PRODUCTION OF LAMBDA_C BARYONS IN PROTON-PROTON AND LEAD-LEAD COLLISIONS AT 5.02 TEV WITH CMS

by
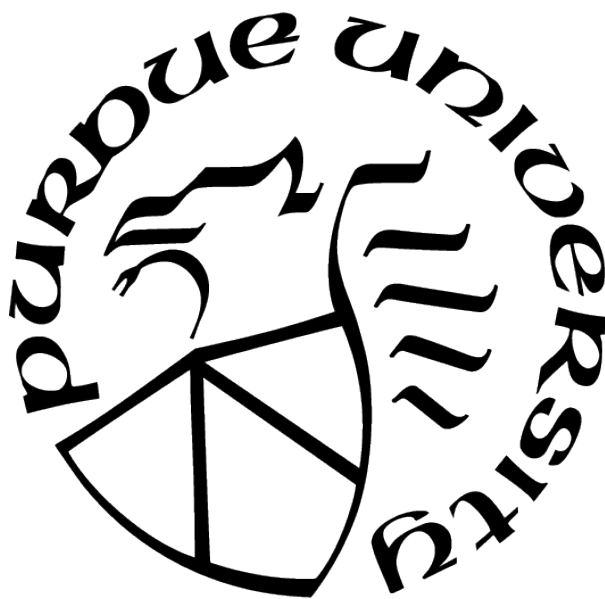
Rui Xiao

A Dissertation

Submitted to the Faculty of Purdue University

In Partial Fulfillment of the Requirements for the degree of

Doctor of Philosophy

Department of Physics and Astronomy

West Lafayette, Indiana

December 2021

THE PURDUE UNIVERSITY GRADUATE SCHOOL
STATEMENT OF COMMITTEE APPROVAL

Dr. Wei Xie, Chair

Department of Physics and Astronomy

Dr. Denes Molnar

Department of Physics and Astronomy

Dr. Fuqiang Wang

Department of Physics and Astronomy

Dr. Martin Kruczenski

Department of Physics and Astronomy

Approved by:

Dr. Gabor Csathy

I am open to everything. When you
start to criticize the times you live in,
your time is over.

_____

Karl Lagerfeld

Even pigs can fly when placed against
the wind.

_____

Jun Lei

ACKNOWLEDGMENTS

The work in this thesis could not be possible without the great assistance and support from my family, my advisor, professors, collegues and friends. I am fortunate to have these amazing people on my journey towards the doctoral degree.

First, I would like to thank my parents and my boyfriend for their support, encourage, love and understanding. My parents, Yuhe Xiao and Ying Gao, have always been supporting my interest, providing me both financial and emotional assistance during my graduate study. My boyfriend, Shengdong Liu, has been extremely patient and unconditionally supportive for the past six and half years.

Second, I would like to express my sincere gratitude to my advisor Prof. Wei Xie for his continuous support and guidance with my research over years. Prof. Xie has taught me what is the most important character to be a physicist, how to shorten the learning curve, how to reduce the systematic uncertainties, and how to overcome the difficulties with persistent effort and inspiring ideas. I would like to thank Prof. Fuqiang Wang for his helpful advice on my research. I would like to thank Prof. Denes Molnar for his explanations and discussion on theory models related to my research and optimizing my algorithm. I would like to thank Prof. Martin Kruczenski for serving as my thesis committee.

Besides my thesis committee, I would like to thank the graduate and postdoctoral group members: Jian Sun, Cheng-Chieh Peng, Hao Qiu, Liang He, Jie Zhao, Terrence Edmonds, Liang Zhang, An Gu, Yicheng Feng, Soumik Chandra, Han-Sheng Li, Milan Stojanovic. They have made the office hours enjoyable and provided daily discussion. I would like to thank Jian Sun, Cheng-Chieh Peng and Hao Qiu for teaching me the CMS software, programming and providing help at the beginning of my studies, as well as Soumik and Milan for contributing to part of the work in this thesis. I also would like to thank all my other friends at Purdue for making my PhD life colorful.

I would like to thank the CMS collaborators from other institutions, who helped to polish the projects presented in this thesis: Jing Wang, Kevin Mattew Stenson, George Stewart Stephans, Emilien Chapon, Yen-Jie Lee and Camelia Mironov. At last, I would like to acknowledge the people, who were involved in the LHC operation, CMS data taking,

4

software development, and software maintenance. Without their effort, there would not be the high quality data, with which my thesis work is performed.

TABLE OF CONTENTS

6

LIST OF TABLES

9

LIST OF FIGURES

12

13

ABSTRACT

Due to the large masses, heavy quarks are produced early and experience the full evolution of the medium. The comparison between the nuclear modification factors of heavy flavor and light hadrons can provide insights into the expected flavor dependence of parton energy loss. The relative coalescence contribution to baryon production is expected to be more significant than that to mesons because of their larger number of constituent quarks. In particular, models involving coalescence of charm and light-flavor quarks predict a large enhancement in the Λ_c^+/D^0 production ratio in the heavy ion collisions relative to pp collisions and also predict that this enhancement has a strong p_T dependence.

This dissertation presents the production of inclusive (prompt) Λ_c^+ baryons in proton-proton and lead-lead collisions at 5.02 TeV in 2015 (2017 and 2018) with CMS detector at the CERN LHC [1]. These two analyses show that Λ_c^+ baryons production is found to be suppressed in heavy ion collisions. This suppression is consistent with the suppression observed in D^0 meson measurements. The Λ_c^+/D^0 production ratios in pp collisions are consistent with a model obtained by adding color reconnection in hadronization to PYTHIA8. Also the Λ_c^+/D^0 production ratios in pp collisions are consistent with the model that includes enhanced contribution from the decay of excited charm baryons and the model includes the effect of fragmentation and coalescence [1]. There is a hint of an enhancement in the Λ_c^+/D^0 production ratio in PbPb collisions in the p_T range of 6–12.5 GeV/c compared to pp collisions. The Λ_c^+/D^0 ratios in pp and PbPb collisions for $p_T > 12.5$ GeV/c are found to be consistent with each other.

1. INTRODUCTION

This chapter presents the theoretical basis and the motivations of the experimental studies in this dissertation.

1.1 Elementary Particle

All elementary particles can be categorized into two groups by their spin: fermions (particles with semi-integer spin) and bosons (particles with integer spin). The wave function of a system of identical bosons is symmetric under the exchange of any pair of them, while the wave function of a system of identical fermions is anti-symmetric.

Figure 1.1 shows the elementary particles in the Standard Model [2]. There are six types of quarks, known as flavor: up, down, charm, strange, top and bottom. Every quark has a corresponding type of antiparticle, called as an antiquark. All six types of quarks and leptons are fermions and can be further categorized into three generations. The gluon and the photon is the force carrier of the strong and electromagnetic interaction, respectively. The W and Z bosons are the force carriers of the weak interaction. The Higgs boson, which was discovered at the Large Hadron Collider (LHC) [3], [4], explains how most elementary particles acquire their mass [5].

1.2 Quantum Chromodynamics

Quantum Chromodynamics (QCD) [7], [8] is a gauge field theory that describes the strong interaction between quarks and gluons. It is the SU(3) component of the Standard Model [2]. This strong interaction is a short-range interaction, on the order of 10^{-15}m. In QCD, gluons interact with quarks and other gluons via "color charge". The color charge in strong interaction is like the electric charge in electromagnetic interaction. There are three color charges: red, blue and yellow. QCD has three main properties: color confinement, asymptotic freedom and chiral symmetry breaking.

- Color confinement is the phenomenon that particles are all color neutral, and color charged particles, such as individual quark or gluon cannot be isolated [9].

Standard Model of Elementary Particles
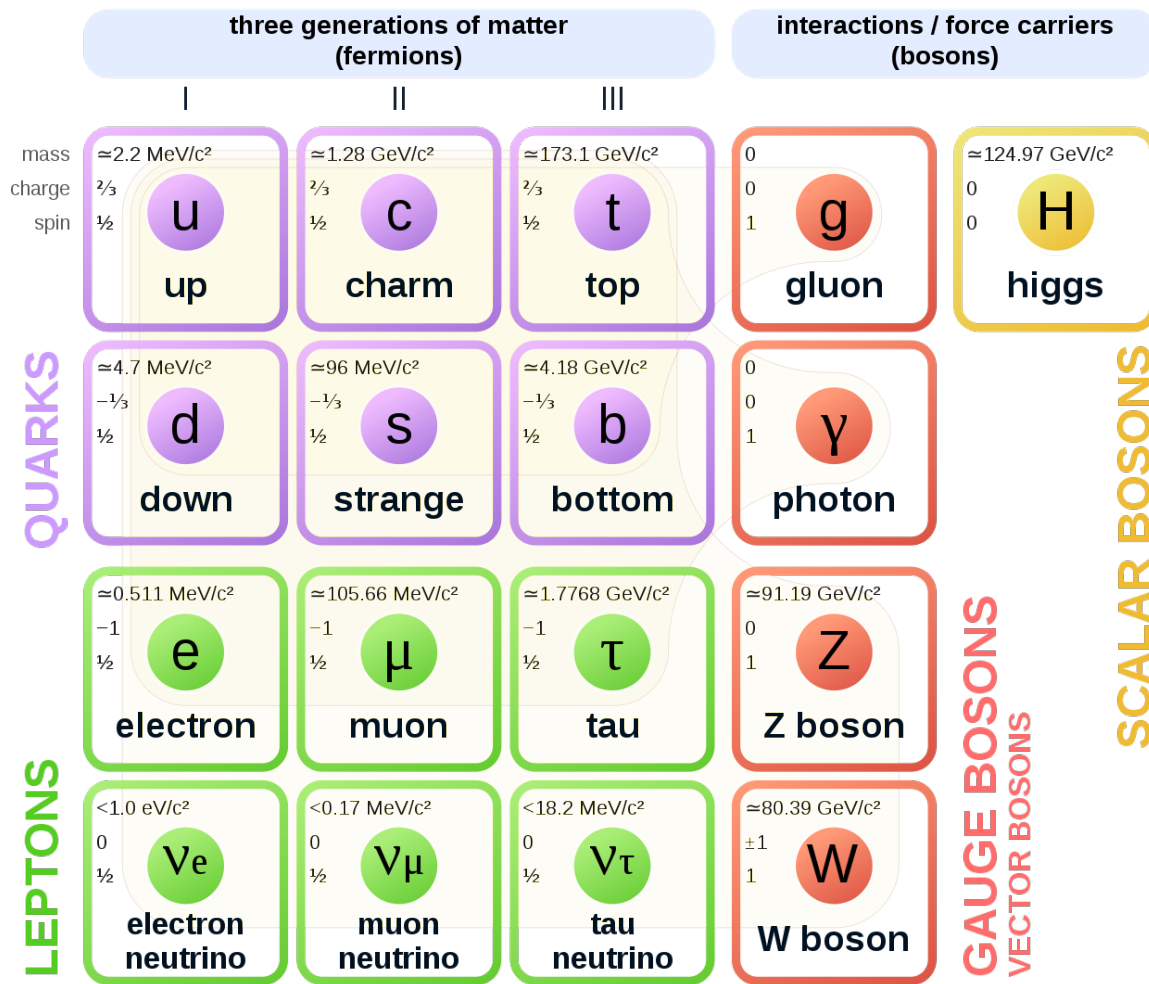
Figure 1.1. Elementary Particles Included In The Standard Model. This Figure Is Taken From Wikipedia [6].

- Asymptotic freedom: When the energy scale of strong interactions increases or the length scale decreases, there is a reduction in the strong interactions between quarks and gluons [8], [10], [11].

- Chiral symmetry breaking. (chirality, discrimination between left and right-handed.)

1.2.1 Lattice Quantum Chromodynamics

Many physical processes involve hadrons. Since hadros are composed of quarks and gluons, the properties of hadrons are governed by QCD. Theoretical calculations of these properties require non-perturbative method, and Lattice QCD is a tool to carry out these calculations. In other words, Lattice QCD reformulates QCD on a lattice of discrete space-time points. Of course, any quantity calculated on the lattice would depend on the lattice spacing. Performing the same calculation multiple times with different, decreasing lattice spacing until the scaling regime is reached, could remove the lattice spacing dependence. The details of how the QCD Lagrangian is put on the lattice could be found in Ref. [2].

1.3 Quark Gluon Plasma

For a few millionths of a second, shortly after the Big Bang, the universe was filled with an astonishingly hot, dense soup made of all kinds of particles moving at near light speed. This mixture was dominated by quarks and gluons. Under this extreme temperature, quarks and gluons were bound only weakly, free to move on their own, and this is called a quark gluon plasma (QGP) [12], [13], [14].

Lattice QCD predicts that there is a change in the state of matter (a phase transition) from a hadronic system to a nearly free gas of quarks and gluon (QGP). Figure 1.2 shows the temperature vs baryon chemical potential [15]. The line of first-order transition ends somewhere near the high temperature axis, indicated on the diagram by the label 'critical point'.

There are three major states for the QCD system shown in Fig. 1.2 [15]: hadron gas, the QGP state, and the color superconductor. The quark matter phase can be reached either by
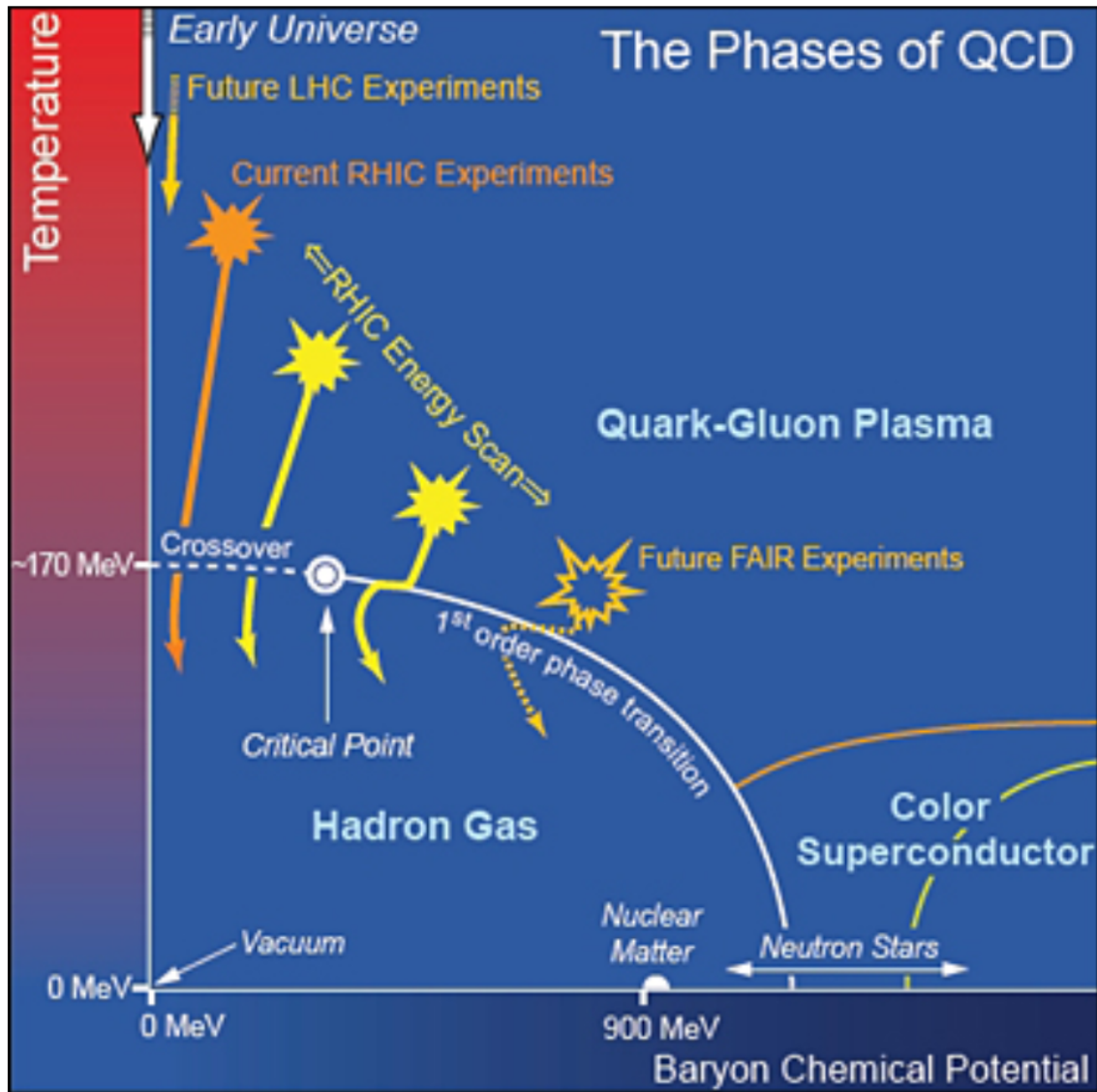
Figure 1.2. A Sketch Illustrating The Experimental And Theoretical Exploration Of The QCD Phase Diagram [15].

compressing nuclear matter to high density while at rather low temperatures or increase the vacuum. The high density phase are expected to play a key role in the interior of neutron stars. With the temperature and/or density increasing, the deconfinement of quarks and gluons occurs as a consequence of the asymptonic freedom and results in the formation of QGP.

Phase transitions usually involve a change in the symmetry of the system. In the early universe, the quarks were massless and there were an equal number of quarks and antiquarks. In the universe today, after the transition to normal nuclear matter, there is a small difference in the light quark masses - as well as an even larger difference between the light quark masses and those of the other quarks, even between the light quark and the strange quark. This mass difference is caused by chiral symmetry breaking. At high temperature chiral symmetry is expected to be restored.

1.3.1 Parton Energy Loss

The QGP state produced in ultra-relativistic heavy ion collisions can last just for a very short time of a few fm/c, so it cannot be directly observed. Parton energy loss is one important signature of the QGP.

In heavy-ion collisions, when the QGP is produced, the out-going partons can lose a large amount of their energy as they traverse the medium, primarily through gluon radiation [16]–[18] and collisional energy loss [19], [20]. Thus, the spectra of produced hadrons will shift toward lower p_T region compared to pp collisions and thus show suppression at high p_T.

The nuclear modification factor (R_{AA}) is one variable to quantify the parton energy loss. (the ratio of the yield in heavy ion collisions to that in pp collisions scaled by the number of nucleon-nucleon interactions). R_{AA} is defined as the followings:

$$R_{\mathrm{AA}}(p_T) = \frac{1}{\langle T_{\mathrm{AA}} \rangle} \frac{dN_{\mathrm{PbPb}}}{dp_T} \bigg/ \frac{d\sigma_{\mathrm{pp}}}{dp_T} \ . \tag{1.1}$$

$R_{AA} = 1$ means that the heavy-ion collisions is the same as pp collisions. When $R_{AA} > 1$, the production is enhanced. When $R_{AA} < 1$, the production is suppressed, which is the general expectation for hadrons with high p_T as a consequence of the in-medium parton energy

loss.

1.4 Heavy Ion Collisions

In order to recreate conditions similar to those of the very early universe, accelerators make head-on collisions between massive ions, such as gold or lead nuclei. The Relativistic Heavy-Ion Collider (RHIC) at BNL [21]–[24] and the Large Hadron Collider (LHC) at CERN [25], [26] produce AuAu and PbPb collisions at energies up to 200 GeV/nucleon and 5500 GeV/nucleon, respectively in the center of mass. In these heavy ion collisions the hundreds of proton and neutrons in two such nuclei smash into one another. This forms a miniscule fireball in which everything "melts" into a QGP. The primary goal of heavy ion collisions is to study the properties of QGP.

In this chapter, the centrality of heavy ion collisions is described.

1.4.1 Centrality Reconstruction And Calibration

The size of the proton may be considered negligible in proton-proton collisions. However, the size of the nuclei cannot be ignored in heavy-ion collisions. In principle, the centrality gives the degree of the overlap of two colliding nuclei. (i.e., the centrality class of 0-30% corresponds to the 30% of collisions with the largest overlap of the two nuclei.). However, the collision geometry cannot be measured directly and only the final-state variables such as momentum and energy can be measured. In the CMS experiment, the events are divided into centrality classes according to the sum of transverse energy (E_T) measured in the Hadron Forward Calorimeters (which will be described in 2.2.). The distribution of the sum of HF E_T for a large sample of minimum bias collisions is measured, and is used to devide the data sample into centrality classes (i.e., the top 10% most energy deposited corresponds to centrality class 0-10%.). The distribution measured in PbPb collisions at 2.76 TeV is shown in Figure 1.3 [27]. The centrality of a collision can also be determined by other final-state observable like rapidity loss, but the basic principle is the same.
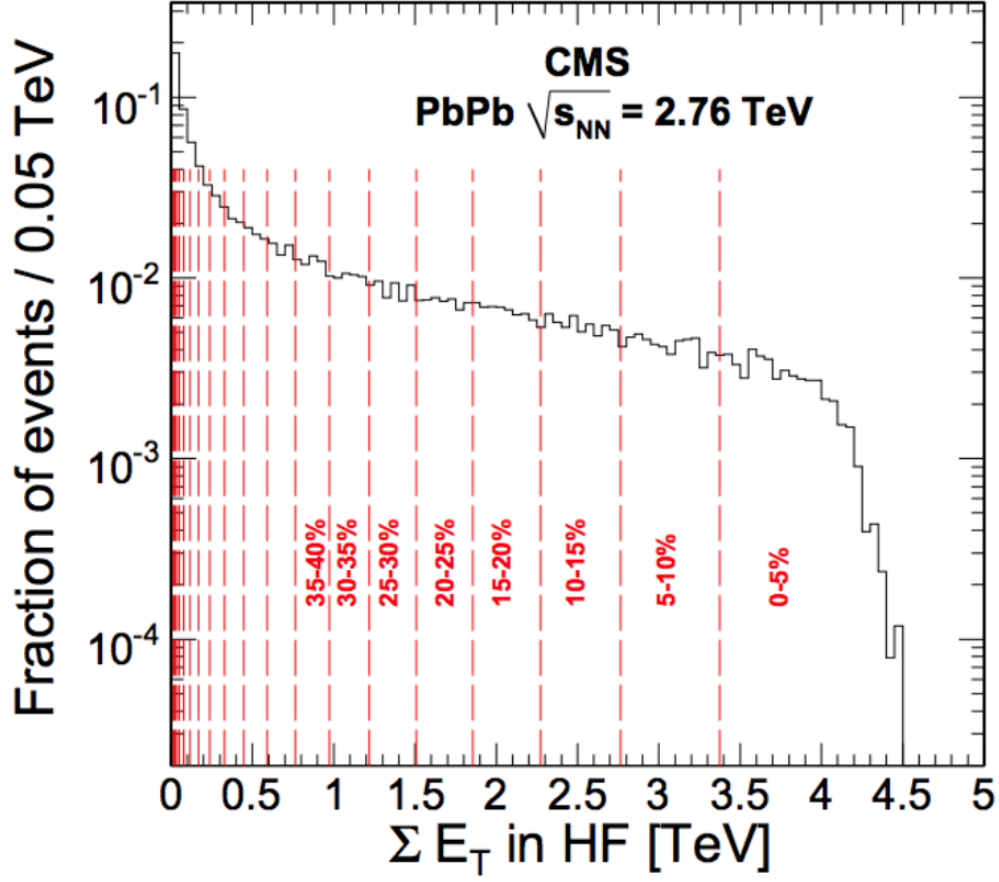
Figure 1.3. Distribution Of The Sum Of HF E_T For A Large Minimum Bias Event Sample Divided Into Centrality Classes Of PbPb Collisions At 2.76 TeV. Figure Is Taken From Ref. [27].

The geometric quantities of heavy ion collisions, such as number of participating nucleons (N_{part}), number of binary nucleon-nucleon collision (N_{coll}), can be calculated by Monte Carlo Glauber model [28], in which each nucleon position in a nucleus is stochastically determined event-by-event. The geometric quantities are estimated by averaging over multiple events in this model. The position of each nucleon in a nucleus is determined according to the Woods-Saxon or Fermi distribution [28]. The nucleons are assumed to move with a straight trajectory along the beam axis. The details of how impact parameter, N_{coll} and N_{part} distributions are calculated from the Monte Carlo Glauber model is written in Ref. [28].

1.5 Open Heavy Flavor Study In Heavy Ion Collisions

Measurements of heavy-quark production provide unique constraints to help us understand parton energy loss and the degree of thermalization in QGP [12] formed in high energy heavy ion collisions. Because of the large masses, heavy quarks are generated via initial hard scattering in heavy ion collisions and experience the whole evolution of the medium. Thus they are effective probes to study the properties of the medium and in-medim interactions [29]. Besides the in-medium interactions, a detailed study of the hadronization process is critical for the interpretation of experimental data. In addition to the fragmentation process, hadron production can also occur via coalescence, in which partons combine with each other while transversing the QGP medium or at the phase boundary [30], [31], in heavy ion collisions. The probability of coalescence has a strong dependence on the p_T distribution. This probability is observed reduced at high transverse momentum ($p_T > 6$ GeV/c), and thus the hadronization process is expected to be dominated by fragmentation.

A significant enhancement of the baryon-to-meson ratio is observed in heavy ion collisions for hadrons with up, down, or strange quarks [32], [33] in p_T range 2-6 GeV/c. This enhancement, and its dependence on centrality can be explained in a scenario with hadronization via coalescence. Furthermore, elliptic flow, the second Fourier component of the azimuthal distribution of emitted particles, is found to roughly scale with the number of constituent quarks in the p_T range of 2–5 GeV/c at RHIC [34], an observation which is also consistent with the expectation for coalescence.

A significant contribution of coalescence to the hadronization of charm quarks from the QGP medium is supported by various measurements of charmonium and open charm production at RHIC and LHC energies [35]–[43]. One such observable is the nuclear modification factor, which is introduced in section 1.3. At RHIC, the R_{AA} for J/ψ mesons with $p_T \leq 7$ GeV/c produced in AuAu collisions decreases significantly from peripheral to central collisions [35]. In contrast, in higher energy PbPb collisions at the LHC, the J/ψ R_{AA} has a much smaller centrality dependence [36], [37]. The difference between the AuAu and PbPb results can be explained by a larger coalescence probability in PbPb collisions because of the larger number of produced charm and anti-charm quarks at the higher center-of-mass energy. The R_{AA} of D^0 meson in AuAu collisions, can be qualitatively reproduced by models involving coalescence [38], [39]. At the LHC, the measurements of D^0 R_{AA} and D^0 azimuthal anisotropy [40]–[43] are well explained by models involving coalescence.

Due to the larger number of constituent quarks in baryons, the relative coalescence contribution to baryon production is expected to be more significant than that to mesons. Models involving coalescence of charm and light-flavor quarks predict a large enhancement in the Λ_c^+/D^0 production ratio in heavy ion collisions relative to pp collisions and also predict that this enhancement has a strong p_T dependence [44]–[47]. Comparison of Λ_c^+ baryon production in pp and lead-lead (PbPb) collisions can thus provide essential insight into understanding heavy-quark transport in the medium and heavy-quark hadronization via coalescence. All discussions of Λ_c^+ and D^0 in this thesis also include their corresponding charge conjugate states.

In this thesis, the analyses on inclusive and prompt Λ_c^+ p_T-differential cross section in both pp and PbPb collisions, nuclear modification factor in PbPb collisions, and Λ_c^+/D^0 in both pp and PbPb collisions with the CMS detector will be presented [1]. The production of prompt Λ_c^+ baryons are found to be suppressed in PbPb collision in centrality class 0–90% and 0–10% [1]. A hint shows that there is an enhancement of the prompt Λ_c^+/D^0 production ratio in 6–12.5 GeV/c in PbPb collisions compared to pp results. The Λ_c^+/D^0 production ratio in PbPb collisions is consistent with the result from pp collisions when $p_T > 12.5$ GeV/c [1]. Apart from these CMS measurements, similar measurements of Λ_c^+ are also performed with ALICE, LHCb detector [48]–[51] in different rapidity ranges and different

center of mass energies. The LHCb p_T-differential cross section results for the rapidity range $2.0 < y < 4.5$ were found to be compatible with the next-to-leading order Generalized Mass Variable Flavor Number Scheme [50], [52], while the ALICE and CMS values were larger than predictions, for $|y| < 0.5$ and $|y| < 1$ [1], [48]. The ALICE Λ_c^+/D^0 production ratio for 6-12 GeV/c in PbPb collisions was noticed to be much larger than pp and pPb collisions, and this difference is possible to be described via a model involving only coalescence in hadronization [49].

1.6 Event Simulation

Event generators are software libraries that generate simulated high energy particles physics events. These event generators are based on some theoretical models or frameworks.

1.6.1 PYTHIA8 Event Generator

The PYTHIA program is a general-purpose generator for the generation of events in high energy collisions, i.e., for description of collisions at high energies between electrons, protons, photons and heavy nuclei. It contains theory and models for a number of physics aspect, including hard and soft interactions, parton distributions, intial- and final-state parton showers, multiparton interactions, fragmentation and decay [53]. PYTHIA8 with different tunes are used in all analyses described in this thesis. The detailed information could be found in this comprehensive manual in Ref. [53]. Hadronization is performed via an implementation of the Lund string fragmentation model. As q and $\bar{q}$ move apart, the potential energy stored in the string increases, and the string may break by production of a new $q'\bar{q}'$, so that the system splits into two colour-singlet systems q$\bar{q}'$ and $q'\bar{q}$. Further breaks may occur unless the invariant mass of either of these string pieces is not large enough. In the Lund string model, the string break-up process is assumed to proceed until only on-mass-shell hadron remain, each hadron corresponding to a small piece of string with a quark in one end and an antiquark in the other [54].

2. THE CMS DETECTOR

The work in this thesis is performed using the data collected by the Compact Muon Solenoid (CMS) detector. The CMS detector is a general-purpose detector at the CERN Large Hadron Collider (LHC), which covers broad physics programs, such as the search for and study of the Higgs boson, the exploration of physics beyond the Standard Model, and also heavy ion physics.

Figure 2.1 shows a schematic representation of the CMS detector with its various subsystems in retracted positions. The CMS detector is build around a 13 m long superconducting solenoid magnet with an inner diameter of 6 m. This takes the form of a cylindrical coil of superconducting cables which can generate a magnetic field of 4 Tesla. The actual magnetic filed strength is 3.8 Tesla during data taking. The innermost part is a silicon-based tacker. Then the next one is a scintillating crystal electromagnetic calorimeter, and then the next one is hadron calorimeter. Outside the magnet are the large muon detectors. This chapter presents certain details of the detector subsystems relevant to the analyses in this thesis. A complete description of the CMS detector can be found in Ref. [55]. The detector coordinate system has the origin centered at the nominal collision point inside the experiment, with the z axis pointing along the counterclockwise beam direction, the x axis pointing radially inward towards the center of the LHC ring, and the y axis pointing vertically upward.

2.1 The Inner Tracking System

The CMS inner tracking system is designed to precisely and efficiently reconstruct the trajectories of charged particles and the secondary vertices. At the LHC designed luminosity, there will be on average about 1000 particles from more than 20 overlapping proton-proton interactions traversing the tracker for each bunch crossing. The CMS tracker consists of a pixel detector and a silicon strip tracker. This thesis uses both the data collected before the pixel detector upgrade and after the pixel detector upgrade. Before the pixel detector upgrade (from the end of 2016), the pixel detector is with three barrel layers at radii between 4.4 cm and 10.2 cm. Figure 2.2 is a schematic view of the previous CMS tracker (used for 2015 data taking, and these data are used for inclusive Λ_c^+ analysis). This pixel detector
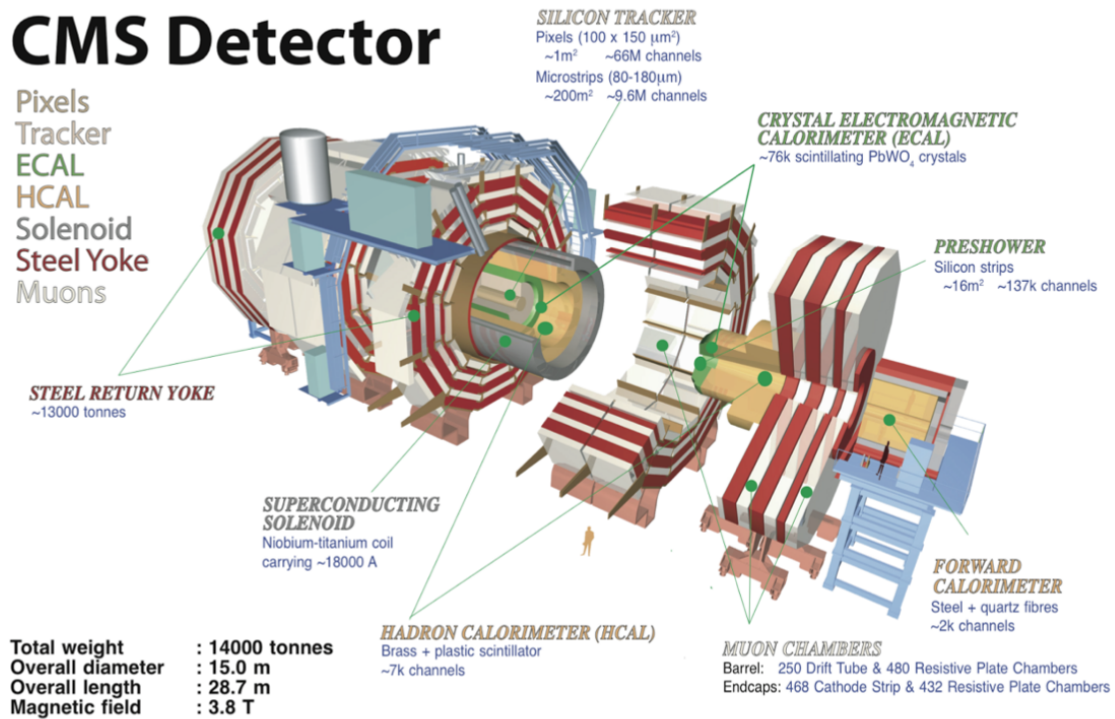
Figure 2.1. A Schematic Representation Of The CMS Detector With Its Various Subsystems In Retracted Positions (CERN)

consists of three barrel layers (BPIX) at radii of 4.4 cm, 7.3 cm and 10.2 cm, and two forward/backward disks (FPIX) at longitudinal positions of ±34.5 cm and ±46.5 cm and extending in radius from about 6 cm to 15 cm. The silicon strip tracker is comprised of 10 barrel layers (TIB and TOB) at midpseudorapidity extending outwards to a radius of 110 cm, and 3 smaller disc layers (TID) and 9 larger disc layers (TEC) at forward pseudorapidity [56].
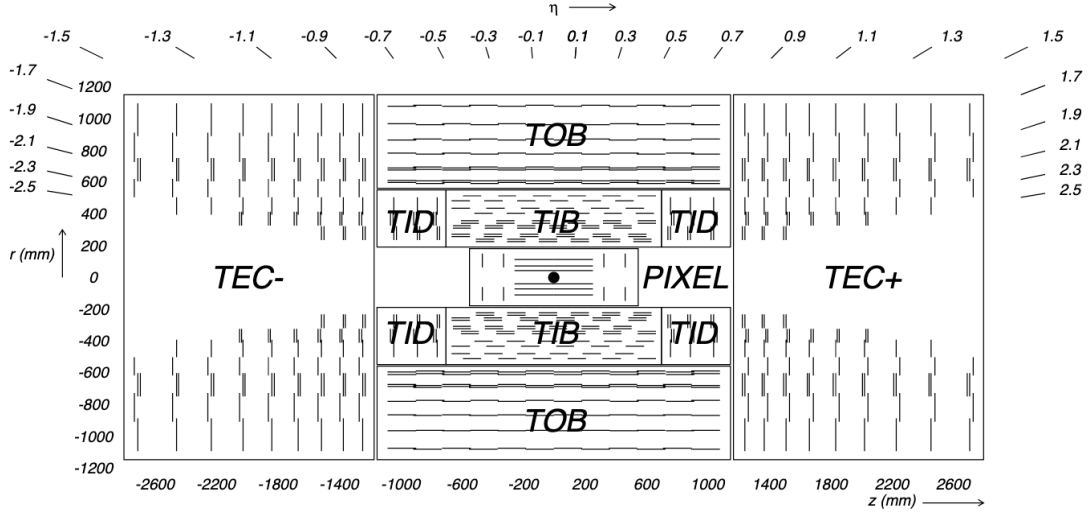
Figure 2.2. Schematic View Of The Previous CMS Tracker (Before The End Of 2016), Showing The Nomenclature Used To Identify Different Sections. Each line Represents A Detector Module. Double Lines Indicate Back-to-back Modules Which Deliver Stereo Hits In The Strip Tracker. This Figure Is Taken From Ref. [57].

After the upgrade, the pixel detector is with four concentric, cylindrical layers with a length of 548.8 mm and radii between 3 cm and 16 cm. The accuracy of the position information can be described by the resolution of track impact parameter. The impact parameter is defined as the minimal distance between the track helix and the primary vertex. Figure 2.3 and 2.4 show respectively the transverse and longitudinal impact parameter resolutions for the upgraded and previous pixel detectors as a function of the track (total) momentum for zero pileup. The ratio of the impact parameter resolutions show that the impact parameter resolution is expected to be greatly improved. This improvement at lower absolute momen-

tum is due to the reduction of material in the upgraded detector [57]. Detailed information of the CMS tracking system can be found in Ref. [56], [57].
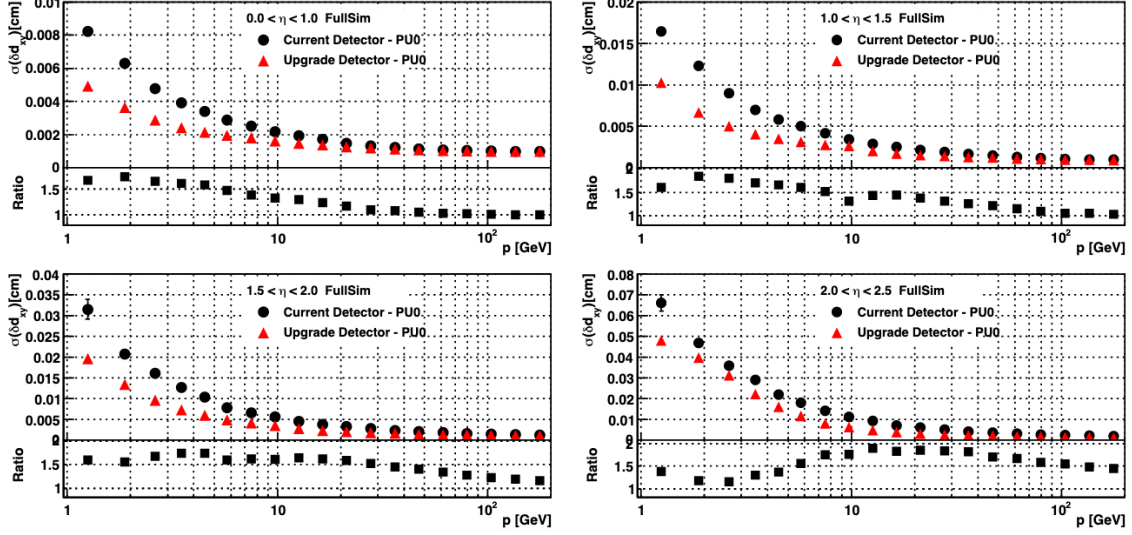
Figure 2.3. Transverse Impact Parameter Resolution For Muon Tracks As A Function Of The Track Momentum For Different η Ranges. The Black Circles Labeled As "Current" Is For The One Before The Upgrade. The Red Triangles Are For The Upgraded Pixel Detector. The Lower Part Of Each Plot Shows The Ratio Of The Previous Detector Resolution To The Upgraded Resolution. (Top-left) $0 < \eta < 1$; (Top-right) $11 < \eta < 1.5$; (Bottom-left) $1.5 < \eta < 2$; (Bottom-right) $2 < \eta < 2.5$. This Figure Is Taken From Ref. [57].

2.2 Hadron Forward Calorimeter

The hadron forward calorimeter (HF) is extremely important to heavy ion collisions, since the centrality can be determined with the HF detector, which has been discussed in section 1.4.1. The forward calorimeter is essentially a cylindrical steel structure with an outer radius of 130.0 cm. Azimuthally, each HF calorimeter consists of 18 modular wedges covering 20°. The two HF calorimeters are located 11.2 m away from the interaction region, one on each end, and together they extend the calorimeter coverage from $|\eta|$=3.0 to 5.2. The steel absorber is composed of 5 mm thick grooved steel and quartz fibers are used as the sensitive material. Each HF calorimeter consists of 432 readout towers, containing long
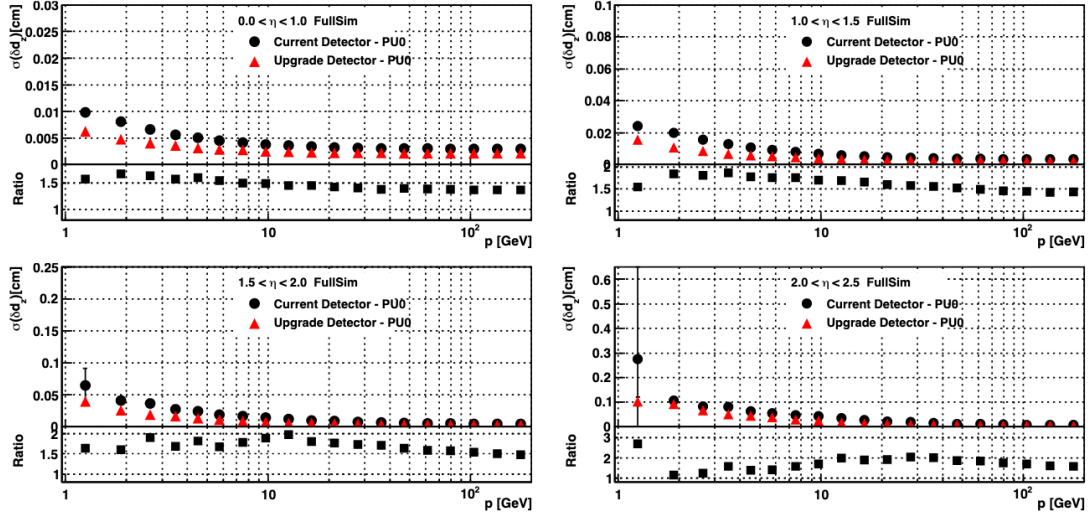
Figure 2.4. Longitudinal Impact Parameter Resolution For Muon Tracks As A Function Of The Track Momentum For Different η Ranges. The Black Circles Labeled As "Current" Is For The One Before The Upgrade. The Red Triangles Are For The Upgraded Pixel Detector. The Lower Part Of Each Plot Shows The Ratio Of The Previous Detector Resolution To The Upgraded Resolution. (Top-left) $0 < \eta < 1$; (Top-right) $11 < \eta < 1.5$; (Bottom-left) $1.5 < \eta < 2$; (Bottom-right) $2 < \eta < 2.5$. This Figure Is Taken From Ref. [57].

and short quartz fibers running parallel to the beam, providing information on the shower energy and relative contribution originating from hadrons versus electrons and photons. The cross sectional view and transverse plan of HF calorimeter are shown in Fig. 2.5. A detailed description can be found in Ref [56].
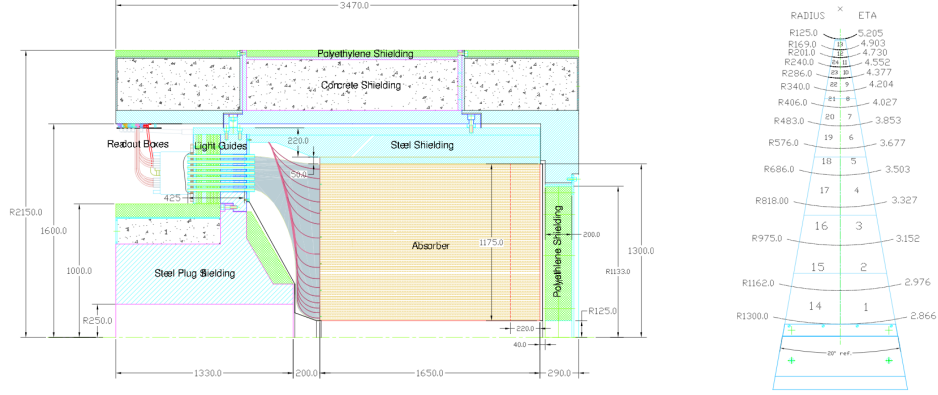
Figure 2.5. (Left) The Cross Sectional View Of The HF Calorimeter. (Right) Transverse Segmentation Of A Single 20° Modular Edge Of The HF Detector. Figures Are Taken From Ref. [56].

2.3 The Level-1 And High Level Trigger System

For the nominal LHC design luminosity of $10^{34}cm^{-2}s^{-1}$, an average of 17 events occurs at the beam crossing frequency of 25 ns. The high input rate must be reduced to accommodate the on-line computer. Therefore, the trigger system is designed to reduce the rate of recording under 1 kHz by keeping the interesting events for analyses and filtering out the uninteresting events. CMS reduces this rate by two steps: (1) The Level-1 (L1) Trigger [58]. (2) High-Level Trigger (HLT) [59]. The L1 triggers are hardware-based system and the HLT triggers are software-based.

The L1 triggers consists of custom-built programmable electronics, which are largely integrated with the readout systems of subdetectors. The L1 triggers are designed to reduce the rate under 100 kHz. Within 4 μs, the system must decide whether to drop an event or pass it to the HLT triggers. The L1 triggers are typically implemented using simple

threshold algorithms written to filed-programmable gate arrays (FPGAs), which allow for a fully customizable hardware circuit.

The HLT triggers select events in a similar way, and pass a fraction of these events to the remainder of the online computer resources. For each event, objects such as tracks, muons, and jets can be reconstructed and applied selection criteria to select the interesting events for analyses.

2.4 The CMS Computing Model

Unlike previous generations of experiments, the majority of data storage and processing resources are available outside the host laboratory. CMS chooses to use a distributed system of computing resources. Figure 2.6 shows the dataflow between CMS computing centers [56]. The details of the CMS computing system can be found in Ref. [60].
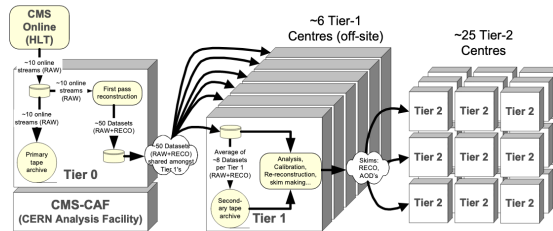
Figure 2.6. Dataflow Between Different CMS Computing Centers. This Figure Is Taken From Ref. [56].

Tier-0 is the first tier of the computing system, which is responsible to accept and store the raw data at CERN, perform a real-time reconstruction of the data, and distribute both raw and reconstructed data to Tier-1.

Tier-1 regional centers archives the RAW and reconstructed data (a second copy of RAW and reconstructed RECO data), performs additional reconstruction over the data with the timely calibration, and distribute reconstruction data to Tier-2. Besides these responsibilities, it also provide secure storage and redistribution for Monte Carlo simulated samples which are produced by the Tier-2 and other centers.

The Tier-2 centres have the following responsibilities:

- keep part of the reconstruction data for physics analyses.

- produce Monte Carlo simulations.

3. Λ_c^+ RECONSTRUCTION AND CUT OPTIMIZATION

In this thesis, the Λ_c^+ baryons are reconstructed through the hadronic decay channel $\Lambda_c^+ \to P^+K^-\pi^+$ with a branching ratio of 6.28±0.32% [2]. Figure 3.1 is the schematic view of the $\Lambda_c^+ \to P^+K^-\pi^+$ decay channel and the variables marked will be defined and discussed below.
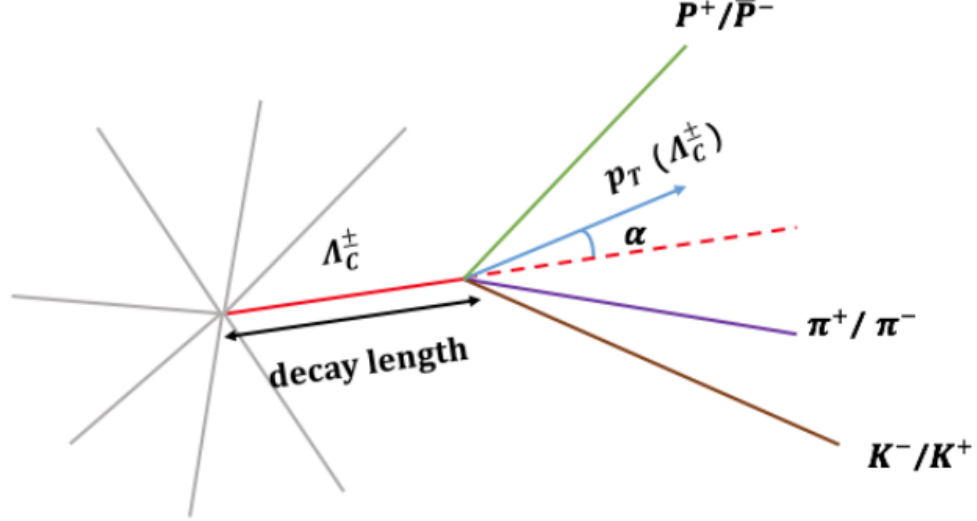
Figure 3.1. Schematic View Of The Λ_c^+ Decay Channel Used In This Thesis.

3.0.1 Λ_c^+ Reconstruction

Λ_c^+ candidates are considered by assuming that three tracks having the mass of proton, kaon and pion and then do the permutations. The decay vertex is reconstructed by using a ROOT "KinematicParticleVertexFitter", where least-mean squared minimization is implemented. Several geometric selections are applied in order to reduce the combinatorial background. In particular, the Λ_c^+ are selected according to the following topological variables:

- the 2D decay length significance with respect to Beam Spot (BS) for pp collisions and 3D decay length significance with respect to Primary Vertex (PV) for PbPb collisions.

- 2D pointing angle α with respect to BS for pp collisions and 3D pointing angle α with respect to PV for PbPb collisions.

- vertex probability.

- track p_T over Λ_c^+ p_T ratio for pp and PbPb collisions.

3.0.2 Cut Optimization

The aim of the cut optimization is to maximize the statistical significance (which is $s/\sqrt{b}$ in this analysis) of the signals with a still reasonable high signal efficiency. The optimal cut minimizing background efficiency for a specific signal efficiency is obtained by the TMVA(Toolit for Multivatiate Data Analysis with ROOT) [61]. Rectangular cut and Boosted Decision Tree is chosen as the classification methods in TMVA. The reconstructed Λ_c^+ candidates that are matched to the generated Λ_c^+ baryons are used as the signal sample and sideband data are used as the background sample. The sideband is defined as the shoulder region right next to the $\sim 3\sigma$ boundaries of fit to the observed signal on both side (i.e., mass = 2.315–2.355 GeV/c^2 and mass = 2.215–2.255 GeV/c^2).

Due to the high luminosity, more than one collision can occur in the same bunch crossing in pp collisions. To make the measurement less sensitive to this pileup effect, two-dimensional variables in the transverse plane with respect to an estimate of the pp interaction region (beamspot) are used in pp collisions.

The cut variables for pp collisions are the followings:

- 2D decay length significance with respect to BS. ("2D dls")

- vertex probability.("chi2cl")

- 2D pointing angle with respect to BS.("2D α")

- daughter tracks p_T ratio distribution.

And the cut variables for PbPb collisions are the followings:

- 3D decay length significance with respect to PV. ("3D dls")

- vertex probability.("chi2cl")

- 3D pointing angle with respect to PV.("3D α")

- daughter tracks p_T ratio distribution.

To minimize the size of the analysis tree output, the following initial cuts are applied for the Λ_c^+ production with 2015 CMS pp and PbPb data for inclusive Λ_c^+ analysis.

- 3D dls with respect to PV > 1.0 and > 2.0 for pp and PbPb collision.

- chi2cl > 0.05 for both pp and PbPb.

- 3D α < 0.2 in PbPb collisions and 3D α does not have this initial cuts in pp collisions.

- track p_T > 1 GeV/c and > 0.7 GeV/c for PbPb and pp.

The initial cuts applied for the Λ_c^+ production with 2017/2018 CMS pp and PbPb data for prompt Λ_c^+ analysis are:

- 3D dls with respect to PV > 2.0 for PbPb collision only when p_T < 30 GeV/c.

- chi2cl > 0.05 for both pp and PbPb. (No cuts for PbPb collisions with p_T > 30 GeV/c.)

- 3D α < 0.2 in PbPb collisions.

- track p_T > 1 GeV/c and > 0.5 GeV/c for PbPb and pp collisions, respsectively.

The rapidity of the Λ_c^+ candidates are required to be within ± 1, leading to the daughter track pseudorapidity dominantly reside in ± 1.2. Thus, $|\eta_{track}| < 1.2$ is required in the initial cuts for both analyses. The sample with these initial cuts are used as inputs to the TMVA training.

The optimal cut values are defined as the one that can maximize the significance $s/\sqrt{b}$. The statistical significance is defined as this form so that the input signal and background do not need to be normalized to the same number of luminosity. Since the signal background ratio for Λ_c^+ is small, if the default statistical significance definition in TMVA package ($s/\sqrt{s+b}$) is used, the optimized cuts are sensitive to the normalized weight.

$s = s\times$ (signal cut efficiency), where s is the number of Λ_c^+ candidate in data before optimal cuts, and the signal efficiency is Λ_c^+ after optimal cuts over the Λ_c^+ candidates before optimal cut.

$b = b\times$ (background cut efficiency), where b is the amount of background before cuts, and the background efficiency is background after optimal cuts over the background before optimal cut. Signal region is defined as $|m_{\Lambda_c^+} - m_{\Lambda_c^+(\text{PDG})}| < 3\sigma$. σ is the with of Λ_c^+ candidates mass fitting in MC.

4. PRODUCTION OF INCLUSIVE Λ_c^+ IN PP AND PBPB COLLISIONS AT 5.02 TeV WITH 2015 CMS DATA

This chapter presents the details of the measurements of inclusive Λ_c^+ with 2015 CMS data.

4.1 Data Sets And Monte Carlo Simulation

This analysis is performed using the 2015 pp and PbPb data at $\sqrt{s_{\mathrm{NN}}} = 5.02$ TeV. The luminosity of MB pp, MB PbPb golden json and tracker only json sample are 38 nb^{-1}, $\sim$ 21.639 μb^{-1} and $\sim$ 22.223 μb^{-1}, respectively. Thus, the luminosity for MB PbPb data is $\sim$ 44 μb^{-1}. More data are available from PbPb 30-100% centrality trigger sample which has a luminosity of $\sim$ 57.711 μb^{-1}. Details of the data sets for inclusive Λ_c^+ analysis are summarized in Tab. 4.1. The good quality of the data is ensured by applying the JSON file

Table 4.1. CMS 2015 Datasets Used For Inclusive Λ_c^+ Production Analysis.

sample	DAS name	Global Tag
pp	/MinimumBias1-20/Run2015E-PromptReco-v1/AOD	auto:run2_data
PbPb	/HIMinimumBias1-11/HIRun2015-PromptReco-v1/AOD	75X_dataRun2_v13

for pp and PbPb respectively. (The file describes which luminosity sections in which runs are considered good and should be processed. In CMS, these files are in the JSON format.)

- Cert_262081-262328_5TeV_PromptReco_Collisions15_25ns_JSON.txt

- Cert_262548-263757_PromptReco_HICollisions15_JSON_v2_PbPb.txt

- Cert_263685-263757_PromptReco_HICollisions15_TrackerOnly_JSON.txt

Both pp and PbPb samples were reconstructed using the CMSSW version CMSSW_7_5_8.

4.1.1 Signal Monte Carlo

Monte Carlo simulations of inclusive Λ_c^+ productions were made in order to estimate the acceptance $\times$ reconstruction efficiency ($\alpha\epsilon$) and also to help to evaluate systematic uncertainties. For pp collisions, QCD events are generated by PYTHIA8 [53] with Tune

CUEP8M1 [62] at 5.02 TeV. We use the $\Lambda_c^+ \to P^+K^-\pi^+$ channel, which includes four sub-channels:

- $\Lambda_c^+ \to P\bar{K}^*(892)^0 \to P^+K^-\pi^+$ (1.29%)

- $\Lambda_c^+ \to \Delta(1232)^{++}K^- \to P^+K^-\pi^+$ (1.07%)

- $\Lambda_c^+ \to \Lambda(1520)\pi^+ \to P^+K^-\pi^+$ (0.494%)

- $\Lambda_c^+ \to P^+K^-\pi^+$ (nonresonant) (3.4%)

While in Particle Physics Booklet, the decay channel shows like this: The whole branching fraction for $\Lambda_c^+ \to P^+K^-\pi^+$ is 6.28 ±0.32%. The four sub-channels are:

- $\Lambda_c^+ \to P\bar{K}^*(892)^0$ $(1.94 \pm 0.27\%)$

- $\Lambda_c^+ \to \Delta(1232)^{++}K^-$ $(1.07 \pm 0.25\%)$

- $\Lambda_c^+ \to \Lambda(1520)\pi^+$ $(2.2 \pm 0.5\%)$

- $\Lambda_c^+ \to P^+K^-\pi^+$ (nonresonant) $(3.4 \pm 0.4\%)$

The sum of the branching fractions of the above sub-channels is not equal to that of the whole channel that we use in this analysis. The reason for this is that for the first three sub-channels, there are two decays. We will calculate the branching fraction of $\Lambda_c^+ \to P\bar{K}^*(892)^0 \to P^+K^-\pi^+$ as an example: $\Lambda_c^+ \to P\bar{K}^*(892)^0 \to P^+K^-\pi^+$ is from:

- $\Lambda_c^+ \to P\bar{K}^*(892)^0$ (1.94%)

- $\bar{K}^*(892)^0 \to K\pi$ ($\sim 100\%$)

The second bullet actually is composed of: $\bar{K}^*(892)^0 \to K^-\pi^+$ and $\bar{K}^*(892)^0 \to \bar{K}^0\pi^0$. While the second step is a decay into kaon and pion which are not only $K^\pm$ and $\pi^\mp$. We use Isospin conservation to calculate the branching fraction with the C-G coefficient. We use this pair (I,M) to represent (Isospin, the z-component of Isospin). So we have the followings:

π^0:(1,1), π^0:(1,0), K^-:($\frac{1}{2}$,$\frac{-1}{2}$), $\bar{K}^0$:($\frac{1}{2}$,$\frac{1}{2}$) and $\bar{K}^*(892)^0$:($\frac{1}{2}$,$\frac{1}{2}$). From C-G coefficient, we get $\frac{2}{3}$ for $\bar{K}^*(892)^0 \to K^-\pi^+$ and $\frac{1}{3}$ for the other channel. Then the final branching fraction for $\Lambda_C^+ \to P\bar{K}^*(892)^0 \to P^+K^-\pi^+$ is $1.94\% \times \frac{2}{3} = 1.29\%$

The final branching fractions for all the sub-channels are written as the followings:

- $\Lambda_c^+ \to P\bar{K}^*(892)^0 \to P^+K^-\pi^+$ ($1.94\% \times \frac{2}{3} = 1.29\%$)

- $\Lambda_c^+ \to \Delta(1232)^{++}K^- \to P^+K^-\pi^+$ (1.07%)

- $\Lambda_c^+ \to \Lambda(1520)\pi^+ \to P^+K^-\pi^+$ ($2.2\% \times 22.5\% = 0.494\%$)

- $\Lambda_c^+ \to P^+K^-\pi^+$ (nonresonant) (3.4%)

The reason that we calculate this branching fraction is that we need to mix the simulation samples for four sub-channels according to the individual branching fraction to do this analysis, also we need this relative branching fraction to calculate $\alpha\epsilon$ which will be described in details later. Λ_c^+ were forced to decay to these four sub-channels respectively, which means that for these four sub-channels, we should have 4 simulation samples, in each of which, Λ_c^+ were forced to decay to the specific sub-channel. Only events with at least one Λ_c^+ with $|y| < 1.2$ and $|\eta| < 2.4$ were kept. The number of generated output simulation events for Λ_c^+ different sub-channels and different p_T thresholds are shown in Tab. 4.2. A $\hat{P}_T$ threshold is also used to speed up PYTHIA production of high Λ_c^+ p_T events, as also listed in the table. It has been studied that these $\hat{P}_T$ thresholds are low enough for according Λ_c^+ p_T, and will not bias the distribution.

Table 4.2 shows the requested simulation samples for each individual sub-channel. Two $\hat{P}_T$ bins are used in order to obtain enough sample in different p_T bins. The $\hat{P}_T > 0$ GeV/c condition is used for p_T = 5-10 GeV/c sample. The $\hat{P}_T > 4$ GeV/c condition is used to produce $p_T > 10$ GeV/c sample. The $\hat{P}_T$ cut is selected to ensure 100% efficiency for the signals in the corresponding p_T bins.

For PbPb productions, selected PYTHIA8 events were embedded into a simulated PbPb background generated by HYDJET (VERSION 1.8, tune "Cymbal5Ev8") [63].

Table 4.2. Λ_c^+ p_T Threshold, Number Of Output Events And $\hat{P}_T$ Threshold For Simulation Samples For Inclusive Λ_c^+ Analysis In Both pp And PbPb Collisions.

sub-channel	Λ_c^+ p_T threshold (GeV/c)	# output simulation events	$\hat{P}_T$ (GeV/c)
$\Lambda_c^+ \rightarrow P\bar{K}^*(892)^0 \rightarrow P^+K^-\pi^+$	4	50k	0
$\Lambda_c^+ \rightarrow P\bar{K}^*(892)^0 \rightarrow P^+K^-\pi^+$	10	50k	4
$\Lambda_c^+ \rightarrow \Delta(1232)^{++}K^- \rightarrow P^+K^-\pi^+$	4	50k	0
$\Lambda_c^+ \rightarrow \Delta(1232)^{++}K^- \rightarrow P^+K^-\pi^+$	10	50k	4
$\Lambda_c^+ \rightarrow \Lambda(1520)\pi^+ \rightarrow P^+K^-\pi^+$	4	20k	0
$\Lambda_c^+ \rightarrow \Lambda(1520)\pi^+ \rightarrow P^+K^-\pi^+$	10	20k	4
$\Lambda_c^+ \rightarrow P^+K^-\pi^+$ (nonresonant)	4	100k	0
$\Lambda_c^+ \rightarrow\rightarrow P^+K^-\pi^+$ (nonresonant)	10	100k	4

Table 4.3. Summary Of HLT Paths Used In The 2015 pp And PbPb Analysis

DataSet	HLT trigger
pp	HLTL1MinimumBiasHF1OR__part* __v1
PbPb	HLTL1MinimBiasHF2AND__part*__v1
PbPb	HLT__HIL1Centralityext30100MinimumumBiasHF2AND__part1__v1, part1, part2, part3

Table 4.4. Track Selection Criteria Applied In The 2015 pp And PbPb HLT Tracking.

	pp p_T	PbPb p_T
Track quality	highpurity	highpurity
$|\eta|$	<1.2	<1.2
p_T	>0.7	>1
Track algo	4-5-6-7	4-5-6-7
trkChi2/trkNdof/trkNlayers	<0.15	<0.15
trkNHits	>=11	>=11
trkPtError/trkPt	<0.1	<0.3

4.1.2 Event Selection

This analysis uses samples collected from minimum-bias triggers. Event selections are used to reject noise and beam-background event.

For pp, the HLT trigger is HLTL1MinimumBiasHF1OR_part*_v1. To further enhance the statistics for PbPb collisions with centrality 30-100%, the centrality triggers are also used in this inclusive Λ_c^+ analysis. The names of the specific centrality triggers are: HLT__HIL1Centralityext30100MinimumumBiasHF2AND__part*__v1.

The HLT track reconstruction in PbPb collisions corresponds to the standard Heavy ion tracking sequence used in the HI analysis. The HLT track reconstruction in pp includes the first 5 offline tracking iterations. A summary of the track selections applied in the HLT tracking is presented in Table 4.4.

In the offline analysis for PbPb collisions, an additional selection of hadronic collisions is applied by requiring a coincidence of at least three of the HF calorimeter towers, with more than 3 GeV of total energy, from the HF detectors on both sides of the interaction point. Events are required to have at least one reconstructed primary vertex [56]. The primary

vertex is formed by two or more associated tracks and is required to have a distance from the nominal interaction region of less than 15 cm along the beam axis and less than 0.15 cm in the transverse plane. Table 4.3 shows the HLT MB triggers for both pp and PbPb collisions for 2015 CMS data sets used in this inclusive Λ_c^+ analysis.

4.2 Signal Extraction

In this section, inclusive Λ_c^+ candidates and signal yield extraction for pp and PbPb collision are described. Raw yields are extracted in each p_T interval via unbinned maximum likelihood fit to the invariant mass distribution. The fit function consists of the following components:

- a double Gaussian function with same mean but different width and strength to model the signal shape determined from MC in the each p_T bin.

- a 3rd-order Chebyshev polynomial function to model the combinatorial background and the swapped Λ_c^+ component for both pp and PbPb collisions.

We use the same strategy as Ref. [41]: the signal shape is defined by the simulation, and a floating width parameter is used to accommodate the difference in the signal shape between simulation and data in all p_T bins except for pp 5–6 GeV/c. The swapped components are the Λ_c^+ signals with incorrect mass assignment from the exchange of the proton and pion mass for lack of particle identification. Although three particles are combined for a Λ_c^+ signal, the charge of kaon differs from that of both the proton and the pion, which means that only proton and pion have the possibility for incorrect mass assignment.

In the above signal extraction procedure, we fix the two widths of the double Gaussian and the ratio of the yield between the two Gaussians. We let the mean and also one parameter that corresponds to two widths of the double Gaussian float in this fit in all bins except for pp 5–6 GeV/c. For pp 5–6 GeV/c, because there is always a bias in the fit, we scan the value of float width in the range [-0.4,0.4] and perform a toy MC study to find the value of the width with the smallest bias. All parameters, including mean, two sigma of

double Gaussian MC fit are shown in Figure 4.2 and Figure 4.3 (in several p_T ranges for pp collisions). Figure 4.5–Figure 4.7 show the signal extraction with the default fit function in both pp and PbPb collisions with three centrality ranges. The red line represents the signal on top of the background, while the blue dashed line is the fit function for the background.

The distribution of swapped component is broad (about 30 times broader) as shown in Figure 4.1 and cannot be distinguished from the combinatorial background. We thus use the Chebyshev polynomial function to represent the combination of the swapped component and the combinatorial background. Figure 4.1 shows the mass distribution of the gen-matched signal as well as the swapped component.

4.3 Acceptance And Efficiency Correction

Acceptance and efficiency corrections are applied to the extracted inclusive Λ_c^+ yields in order to get the corrected spectra. In this section, we present the acceptance×efficiency product as a function of p_T of inclusive Λ_c^+. The studies are performed using PYTHIA8 samples for pp and PYTHIA+HYDJET samples for PbPb collisions.

The correction factor that is relevant for the cross section is the acceptance efficiency. However, to present the effect of acceptance by itself, we also provide the acceptance as a function of p_T. The acceptance (α) is defined as the fraction of Λ_c^+ generated in $|y| < 1$ that have three tracks that fullfill the initial single track acceptance selections (i.e., $p_T > 0.7$ GeV/c (pp) or 1.0 GeV/c (PbPb) and $|\eta| < 1.2$). Figure 4.8 shows α as a function of Λ_c^+ p_T in pp (upper left) and PbPb collisions in 0–100% (upper right), 0–30% (lower left) and 30–100% (lower right) centrality bins. For all centrality ranges in PbPb collisions, the acceptances are identical as expected. The acceptance in pp is higher than the one in PbPb for $p_T = 10$–20 GeV/c due to looser track p_T cuts. It is confirmed by assigning the same track p_T cut where the pp and PbPb acceptance are essentially the same.

The reconstruction efficiency ϵ_{reco} is defined as the fraction of reconstructed Λ_c^+ candidates with reconstructed and selected tracks that fullfill the Λ_c^+ selection criteria which are the
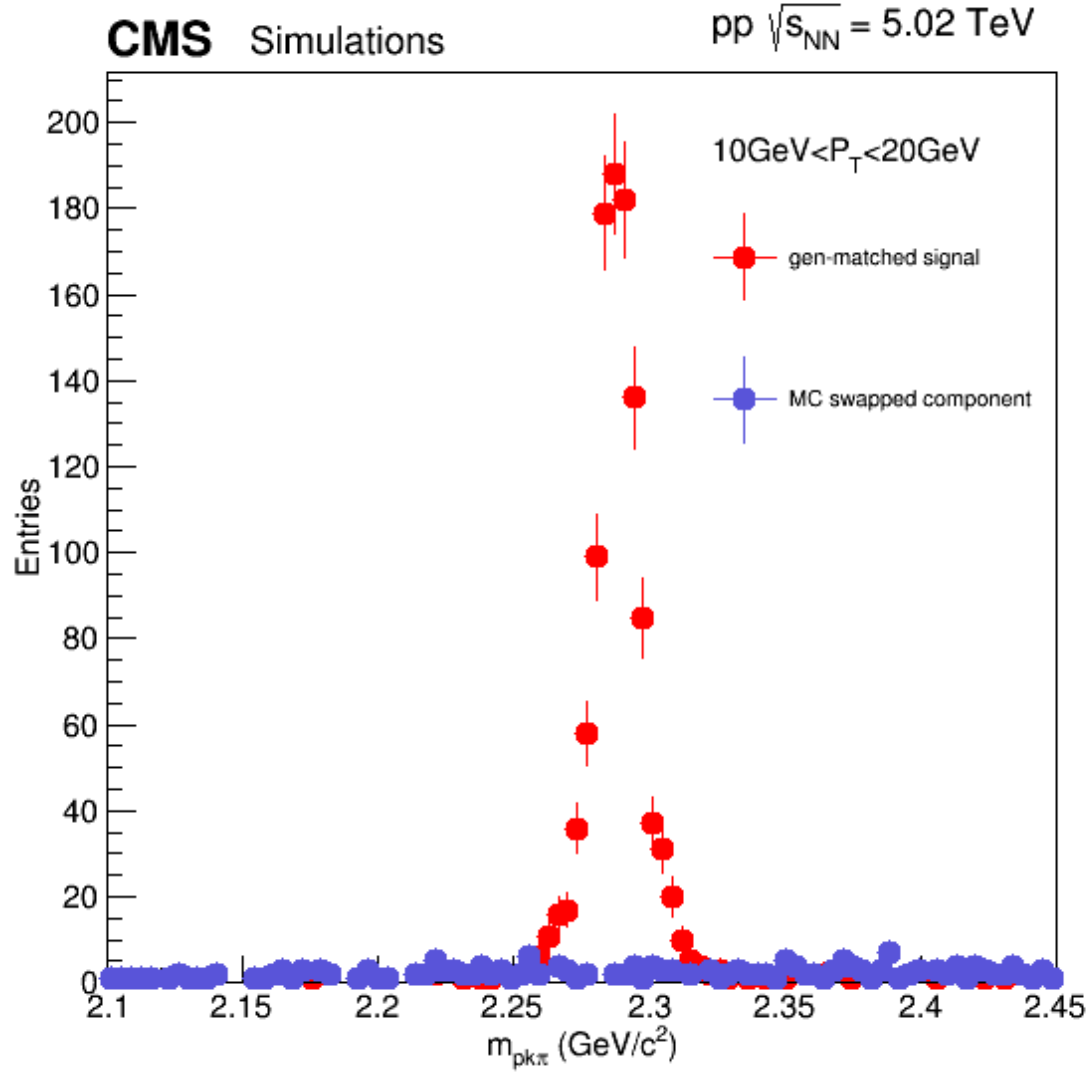
Figure 4.1. The Mass Distribution Of Gen-match Signal And The Swapped Component For pp In $p_T = 10$–20 GeV/c. The Red Points Are The Gen-matched Signal And The Blue Points Are Swapped Component.
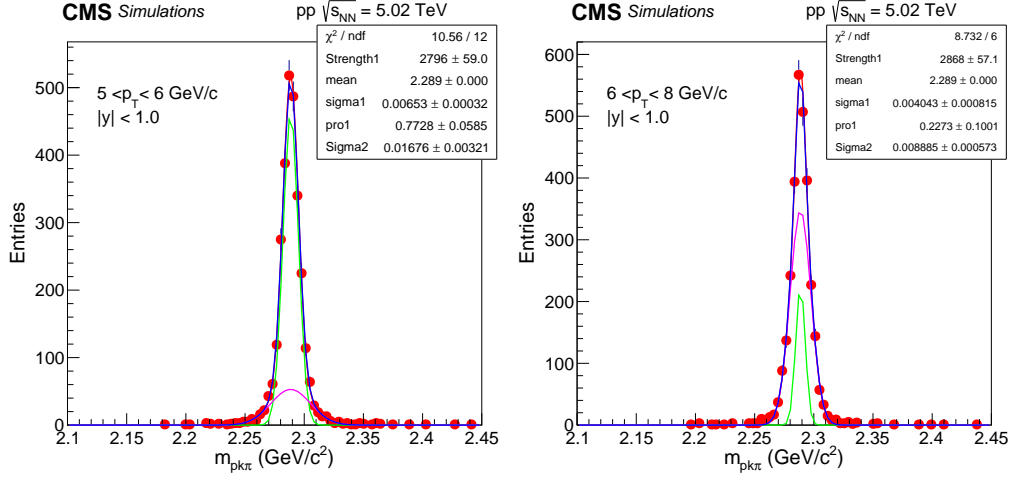
Figure 4.2. Double Gaussian Fit For pp Collisions In $p_T = 5$–6 GeV/c (Left) And 6–8 GeV/c (Right). In Both Plots, The Blue Line Is The Whole Double Gaussian Fit Function And The Green And Pink Lines Are The Gaussian Fit Function With The Same Mean But Different Widths.
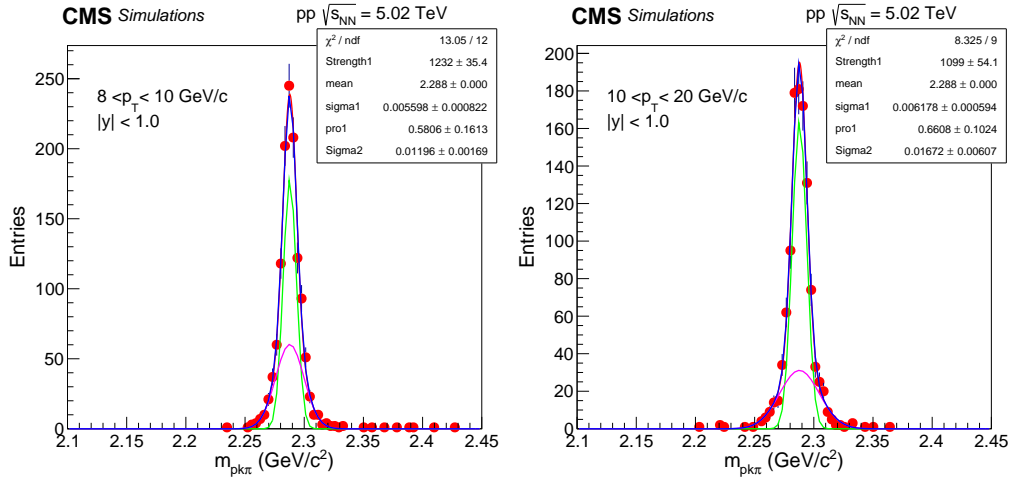
Figure 4.3. Double Gaussian Fit For pp Collisions In $p_T = 8$–10 GeV/c (Left) And 10–20 GeV/c (Right). In Both Plots, The Blue Line Is The Whole Double Gaussian Fit Function And The Pink Lines Are The Gaussian Fit Function With The Same Mean But Different Widths.
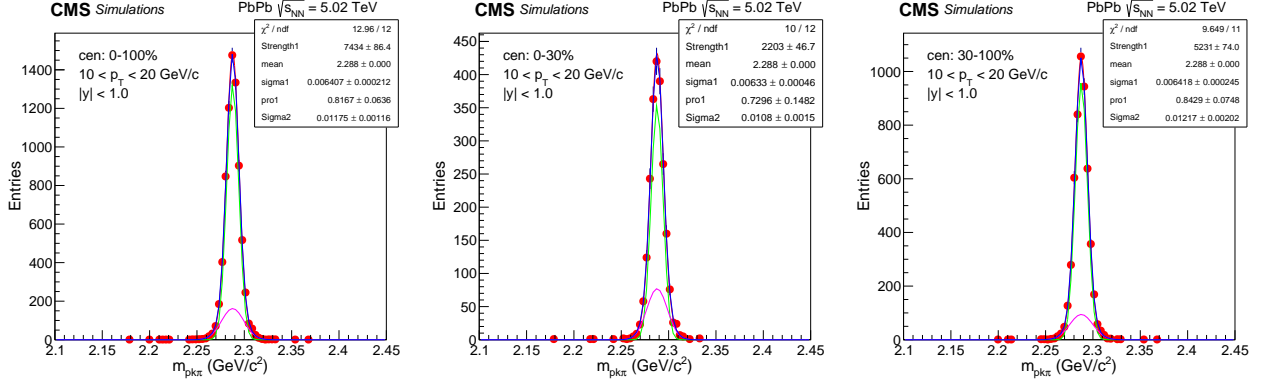
Figure 4.4. Double Gaussian Fit For PbPb Collisions In Centrality Range 0–100% (Left), 0–30% (Middle) And 30–100% (Right).
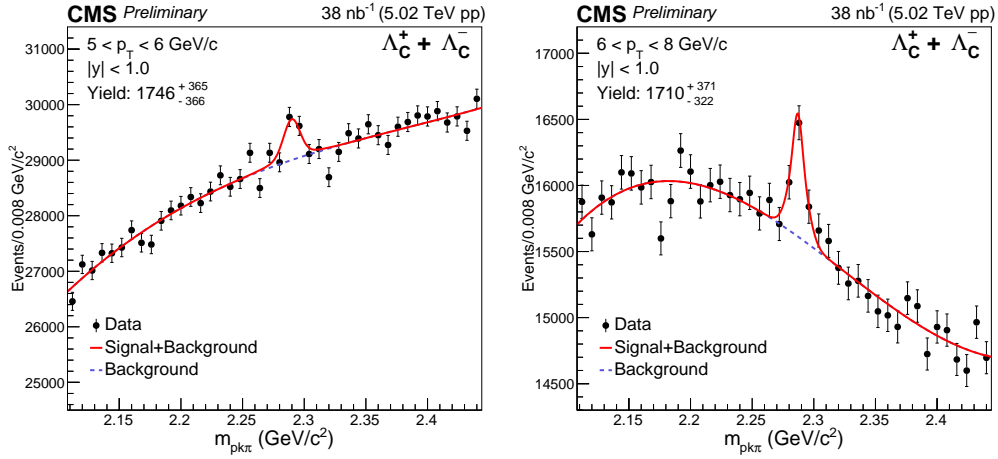
Figure 4.5. Λ_c^+ Signal Extraction In pp Collisions For p_T Ranges: 5–6 GeV/c (Left) And 6–8 GeV/c (Right). The Red Line Is The Function For The Foreground And The Blue Dashed Line Is The Function For The Background.

optimized cuts from TMVA training of each p_T bins. There are four sub-channels for this channel, so when we calculate the acceptance×efficiency product, we weight $A\epsilon_{reco}$ of each sub-channel as:

$$\alpha\epsilon_{reco} = \frac{\sum_{n=1}^{4} \alpha_i\epsilon_{reco}(i) \times \mathcal{B}_i}{\sum_{n=1}^{4} \mathcal{B}_i}, \tag{4.1}$$

We do the centrality reweight and normalized by N_{coll} to account for the following facts: 1) there is a difference in centrality distributions between data and MC for PbPb collisions; 2) and there is exactly one signal in each simulated event, while more in real data.
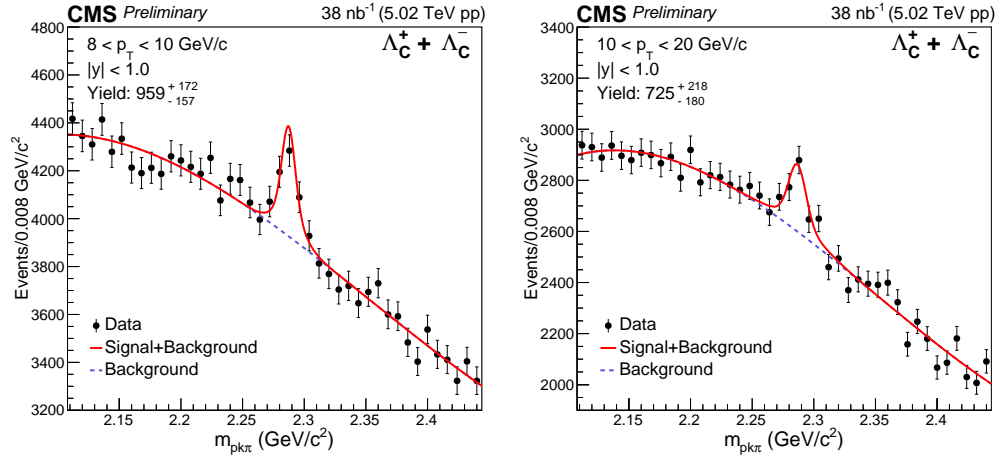
Figure 4.6. Λ_c^+ Signal Extraction In pp Collisions For p_T Ranges: 8–10 GeV/c (Left) And 10–20 GeV/c (Right). The Red Line Is The Function For The Foreground And The Blue Dashed Line Is The Function For The Background.
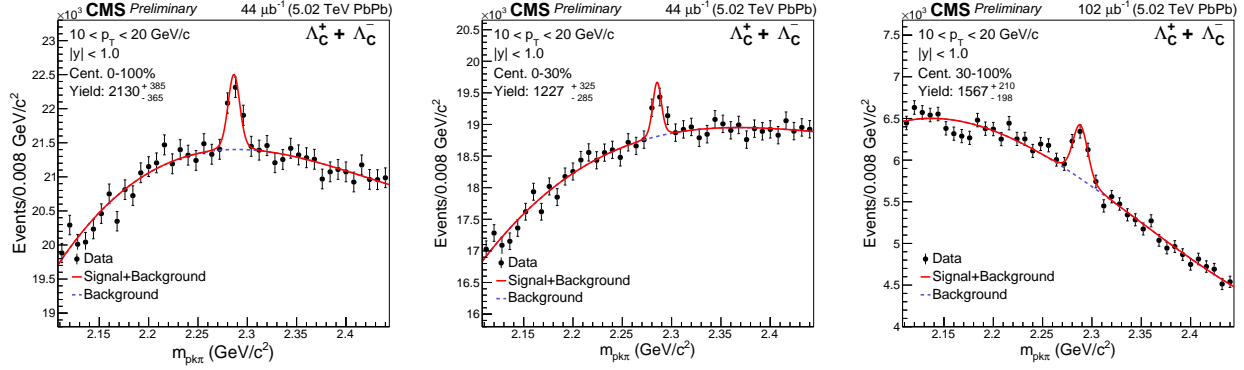
Figure 4.7. Λ_c^+ Signal Extraction In PbPb Collisions For p_T Range 10–20 GeV/c In Centrality Class 0–100% (left), 0–30% (Middle) And 30–100% (Right).The Red Line Is The Function For Foreground And The Blue Dashed Line Is The Function For The Background.

When calculating $\alpha\epsilon_{reco}$, a p_T weight is included to avoid the difference between the p_T shapes from the simulation and real data. The reweight is defined as follows:

$$weight = \frac{\Lambda_c^+ \ p_T \text{ spectrum}}{\text{gen-level } \Lambda_c^+ \ p_T \text{ spectrum}} \tag{4.2}$$

For pp, we do the p_T reweight as discussed above. The p_T weight is done for several times until the values of $\alpha\epsilon$ is converged. But for PbPb, we only have one p_T bin for centrality ranges 0–100%, 0–30% and 30–100%. The p_T function is obtained via the m_T scaling from the measurement of D^0 invariant yield in 0–100% centrality[41], [64] since this is the only centrality bin where both Λ_c^+ and D^0 have results. Under this scaling assumption, the invariant yields of Λ_c^+ and D^0 vs transverse mass $m_T = \sqrt{p_T^2 + m^2}$ are the same. From $m^2(\Lambda_c^+) + p_T^2(\Lambda_c^+) = m^2(D^0) + p_T^2(D^0)$, the invariant yield distribution for Λ_c^+ from D^0 can be obtained. Figure 4.9 and Figure 4.10 show the invariant yield of prompt and nonprompt Λ_c^+ (normalized by T_{AA}) from m_T scaling. The m_T scaling is not used in pp collisions, because at low p_T, there could be significant medium effect according to the model.

There is one additional correction applied to $\alpha\epsilon_{reco}$ for the PbPb data set. Previous CMS results have found more suppression for prompt than nonprompt D^0 mesons [41], [64], which can be quantified for $10 < p_T < 20$ GeV/c as $R_{AA}^{\text{nonprompt}}/R_{AA}^{\text{prompt}} = 1.66 \pm 0.38$. As nonprompt baryons tend to have greater p_T and decay farther from the collision point than
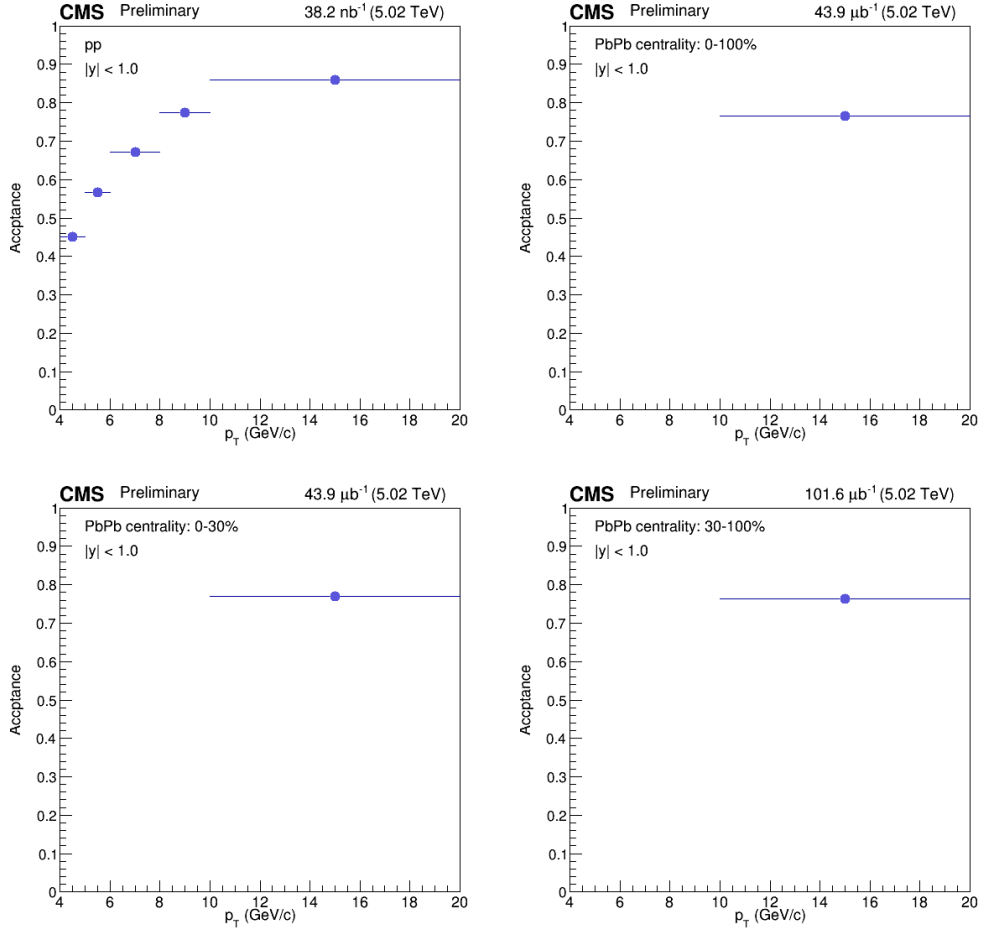
Figure 4.8. The Λ_c^+ Acceptance As A Function Of p_T In pp Collision As Well As PbPb In 0–30%, 0–100% And 30–100% Centrality Bins.
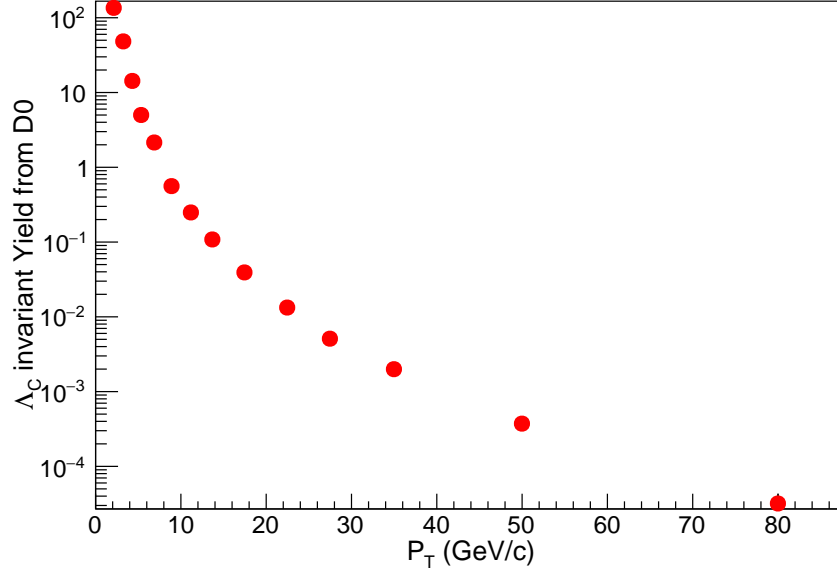
Figure 4.9. Invariant Yield Of Prompt Λ_c^+ Derived From m_T Scaling Of Prompt D^0.
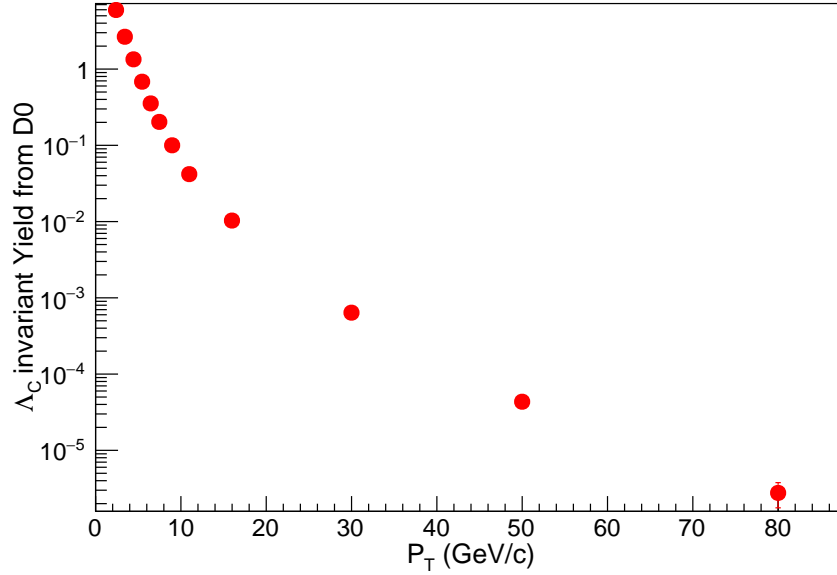
Figure 4.10. Invariant Yield Of Nonprompt Λ_c^+ Derived From m_T Scaling Of Nonprompt D^0.

prompt baryons, $\alpha\epsilon_{reco}$ is larger for nonprompt baryons. Changing the nonprompt fraction to account for the different suppression increases $\alpha\epsilon_{reco}$ by 15%.

Figure 4.11 shows the acceptance×efficiency for both pp and PbPb (all centrality bins). Because the optimized cuts for pp are looser than PbPb and the multiplicity for pp is smaller than that of PbPb collisions, the acceptance×efficiency for pp is higher than PbPb as we expected.

4.4 Systematic Uncertainties

This section presents the studies of systematic uncertainties. Systematic uncertainties arise from the extraction of the raw signal yield, the ability of the MC simulation to reproduce the combined acceptance and efficiency, the branching fraction of the decay mode, and the integrated luminosity [1]. The systematic uncertainty studies are discussed in detail below:

- The systematic uncertainty in the signal yields is obtained by varying the modeling functions that are used for the signal and background contributions.

    - The background function is changed from the default third- to second- and fourth-order Chebyshev polynomials. The maximum difference in yield between these two alternative functions and the default fit function is taken as the systematic uncertainty.

    - The default signal model function is the sum of two Gaussian functions with parameters chosen as described in Section 4.2. For the pp (PbPb) collision data, the alternative model is a triple (single) Gaussian function with similar procedures used for the parameters.

    - As the signal width is fixed for 5–6 GeV/c in pp collisions, an additional systematic uncertainty is assessed by varying the width by ±40%, corresponding to the maximum deviations with respect to the simulation observed in other p_T bins in pp and PbPb collisions.
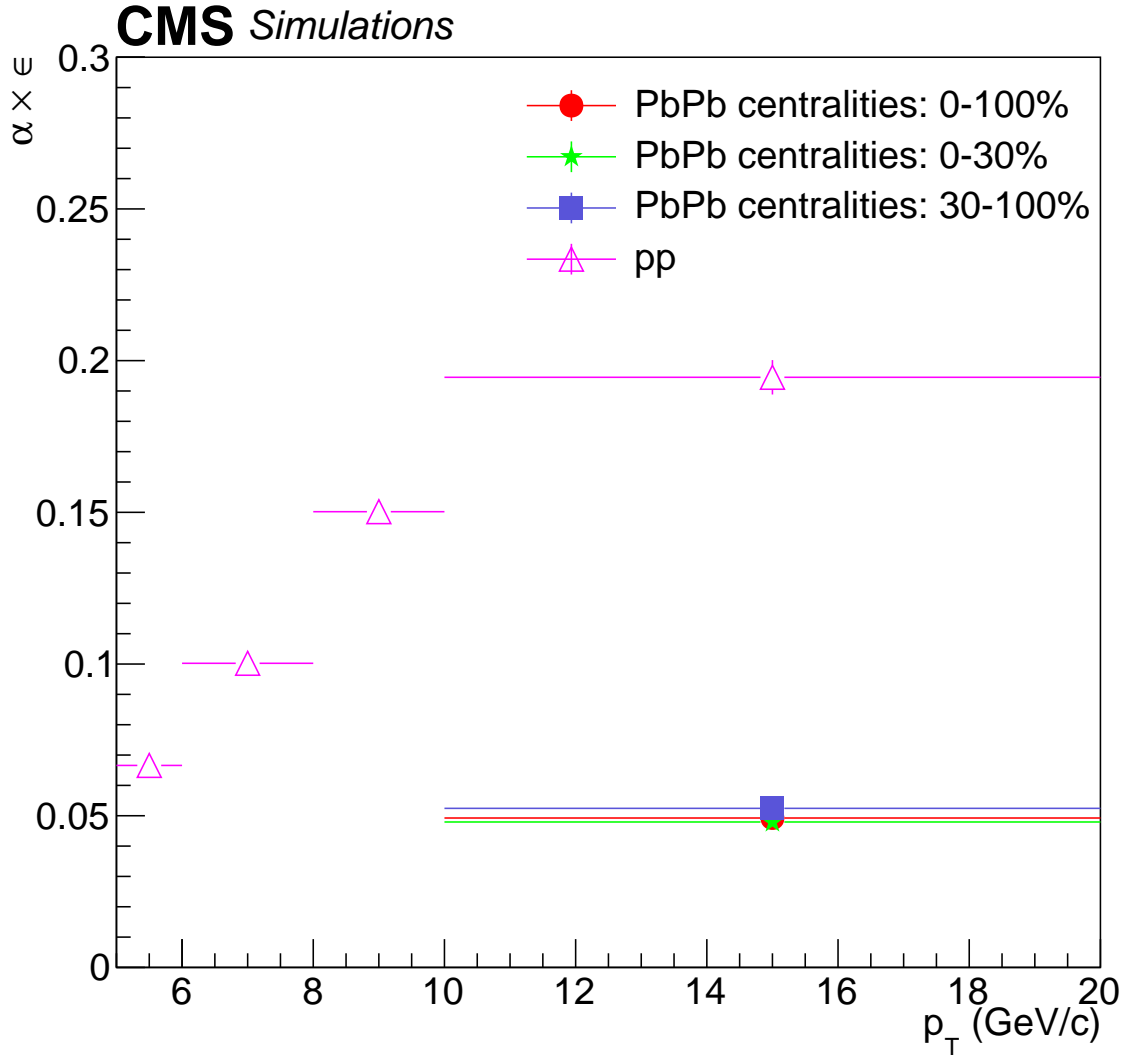
Figure 4.11. The $\alpha\epsilon$ In PbPb Of Three Centrality Bins And pp Collisions. The Closed Squares, The Closed Stars And The Closed Circles Represent $\alpha\epsilon$ In PbPb Collisions Of Centrality Range 30–100%, 0–30% And 0–100%, Respectively. The Pink Triangles Represent $\alpha\epsilon$ Of pp Collisions.

- The uncertainty measures the effect of the selection criteria variation. We define a double ratio as:

$$\mathcal{DR} = \frac{N_{\text{Data}}(\text{varied})}{N_{\text{Data}}(\text{nominal})} \bigg/ \frac{N_{\text{MC}}(\text{varied})}{N_{\text{MC}}(\text{nominal})} \, , \tag{4.3}$$

where $N_{\text{Data}}(\text{nominal})$ and $N_{\text{Data}}(\text{varied})$ are the yields obtained from data using the default and alternative selection criteria, respectively, and $N_{\text{MC}}(\text{nominal})$ and $N_{\text{MC}}(\text{varied})$ are the corresponding yields from the simulated events.

For each of the topological selection criteria, the double ratio is evaluated at many different values of the selection criterion. For all but the α cut in PbPb collisions, $\mathcal{DR}$ is plotted as a function of the selection value and fit to a linear function. The difference between unity and the value of the fitted line at the point where no selection is applied, is taken as the systematic uncertainty. For the α requirement in PbPb collisions, the systematic uncertainty is obtained from the biggest differences between unity and the value of $\mathcal{DR}$ from all of the alternative selection values. Combining the results of the three topological selection criteria systematic uncertainties in quadrature results in final uncertainties due to selection cut for both pp and PbPb collisions [1].

- a potential mismodeling of the p_T distribution of Λ_{c}^+ baryons because $\alpha\epsilon$ is strongly dependent on the Λ_{c}^+ p_T. In pp collisions, the default p_T shape is derived from the data. For PbPb collisions, the default p_T shape is obtained from m_{T} scaling of the measured D^0 p_T spectrum. For each data set, two alternative p_T spectra, one from PYTHIA8 and one from PYTHIA8 with color reconnection (will be described in Section 4.5) are considered and the maximum deviation in $A\epsilon$ is taken as the systematic uncertainty [1].

- imprecise knowledge of the resonant substructure of the $pK^-\pi^+$ decay mode [2]. The $\alpha\epsilon$ is the weighted sum of the four known sub-channels. The branching ratio for each sub-channel has an uncertainty [2]. The systematic uncertainty associated with this is evaluated by determining $\alpha\epsilon$ for each sub-channel and randomly adjusting the weights by the uncertainties of each branching fraction. The systematic uncertainty is obtained

from the standard deviation of a Gaussian fit to the different average $\alpha\epsilon$ values for both pp and PbPb events [1].

- the track reconstruction efficiency, which is 4% for pp collisions [41] and 5% for PbPb collisions [65]. As there are three tracks in the Λ_c^+ decay, the corresponding uncertainties on the measured p_T spectra are 12 and 15% for pp and PbPb, respectively, while for the Λ_c^+/D^0 production ratio, the uncertainties are 4 and 5%, respectively [1].

- possible mismodeling of the nonprompt component, namely Λ_c^+ from hadron decays, in the inclusive Λ_c^+ sample. The inclusive $\alpha\epsilon$ is the weighted sum of prompt and nonprompt $\alpha\epsilon$ according to the prompt and nonprompt fractions. As found using the standard PYTHIA8 MC sample, the nonprompt $\alpha\epsilon$ is generally 3-4 times larger than the prompt $\alpha\epsilon$ and so an incorrect nonprompt fraction in PYTHIA8 will result in an incorrect $\alpha\epsilon$ for the inclusive sample. To evaluate this systematic uncertainty, an alternative method is used to obtain the final result based on a fixed-order plus next-to-leading logarithm (FONLL) calculation [66]. Since there is no direct predictions for Λ_c^+ cross sections in FONLL, a generator-only PYTHIA8 sample of nonprompt Λ_c^+ events is reweighted to match the p_T-differential hadron cross section from a fixed-order plus next-to-leading logarithm (FONLL) calculation [66]. The resulting p_T-differential cross section for nonprompt Λ_c^+ baryons is multiplied by the appropriate luminosity, branching fractions, and $\alpha\epsilon$ for nonprompt Λ_c^+ events to obtain an estimate of the number of reconstructed nonprompt Λ_c^+ baryons in each p_T bin. Subtracting this value from the measured number of reconstructed Λ_c^+ baryons gives the number of reconstructed prompt Λ_c^+ baryons. These reconstructed prompt yields are then corrected using the prompt $\alpha\epsilon$ as well as luminosity and branching fractions to estimate the p_T-differential cross section for prompt Λ_c^+ baryons. Finally, the two cross sections give an alternative estimate of the nonprompt fraction in each p_T bin, and therefore an alternative estimate of the weighted inclusive $\alpha\epsilon$ value. The systematic uncertainty is taken as the difference between the nominal and alternative $\alpha\epsilon$ values. Besides the same method which is applied to pp collision for PbPb collisions, an additional systematic

uncertainty is assessed by taking the difference between applying and not applying the correction for different values of R_{AA} for nonprompt and prompt Λ_c^+ baryons [1].

- The overall $\Lambda_c^+ \to pK^- \pi^+$ branching fraction uncertainty is 5.3% [2]. The uncertainties in the integrated luminosity in pp collisions and the MB selection efficiency in PbPb collisions are 2.3% [67] and 2.0% [68], respectively. The uncertainties in T_{AA} are listed in Table 4.5.

For the measurement of the p_T spectra, the uncertainties associated with the $\Lambda_c^+ \to pK^- \pi^+$ branching fraction and subresonant contributions, the luminosity and MB selection efficiency, and the nonprompt fraction contribute only to the overall normalization and are labeled global uncertainties. Adding these contributions in quadrature yields global uncertainties of 21% (31%) for pp (PbPb) collisions. In measuring the nuclear modification factor R_{AA}, the uncertainties associated with the branching fraction and subresonant contributions cancel and the nonprompt fraction uncertainty partially cancels. In calculating the Λ_c^+/D^0 production ratio, the uncertainties associated with D^0 from the yield extraction, selection criteria efficiency, and p_T shape are obtained from Ref. [41], while the uncertainties in the integrated luminosity in pp collisions and the MB selection efficiency in PbPb collisions cancel [1]. The overview for the relative systematic uncertainties for all the measurements are in Tab. 4.6-4.10.

Table 4.5. Summary Of The $\langle N_{\mathrm{coll}} \rangle$, $\langle T_{\mathrm{AA}} \rangle$, And $\langle N_{\mathrm{part}} \rangle$ Values For Three PbPb Centrality Ranges At 5.02 TeV.

Centrality	$\langle T_{\mathrm{AA}} \rangle [\mu b^{-1}]$	$\langle N_{\mathrm{part}} \rangle$	$\langle N_{\mathrm{coll}} \rangle$
0–30%	$15.41^{+0.33}_{-0.47}$	$270.7^{+3.2}_{-3.4}$	1079^{+74}_{-78}
30–100%	$1.41^{+0.09}_{-0.06}$	$46.8^{+2.4}_{-1.2}$	98^{+8}_{-6}
0–100%	$5.61^{+0.16}_{-0.19}$	$114.0^{+2.6}_{-2.6}$	393^{+26}_{-28}

4.5   Results

This section presents the p_T-differential cross section and R_{AA} of inclusive Λ_c^+ in both pp and PbPb collisions (within three centrality classes), and the Λ_c^+/D^0 production ratio in both pp and PbPb collisions (within centrality: 0–100%).

Table 4.6. Summary Of Relative Systematic Uncertainties Of Inclusive Λ_c^+ Cross Section In pp Collisions At 5.02 TeV With CMS 2015 Data.

Source	p_T interval(GeV/c)			
	5–6	6–8	8–10	10–20
Inv. mass fit(Background PDF)	5.4%	4.4%	6.6%	10.2%
Inv. mass fit(Signal PDF)	27.9%	4.0%	4.7%	3.2%
Tracking efficiency	12%			
Selection efficiency	5.6%			
MC p_T shape	0.1%	0.7%	0.5%	2.6%
Total bin by bin	31.4%	14.5%	15.5%	17.2%
$\alpha\epsilon$	8.1%			
nonprompt fraction	18%			
Luminosity	2.3%			
Branching ratio	5.3%			

Table 4.7. Summary Of Relative Systematic Uncertainties Of Inclusive Λ_c^+ Differential Yield From Data For 5.02 TeV PbPb Collisions With Three Centrality Ranges With CMS 2015 Data.

Source	PbPb 30–100%	PbPb 0–30%	PbPb 0–100%
	10–20GeV/c	10–20GeV/c	10–20GeV/c
Inv. mass fit(Background PDF)	8.6%	6.6%	9.0%
Inv. mass fit(Signal PDF)	3.1%	3.7%	2.1%
Tracking efficiency	15%		
Selection efficiency	18.9%		
MC p_T shape	5.2%		
Total bin by bin	26.3%	25.8%	26.3%
$\alpha\epsilon$	8.1%		
nonprompt fraction	29%		
N_{events} PbPb	2%		
Branching ratio	5.3%		

58

Table 4.8. Summary Of Relative Systematic Uncertainties From Data For Inclusive Λ_c^+ R_{AA} At 5.02 TeV PbPb Collisions For Centrality 0–100%, 0–30% And 30–100% With CMS 2015 Data.

Source	PbPb 30–100%	PbPb 0–30%	PbPb 0–100%
	10–20GeV/c	10–20GeV/c	10–20GeV/c
Inv. mass fit pp(Background PDF)	10.2%	10.2%	10.2%
Inv. mass fit pp(Signal PDF)	3.2%	3.2%	3.2%
Inv. mass fit PbPb(Background PDF)	8.6%	6.6%	9.0%
Inv. mass fit PbPb(Signal PDF)	3.1%	3.7%	2.1%
Tracking efficiency	19%		
Selection efficiency pp	5.6%		
Selection efficiency PbPb	18.9%		
MC p_T shape pp	2.6%	2.6%	2.6%
MC p_T shape PbPb	5.2%	5.2%	5.2%
Total bin by bin	31.3%	30.9%	31.4%
nonprompt fraction	20.9%		
Luminosity	2.3%		
N_{events} PbPb	2%		

Table 4.9. Summary Of Relative Systematic Uncertainties For The Λ_c^+/D^0 (Inclusive Λ_c^+ And Prompt D^0) Production Ratio In pp Collisions At 5.02 TeV With CMS 2015 Data.

Source	p_T interval (GeV/c)			
	5–6	6–8	8–10	10–20
Inv. mass fit Λ_c^+(Background PDF)	5.4%	4.4%	6.6%	10.2%
Inv. mass fit Λ_c^+(Signal PDF)	27.9%	4.0%	4.7%	3.2%
Inv. mass fit D^0	3%	3%	1.7%	4.0%
Tracking efficiency	4%			
Selection efficiency Λ_c^+	5.6%			
Selection efficiency D^0	3.6%			
MC p_T shape Λ_c^+	0.1%	0.7%	0.5%	2.6%
MC p_T shape D^0	2.0%	1.0%	1.0%	1.0%
Total bin by bin	29.7%	10.3%	11.4%	14.1%
$\alpha\epsilon$	8.1%			
nonprompt fraction	18%			
$\mathcal{B}$ (Λ_c^+)	5.3%			
$\mathcal{B}$ (D^0)	1.3%			

Table 4.10. Summary Of Relative Systematic Uncertainties For The Λ_c^+/D^0 (Inclusive Λ_c^+ And Prompt D^0) Production Ratio In PbPb Collisions At 5.02 TeV In The Centrality Range 0–100% With CMS 2015 Data.

Source	p_T interval (GeV/c)
	10–20
Inv. mass fit Λ_c^+(Background PDF)	9.0%
Inv. mass fit Λ_c^+(Signal PDF)	8.0%
Inv. mass fit D^0	6.5%
Tracking efficiency	5%
Selection efficiency Λ_c^+	18.9%
Selection efficiency D^0	1%
MC p_T shape Λ_c^+	5.2%
MC p_T shape D^0	3.5%
Total bin by bin	23.5%
$\alpha\epsilon$	7.9%
nonprompt fraction	29%
$\mathcal{B}\,(\Lambda_c^+)$	5.3%
$\mathcal{B}\,(D^0)$	1.3%

The inclusive Λ_c^+ p_T-differential cross section in pp collisions is defined as

$$\left.\frac{d\sigma_{\rm pp}^{\Lambda_c^+}}{dp_T}\right|_{|y|<1} = \frac{1}{2\mathcal{L}\Delta p_T \mathcal{B}} \frac{N_{\rm pp}^{\Lambda_c^+}|_{|y|<1}}{\alpha\epsilon} , \qquad (4.4)$$

where $N_{\rm pp}^{\Lambda_c^+}|_{|y|<1}$ is the Λ_c^+ yield extracted in each p_T bin, $\mathcal{L}$ is the integrated luminosity, Δp_T is the width of each p_T bin, $\mathcal{B}$ is the branching ratio of the decay, and $\alpha\epsilon$ is the product of the acceptance and efficiency. The factor of $\frac{1}{2}$ accounts for averaging the particle and antiparticle contributions.

The inclusive Λ_c^+ cross section in PbPb collisions is presented as

$$\frac{1}{\langle T_{\rm AA}\rangle} \left.\frac{dN_{\rm PbPb}^{\Lambda_c^+}}{dp_T}\right|_{|y|<1} = \frac{1}{\langle T_{\rm AA}\rangle} \frac{1}{2N_{\rm events}\Delta p_T \mathcal{B}} \frac{N_{\rm PbPb}^{\Lambda_c^+}|_{|y|<1}}{\alpha\epsilon} , \qquad (4.5)$$

where $N_{\rm events}$ is the number of MB events used for the analysis and $\langle T_{\rm AA}\rangle$ is the nuclear overlap function, which is the average number of nucleon-nucleon (NN) binary collisions ($\langle N_{\rm coll}\rangle$) divided by the NN cross section, and can be interpreted as the NN-equivalent integrated luminosity per heavy ion collision.

The values of $\langle T_{\rm AA}\rangle$, $\langle N_{\rm coll}\rangle$, and the average number of participating nucleons ($\langle N_{\rm part}\rangle$), generated with a Glauber model [28], are the averages of these quantities over events in the given centrality range, and are listed in Table 4.5.

Figure 4.12 shows the p_T-differential cross section of inclusive Λ_c^+ baryon production in pp collisions for the range of $5 < p_T < 20$ GeV/c and the $T_{\rm AA}$-scaled yields in PbPb collisions for the range of $10 < p_T < 20$ GeV/c, for three centrality classes. The 21% (31%) normalization uncertainty for the pp (PbPb) results is not included in the boxes representing the systematic uncertainties for each data point. While the shape of the p_T distribution in pp collisions is consistent with the inclusive production calculation from PYTHIA8 using tune CUETP8M1 and activating the "SoftQCD:nondiffractive" processes, the data are systematically higher. The hadronization in PYTHIA8 can be modified by adding a color reconnection (CR) mechanism in which the final partons in the string fragmentation are considered to be color connected in such a way that the total string length becomes as short as possible [69]. The calculations using the recommended color reconnection model from Ref. [69] are consis-

tent with our p_T-differential cross section in pp collisions. The p_T-differential cross section in pp collisions is also compared to the GM-VFNS perturbative QCD calculations [70], which includes only prompt Λ_c^+ baryon production. The GM-VFNS prediction is significantly below our data for $p_T < 10$ GeV/c, similar to the difference found by ALICE [48]. PYTHIA8 predicts that 8–15% of generated Λ_c^+ baryons arise from hadrons, with the low (high) value corresponding to the Λ_c^+ p_T interval $5 < p_T < 6$ GeV/c ($10 < p_T < 20$ GeV/c). Therefore, accounting for the effects of nonprompt Λ_c^+ production will only marginally reduce the disagreement with the GM-VFNS prediction [1].

The nuclear modification factor, R_{AA} of Λ_c^+ is defined as the followings:

$$R_{\mathrm{AA}}(p_T) = \frac{1}{\langle T_{\mathrm{AA}} \rangle} \frac{dN_{\mathrm{PbPb}}^{\Lambda_c^+}}{dp_T} \Big/ \frac{d\sigma_{\mathrm{pp}}^{\Lambda_c^+}}{dp_T} \ . \tag{4.6}$$

The nuclear modification factor R_{AA} for inclusive Λ_c^+ baryons in the p_T range 10–20 GeV/c is shown in Fig. 4.13 as a function of the number of participating nucleons $\langle N_{\mathrm{part}} \rangle$ for PbPb collisions. The results suggest that Λ_c^+ is suppressed in PbPb collisions for $p_T > 10$ GeV/c, but no conclusion can be drawn because of the large uncertainties. The difference in R_{AA} values between the 0–30% and 30–100% centrality ranges is consistent with an enhanced suppression in the more central PbPb collisions [1].

Figure 4.14 shows the Λ_c^+/D^0 production ratio as a function of p_T for pp collisions and PbPb collisions in the centrality range 0–100%. The production ratio found from pp collisions is similar in shape versus p_T but about three times larger in magnitude compared to the calculation from PYTHIA 8.212 tune CUETP8M1. Results using the Monash 2013 [71] tune are found to be consistent with those from the CUETP8M1 tune. Besides providing a reasonable description of Λ_c^+ baryon p_T-differential cross sections, Fig. 4.14 shows that calculations using a color reconnection model are consistent with our results for the Λ_c^+/D^0 production ratio in pp collisions [1].
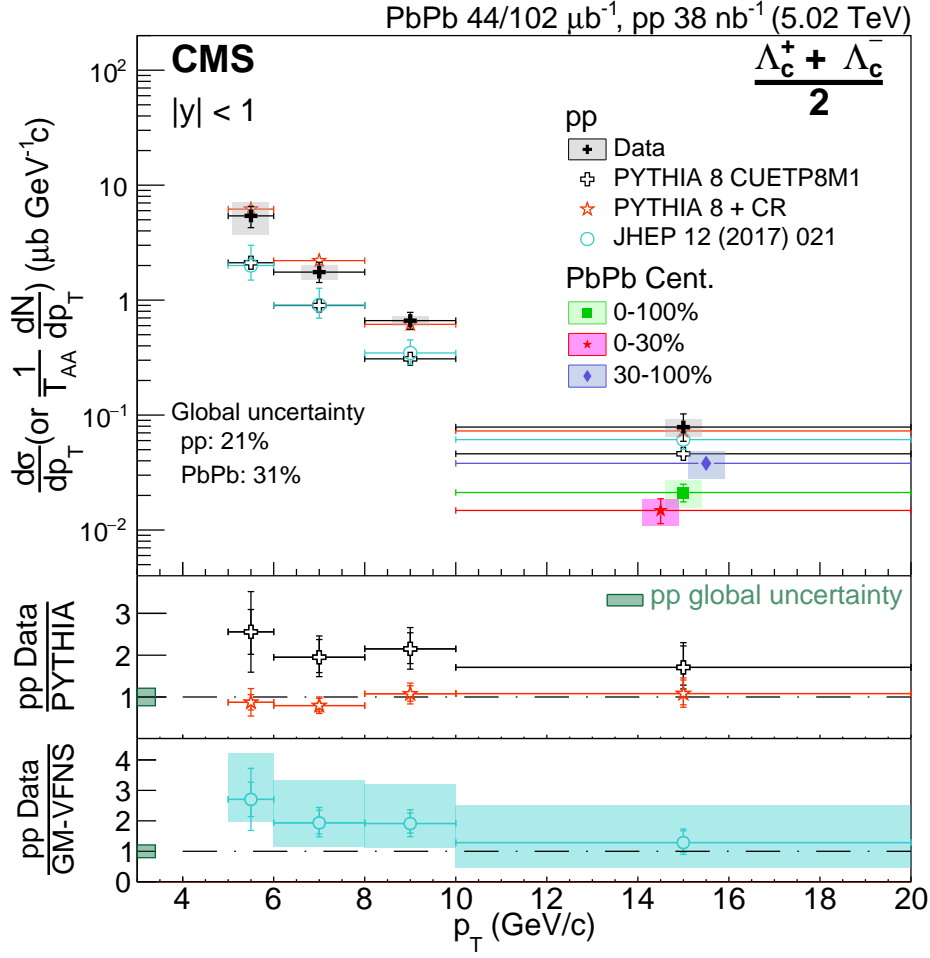
Figure 4.12. The p_T-differential Cross Sections For Inclusive Λ_c^+ Production In pp Collisions And The T_{AA}-scaled Yields For Three Centrality Regions Of PbPb Collisions. The Boxes And Error Bars Represent The Systematic And Statistical Uncertainties, Respectively. The PbPb Data Points Are Shifted In The Horizontal Axis For Clarity. Predictions For pp Collisions Are Displayed For PYTHIA8 With The CUETP8M1 Tune (Open Crosses), PYTHIA8 With Color Reconnection [69] (Open Stars), And GM-VFNS [70] (Open Circles Labeled "JHEP 12 (2017) 021") Along With Ratios To The Data In The Lower Two Panels. The PYTHIA8 (GM-VFNS) Predictions Are For Inclusive (Prompt) Λ_c^+ Production. The Error Bars On The GM-VFNS Prediction Account For The Scale Variation Uncertainty. The Lower Panels Show The Data-to-prediction Ratio For pp Collisions With Inner And Outer Error Bars Corresponding To The Statistical And Total Uncertainty In The Data, Respectively, And The Shaded Box At Unity Indicating The 21% Normalization Uncertainty. The Shaded Boxes In The Bottom Panel Represent The GM-VFNS Uncertainty. This Figure Is Taken From Ref. [1].
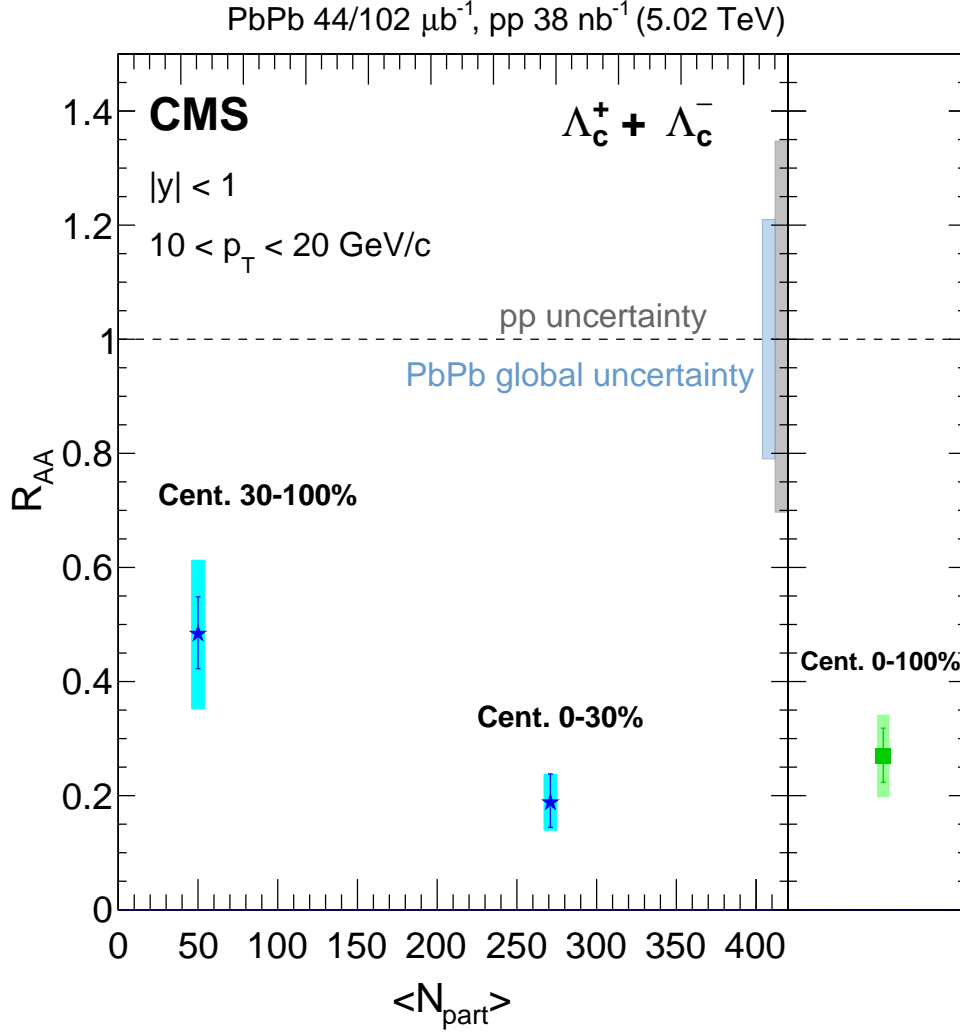
Figure 4.13. The Nuclear Modification Factor R_{AA} Versus $\langle N_{part} \rangle$ For Inclusive Λ_c^+ Production. The Error Bars Represent The PbPb Yield Statistical Uncertainties. The Boxes At Each Point Include The PbPb Systematic Uncertainties Associated With The Signal Extraction, p_T Spectrum, Selection Criteria, Track Reconstruction, And T_{AA}. The Band At Unity Labeled pp Uncertainty Includes These Same Uncertainties For The pp Data (Except For T_{AA}) Plus The Uncertainties In pp Yield And Luminosity. The Band At Unity Labeled PbPb Includes The Uncertainty From The Nonprompt Fraction (Accounting For A Partial Cancellation Between pp And PbPb) And MB Selection Efficiency. This Figure Is Taken From Ref. [1].

64
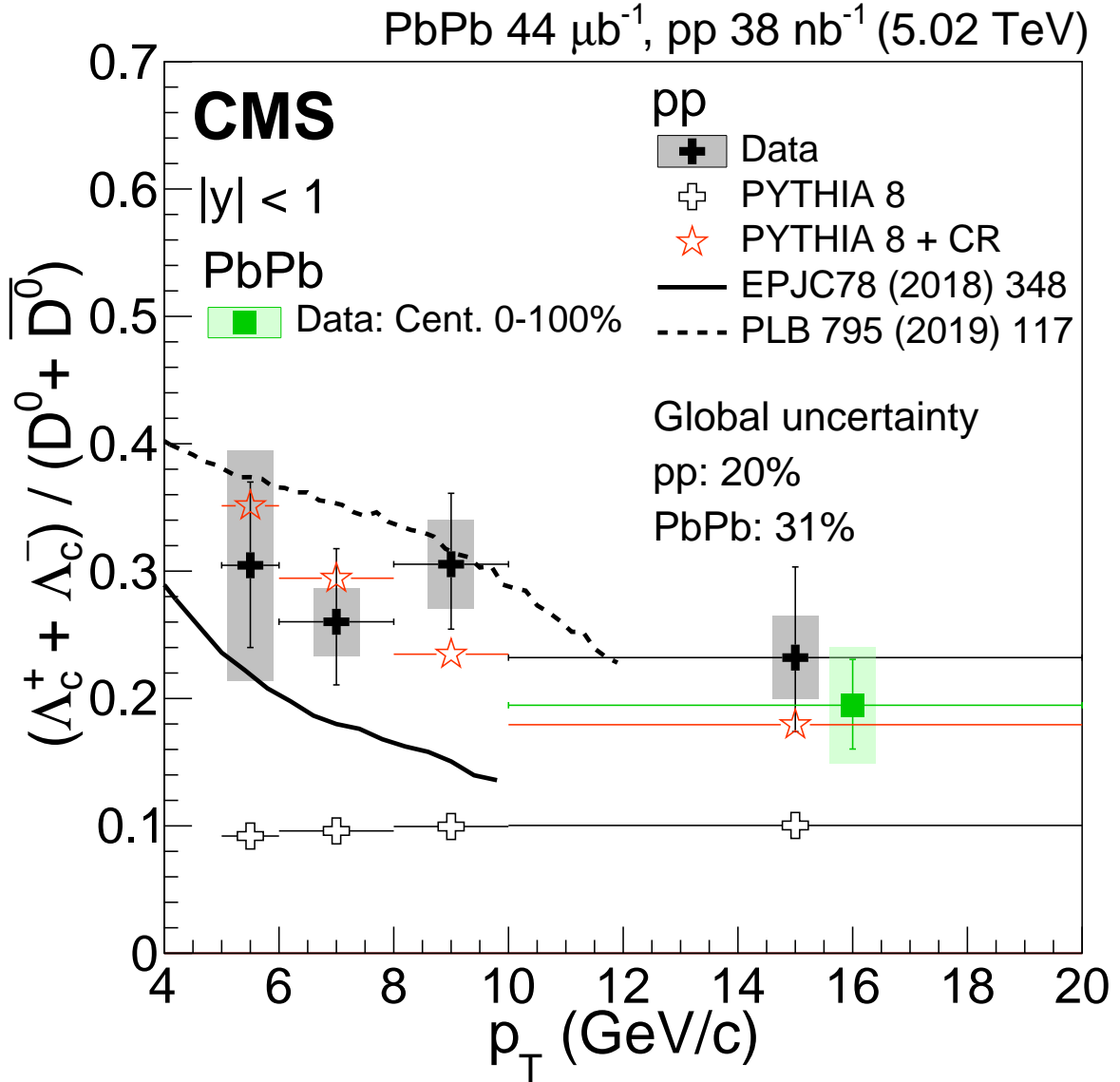
Figure 4.14. The Ratio Of The Production Cross Sections Of Inclusive Λ_c^+ To Prompt D^0 Versus p_T From pp Collisions As Well As 0–100% Centrality PbPb Collisions. The Boxes And Error Bars Represent The Systematic And Statistical Uncertainties, Respectively. The PbPb Data Point Is Shifted In The Horizontal Axis For Clarity. The 20 And 31% Normalization Uncertainties In pp And PbPb Collisions, Respectively, Are Not Included In The Boxes Representing The Systematic Uncertainties For Each Data Point. The Open Crosses And Open Stars Represent The Predictions Of PYTHIA8 With The CUETP8M1 Tune And With Color Reconnection [69], Respectively. The Solid And Dashed Lines Are The Calculations For Prompt Λ_c^+ Over Prompt D^0 Production Ratio From Ref. [47] and Ref. [72], Respectively. All Predictions Are For pp Collisions. This Figure Is Taken From Ref. [1].

5. PRODUCTION OF PROMPT Λ_c^+ IN PP AND PBPB COLLISIONS AT 5.02 TEV WITH 2017 AND 2018 CMS DATA

This chapter presents the details of the measurements of prompt Λ_c^+ with 2017 and 2018 CMS data. Since the luminosity of 2017 pp and 2018 PbPb is 6 and 13 times larger than 2015 CMS data, respectively, lower and higher p_T ranges could be achieved and the prompt component of Λ_c^+ could be distinguished from data.

5.1 Data Sets And Monte Carlo Simulation

This analysis is performed using 2017 pp and 2018 PbPb data at $\sqrt{s_{\mathrm{NN}}} = 5.02$ TeV. The luminosity for Zerobias pp and MinimumBias PbPb is 252 nb^{-1} and 0.58 nb^{-1}, respectively. Details of the data sets for prompt Λ_c^+ analysis are summarized in Table 5.1. The good

Table 5.1. CMS 2017 And 2018 Data Sets Used In The Prompt Λ_c^+ Production Analysis.

sample	DAS name	Global Tag
pp	/HIZeroBias1-12/Run2017G-17Nov2017-v1/AOD	94X_dataRun2_ReReco_EOY17_v6
PbPb	/HIMinimumBias0-19/HIRun2018A-04Apr2019-v1/AOD	103X_dataRun2_Prompt_fixEcalADCToGeV_v1

quality of the data is ensured by applying the JSON file for pp and PbPb respectively. (JSON files has been introduced in 4.1.)

- Cert_306546-306826_5TeV_EOY2017ReReco_Collisions17_JSON.txt

- Cert_326381-327564_HI_PromptReco_Collisions18_JSON.txt

pp and PbPb samples were reconstructed using CMSSW version CMSSW_9_4_10 and CMSSW_10_3_3_patch1.

5.1.1 Event Selection

This analysis uses samples collected from Zero-bias and Minimum-bias triggers. Event selections are used to reject noise and beam-background event.

The following offline event selection criteria are applied to each PbPb event to remove background from the sources such as beam-gas collisions, beam scraping events and electromagnetic interactions (ultra-peripheral collisions):

- pprimaryVertexFilter: In the B=3.8 T data, where tracks are reconstructed, requirement of a reconstructed 2-track primary vertex was imposed. In central events, the minimum p_T requirement was increased, and the tracking region was narrowed down, to keep the maximum number of fitted tracks stable around 40–60, ensuring time-efficient reconstruction. When tracks are not reconstructed, i.e. B= 0 T, the z-vertex position is obtained by maximizing the compatibility of pixel cluster length and global z-positions with a vertex hypothesis. The vertex is only accepted of it lies between ±25 cm from the center of the detector. The requirement of an accepted vertex removes non-inelastic collision events (e.g. beam-gas UPC) with large HF energy deposits but very few pixel hits.

- phfCoincFilter2Th4: This filter requires at least 2 towers on each side of the interaction point in the HF with tower above 4 GeV threshold. The requirement removes approximately 99% of UPC events.

- pclusterCompatibilityFilter: A particle traversing a pixel module at some angle leave a cluster with a width proportional to its angle of incidence. The expected width of the cluster can be determined by the particle pseudrapidity and z-position of the collision vertex. For a given z-position, one can determine the number of clusters in an event that have a width compatible with the hypothesis that the collision vertex was at the z-position. One can scan the z-axis to determine how many clusters are compatible with a vertex at each position. This technique can be used to locate the z-position of a collision vertex, or determine if a collision likely occurred outside the interaction region (i.e. beam scraping).

- $-15 < PVz < 15$: The primary vertex is required to be between $\pm$ 15 cm from the center of the detector in the z-direction.

5.2 Signal Extraction

In this section, Λ_c^+ candidates and signal yield extraction for pp and PbPb collision are described. Raw yield are extracted in each p_T interval via unbinned maximum likelihood fit to the invariant mass distribution. The fit function consists of the following components:

- a double Gaussian function with same mean but different widths and strengths to model the signal shape determined from MC in the each p_T bin for pp collisions; a triple Gaussian function with same mean but different widths and strengths to model the signal shape determined from MC in the each p_T bin for PbPb collisions.

- a Chebyshev polynomial function to model the combinatorial background and the swapped Λ_c^+ component for both pp and PbPb collisions. Previous CMS inclusive Λ_c^+ analysis [1] already shows that the distribution of swapped component is broad (about 30 times broader) and the shape is very closed to the combinatorial background. The detailed information is in 4.2. The order of the Chebyshev polynomial function is decided by LLR test. The default background fit function for PbPb collisions is Chebyshev pol3 function. The default background fit function for pp collisions is Chebyshev pol1, Chebyshev pol2 and Chebyshev pol3 for 3–5 GeV/c, 5–8 GeV/c, and 8–30 GeV/c.

We use the same strategy as that in the inclusive Λ_c^+ analysis [1] (which is described in 4.2): The signal shape is defined by the MC, and the float width parameter is to accommodate the difference of the signal shape between MC and data in all p_T bins.

5.3 Prompt Λ_c^+ Extraction by DCA Fit

The prompt and nonprompt Λ_c^+ are distinguished by fitting the data mix Λ_c^+ DCA distribution by a mixture of prompt and nonprompt Λ_c^+ DCA from MC samples. The Λ_c^+ DCA distributions for prompt and nonprompt Λ_c^+ from the MC are expected to be different. The prompt part should have a narrower distribution near 0 while the nonprompt
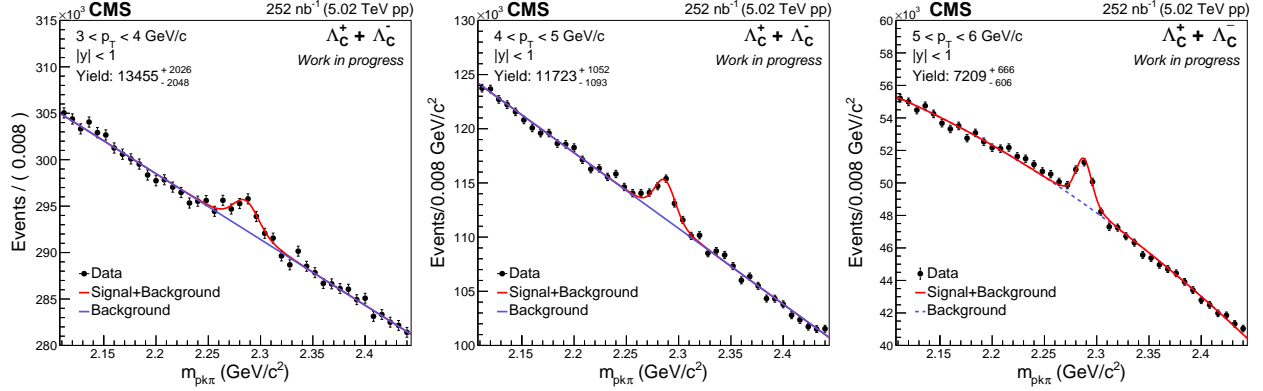
Figure 5.1. Invariant Mass Distribution Of Λ_c^+ Candidates With p_T=3–4 GeV/c (Left), 4–5 GeV/c (Middle) And 5–6 GeV/c In pp Collisions. The Solid Line Represents The Full Fit And The Dashed Line Represents The Background Component.
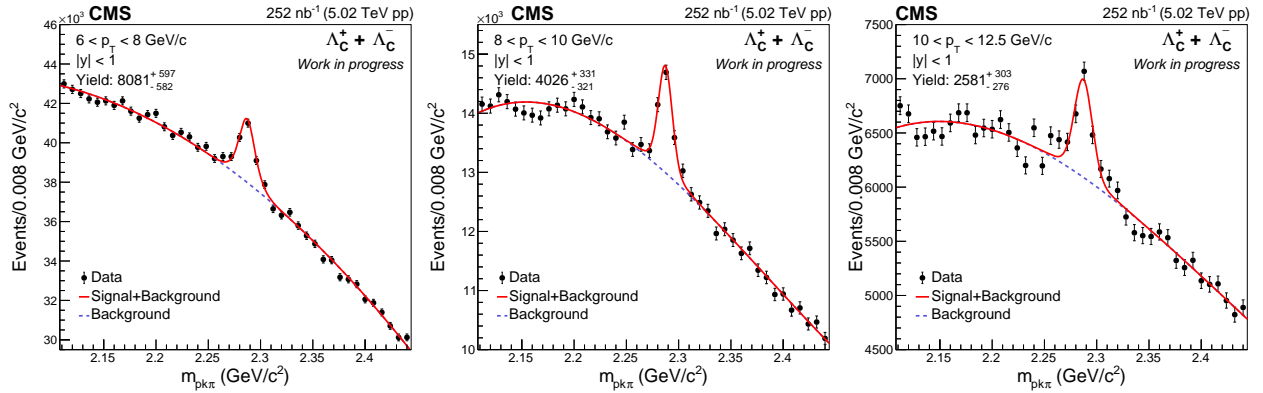
Figure 5.2. Invariant Mass Distribution Of Λ_c^+ Candidates With p_T=6–8 GeV/c (Left), 8–10 GeV/c (Middle) And 10–12.5 GeV/c In pp Collisions. The Solid Line Represents The Full Fit And The Dashed Line Represents The Background Component.

distribution is much wider. There could be a MC-data difference which could influence the prompt and nonprompt Λ_c^+ yields obtained by the Λ_c^+ DCA fit. To estimate this effect, the resolution from MC is scaled by an arbitrary number, and see which scale will lead to the best 2 component Λ_c^+ DCA fit (details below).

The best MC resolution effect scale to match the data is determined by a fit shown in Fig. 5.17. The best scale is at the minimum of $\chi2$ vs. scale. The statistic error of the fitted prompt ratio is assigned as the statistic error and the systematic error is assigned as

69
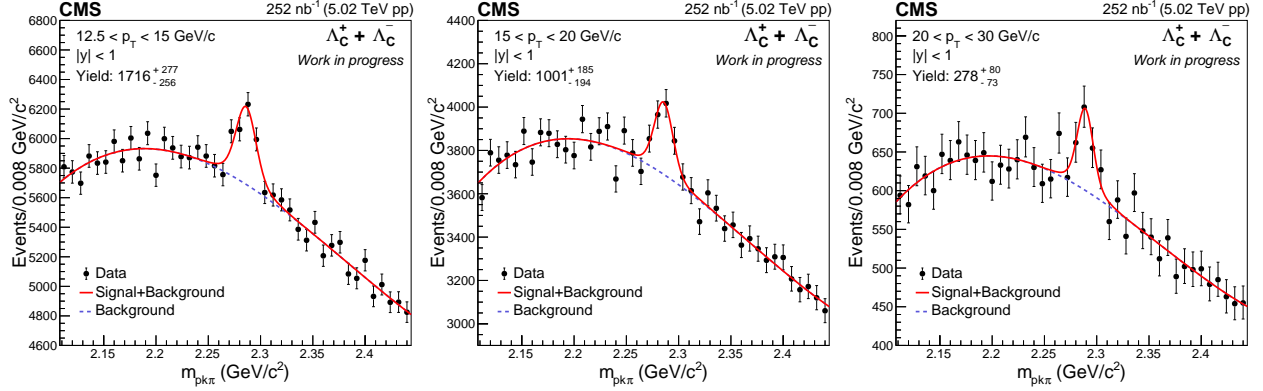
Figure 5.3. Invariant Mass Distribution of Λ_c^+ Candidates With p_T= 12.5–15 GeV/c (Left), 15–20 GeV/c (Middle) And 20–30 GeV/c In pp Collisions. The Solid Line Represents The Full Fit And The Dashed Line Represents The Background Component.

Figure 5.4. Invariant Mass Distribution Of Λ_c^+ Candidates With p_T= 6–8 GeV/c (Left), 8–10 GeV/c (Middle) And 10–20 GeV/c In PbPb Collisions Within The Centrality Range 0–90%. The Solid Line Represents The Full Fit And The Dashed Line Represents The Background Component.

the difference in prompt ratio between the minimal $\chi 2$ and minimal $\chi 2 + 2.3$ [2] or the best smearing DCA fit and DCA significance fit without any smearing .

The statistic of $p_T > 15$ GeV/c is quite low, and the signal shape is not obvious. The value of number of signal minus the statistical error hits a negative value, which leads to unreasonable fitted prompt ratio. Also, it is not able to extract the signal number for $3 < p_T < 4$ GeV/c. The PYTHIA prompt ratio shows that the prompt ratio for $p_T > 15$ GeV/c is closed to that of its neighbour bin ($12.5 < p_T < 15$ GeV/c), and also same case for

70

Figure 5.5. Invariant Mass Distribution Of Λ_c^+ Candidates With $p_T =$ 12.5–15 GeV/c (Left), 15–20 GeV/c (Middle) And 20–30 GeV/c In PbPb Collisions Within The Centrality Range 0–90%. The Solid Line Represents The Full Fit And The Dashed Line Represents The Background Component.

Figure 5.6. Invariant Mass Distribution Of Λ_c^+ Candidates With $p_T =$ 30–40 GeV/c (Left) In Centrality Range 0–90%, 10–12.5 GeV/c (Middle) And 12.5–15 GeV/c In PbPb Collisions Within The Centrality Range 0–10%. The Solid Line Represents The Full Fit And The Dashed Line Represents The Background Component.

$3 < p_T < 4$ GeV/c. Thus, the prompt ratio for 15–30 GeV/c is quoted as that for 12.5–15 GeV/c, and the prompt ratio for 3–4 GeV/c is quoted as that for 4–5 GeV/c. The systematic uncertainty due to prompt ratio for these three p_T bins (3–4, 15–20, and 20–30 GeV/c) will be assigned as the biggest difference between the quoted prompt ratio and that predicted by PYTHIA or next-to-leading logarithm (FONLL). There is no FONLL nonprompt Λ_c^+ cross section predictions, thus, a generator-only PYTHIA8 sample of nonprompt Λ_c^+ events
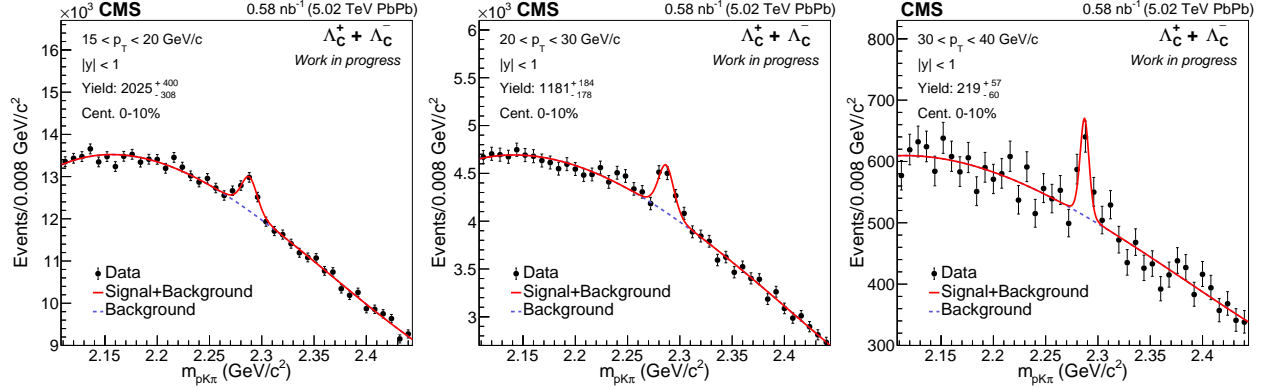
Figure 5.7. Invariant Mass Distribution Of Λ_c^+ Candidates With p_T= 15–20 GeV/c (Left), 20–30 GeV/c (Middle) And 30–40 GeV/c In PbPb Collisions Within The Centrality Range 0–10%. The Solid Line Represents The Full Fit And The Dashed Line Represents The Background Component.
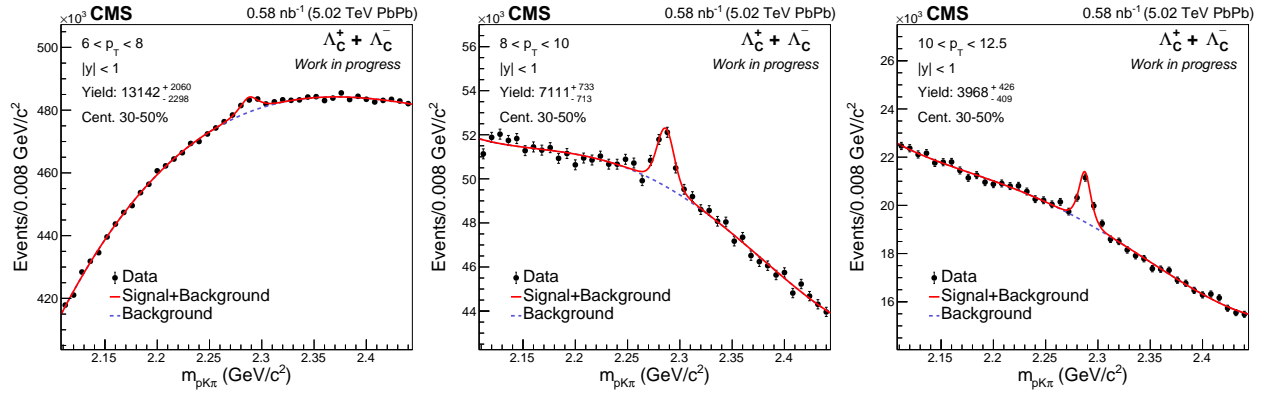
Figure 5.8. Invariant Mass Distribution Of Λ_c^+ Candidates With p_T= 6–8 GeV/c (Left), 8–10 GeV/c (Middle) And 10–12.5 GeV/c In PbPb Collisions Within The Centrality Range 30–50%. The Solid Line Represents The Full Fit And The Dashed Line Represents The Background Component.

is reweighted to match the p_T-differential b hadron cross section from FONLL calculation. The resulting p_T-differential cross section for nonprompt Λ_c^+ baryons is multiplied by the appropriate luminosity, branching fractions, and $\alpha\epsilon$ for nonprompt Λ_c^+ events to obtain an estimate of the nonprompt ratio of Λ_c^+. All the detailed information is listed in Table 5.2.

The s/b is so small for p_T=6–8 GeV/c, and 10–12.5 GeV/c in centrality class 0–90% and 0–10% in PbPb collisions that these two p_T bins could not do DCA fit. The prompt ratios
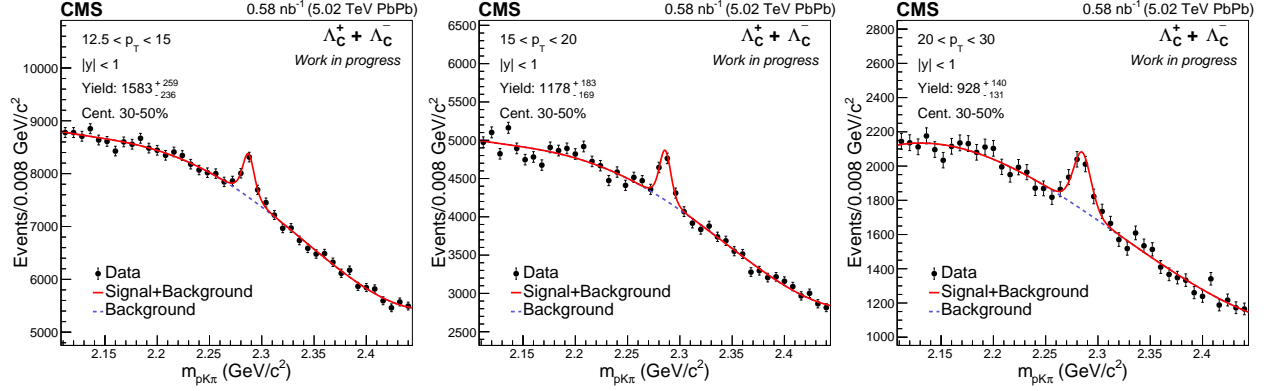
Figure 5.9. Invariant Mass Distribution Of Λ_c^+ Candidates With p_T= 12.5–15 GeV/c (Left), 15–20 GeV/c (Middle) And 20–30 GeV/c In PbPb Collisions Within The Centrality Range 30–50%. The Solid Line Represents The Full Fit And The Dashed Line Represents The Background Component.
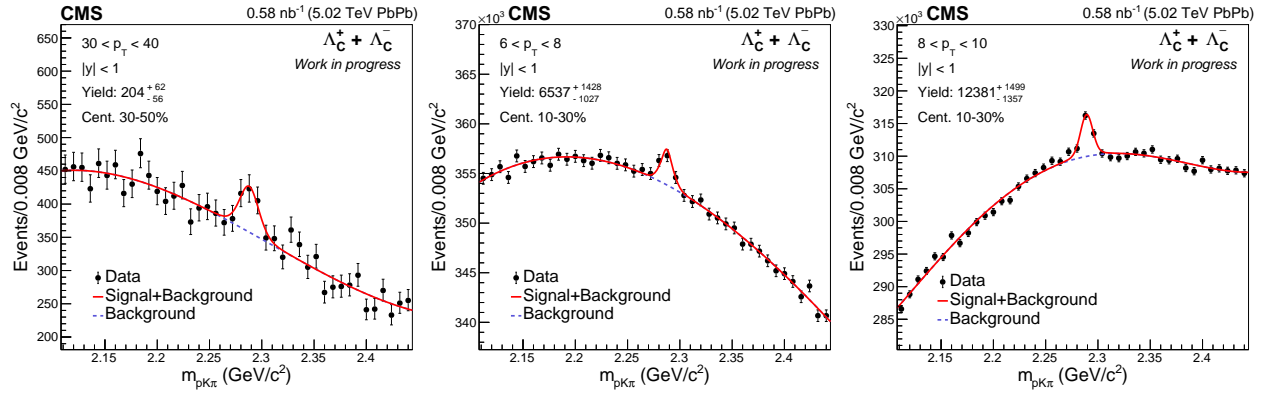
Figure 5.10. Invariant Mass Distribution Of Λ_c^+ Candidates With p_T= 30–40 GeV/c (Left) In Centrality Range 30–50%, 6–8 GeV/c (Middle) And 8–10 GeV/c In PbPb Collisions Within The Centrality Range 10–30%. The Solid Line Represents The Full Fit And The Dashed Line Represents The Background Component.

of these two p_T bins are estimated from the prompt ratios in the corresponding p_T bins in pp collisions.

$$\left.\frac{P}{NP}\right|_{\mathrm{PbPb}}^{withcut} = \left.\frac{P}{NP}\right|_{\mathrm{pp}}^{withcut} \frac{\alpha\epsilon(\mathrm{NP})_{\mathrm{pp}}}{\alpha\epsilon(\mathrm{P})_{\mathrm{pp}}} \Big/ \frac{R_{\mathrm{AA}}(\mathrm{P})_{D^0}}{R_{\mathrm{AA}}(\mathrm{NP})_{D^0}} \Big/ \frac{\Lambda_c^+/D^0(\mathrm{P})_{\mathrm{PbPb}}}{\Lambda_c^+/D^0(\mathrm{P})_{\mathrm{pp}}} \Big/ \frac{\alpha\epsilon(\mathrm{P})_{\mathrm{PbPb}}}{\alpha\epsilon(\mathrm{NP})_{\mathrm{PbPb}}} , \quad (5.1)$$
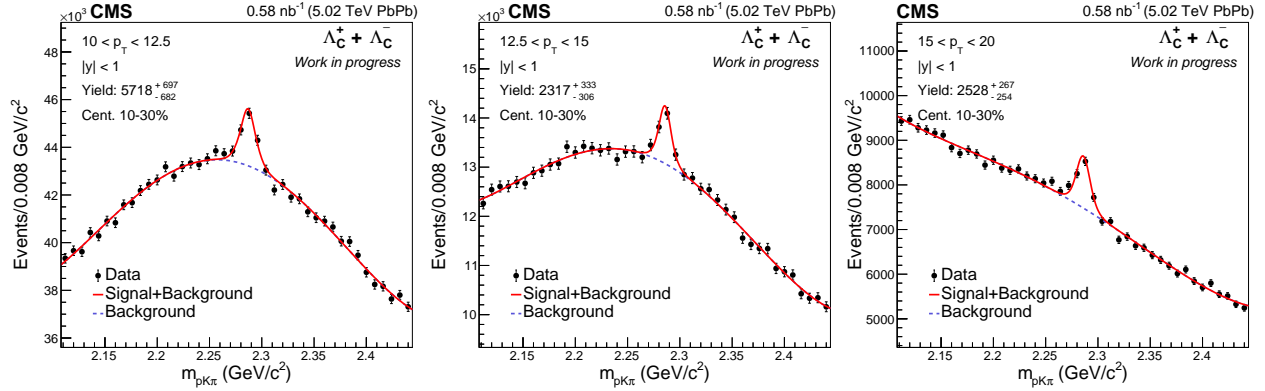
Figure 5.11. Invariant Mass Distribution Of Λ_c^+ Candidates With $p_T=$ 10–12.5 GeV/c (Left), 12.5–15 GeV/c (Middle) And 15–20 GeV/c In PbPb Collisions Within The Centrality Range 10–30%. The Solid Line Represents The Full Fit And The Dashed Line Represents The Background Component.
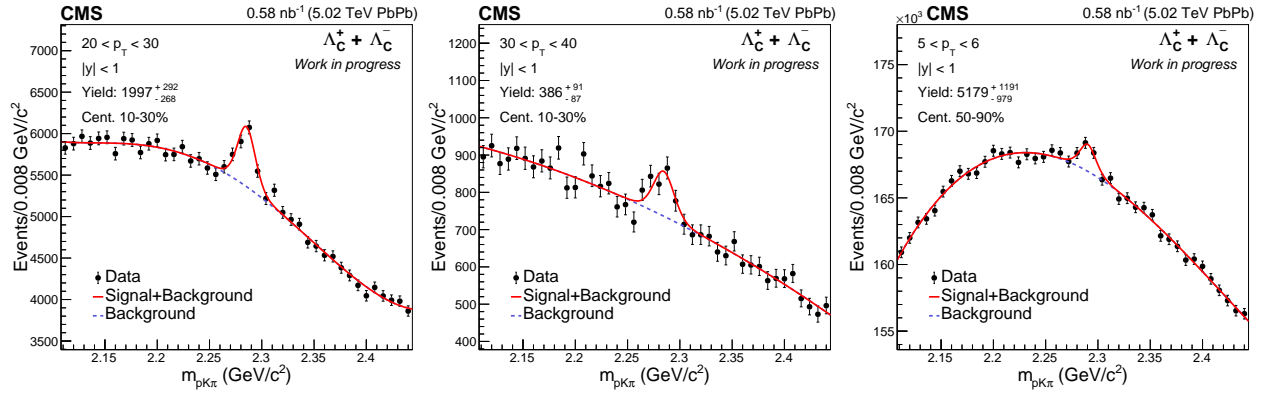
Figure 5.12. Invariant Mass Distribution Of Λ_c^+ Candidates With $p_T=$ 20–30 GeV/c (Left), 30–40 GeV/c (Middle) Within The Centrality Range 10–30% And 5–6 GeV/c In PbPb Collisions Within The Centrality Range 50–90%. The Solid Line Represents The Full Fit And The Dashed Line Represents The Background Component.

where, P represents prompt Λ_c^+ and NP represents nonprompt Λ_c^+. Previous CMS results have found more suppression for prompt than nonprompt D^0 mesons [41], [64], which can be quantified for 6–8 GeV/c (0–100% centrality) as $\frac{R_{AA}(P)_{D^0}}{R_{AA}(NP)_{D^0}} = 0.675 \pm 0.219$. This ratio for 10–12.5 GeV/c (0–10% centrality) can be quantified as 0.83 ± 0.10. The Λ_c^+/D^0 in both pp and PbPb is estimated from ALICE results [48], [49].
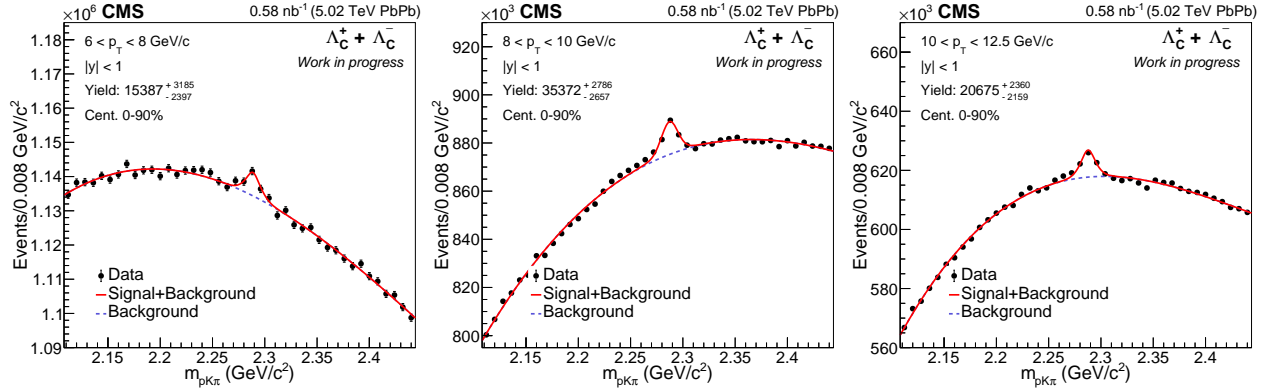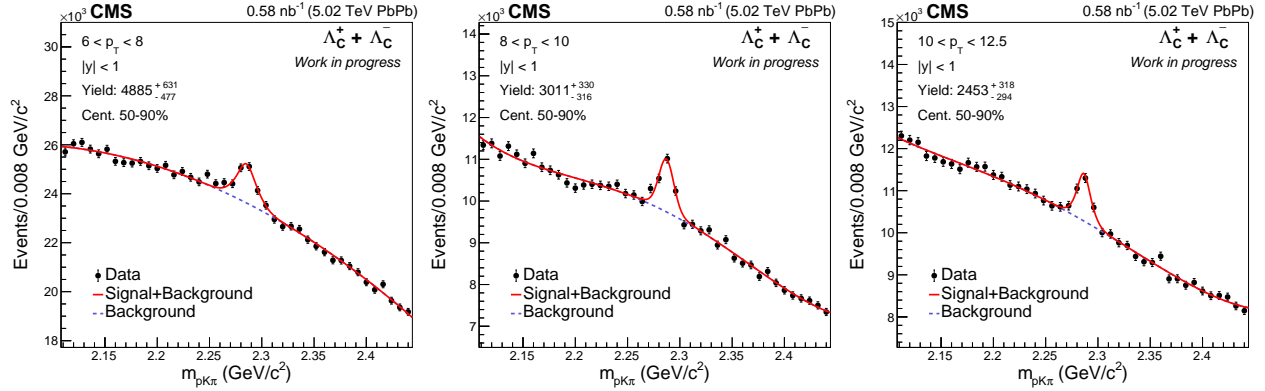
Figure 5.13. Invariant Mass Distribution Of Λ_c^+ Candidates With $p_T=$ 6–8 GeV/c (Left), 8–10 GeV/c (Middle) And 10–12.5 GeV/c In PbPb Collisions Within The Centrality Range 50–90%. The Solid Line Represents The Full Fit And The Dashed Line Represents The Background Component.
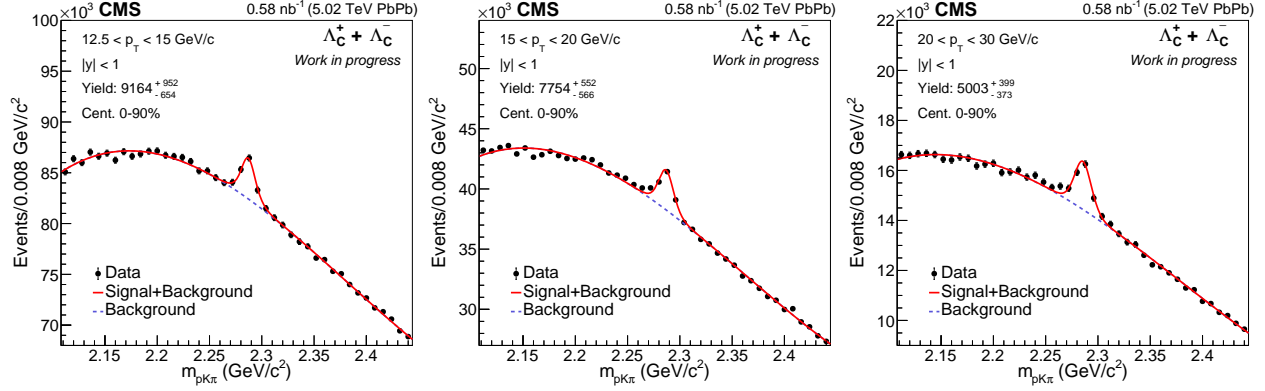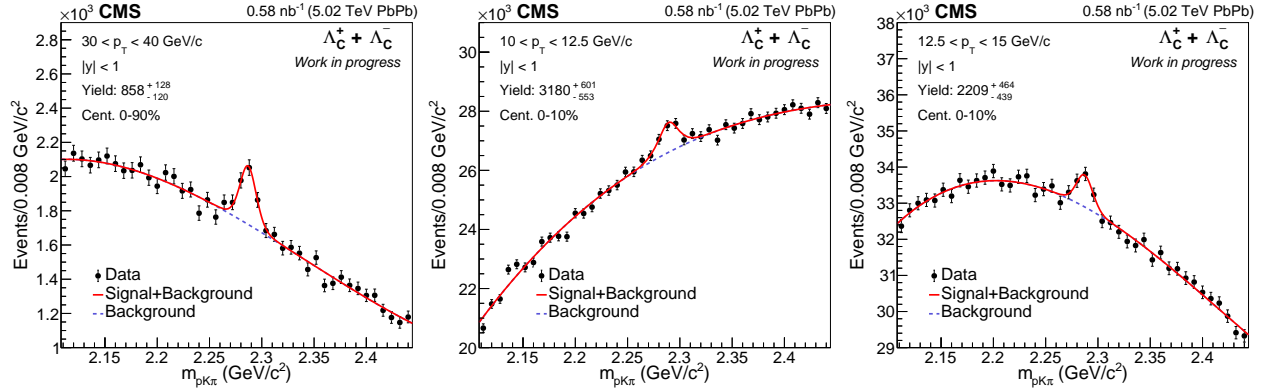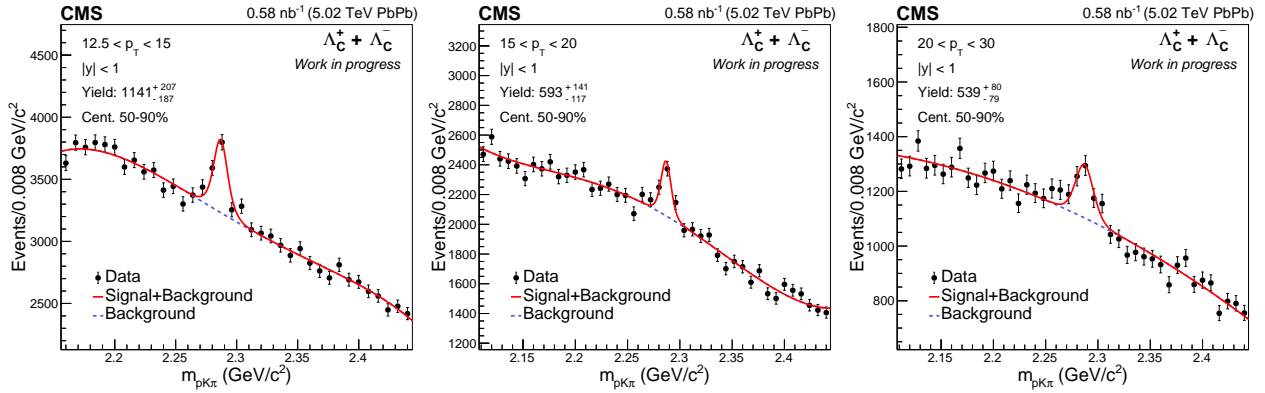

Figure 5.14. Invariant Mass Distribution Of Λ_c^+ Candidates With $p_T=$ 12.5–15 GeV/c (Left), 15–20 GeV/c (Middle) And 20–30 GeV/c In PbPb Collisions Within The Centrality Range 50–90%. The Solid Line Represents The Full Fit And The Dashed Line Represents The Background Component.

The uncertainty due to prompt ratio for these two p_T bins will be assigned as the quadratic sum of the uncertainty from R_{AA} ratio and pp prompt ratio. Thus the uncertainty due to prompt ratio is 34.9% for 6–8 GeV/c in centrality range 0–90%, and 24.5% for 10–12.5 GeV/c in centrality range 0–10%. The detailed information of the prompt ratio in PbPb collisions within five centrality classes are shown in Tab. 5.3 and 5.4.

Table 5.2. This Table Shows All The Fitted Prompt Ratio Got From The Best MC Resolution Scale Factor, The Systematic Uncertainty Due To DCA Fit And Also The Predicted Prompt Ratio From PYTHIA8 And FNOLL In pp Collisions For p_T Bins 3–4 GeV/c, 15–20 GeV/c And 20–30 GeV/c.

p_T intervals (GeV/c)	fitted prompt ratio	PYTHIA	FNOLL	uncertainty (%)
3–4	0.85	0.67	0.98	21.2
4–5	0.85	0.70	not needed	16.5
5–6	0.8	0.70	not needed	6.3
6–8	0.88	0.68	not needed	9.1
8–10	0.73	0.67	not needed	11.1
10–12.5	0.78	0.66	not needed	11.1
12.5–15	0.89	0.66	not needed	11.1
15–20	0.89	0.68	0.90	23.6
20–30	0.89	0.70	0.91	21.3

Table 5.3. This Table Shows All The Fitted Prompt Ratio Got From The Best MC Resolution Scale Factor And The Systematic Uncertainty Due To DCA Fit In PbPb Collisions In Centrality Class: 0–10% And 0–90%.

p_T intervals (GeV/c)	prompt ratio	systematic uncertainty on prompt ratio
centrality class: 0–90% in PbPb		
6–8	0.93	34.9%
8–10	0.9 ± 0.04	6.7%
10–12.5	0.8 ± 0.04	5%
12.5–15	0.9 ± 0.03	3.3%
15–20	0.86 ± 0.03	1.2%
20–30	0.9 ± 0.03	2.2%
30–40	0.89 ± 0.05	4.3%
centrality class: 0–10% in PbPb		
10–12.5	0.68	24.5%
12.5–15	0.91 ± 0.03	6.6%
15–20	0.96 ± 0.03	6.3%
20–30	0.94 ± 0.02	1.1%
30-40	0.90 ± 0.04	4.4%

Table 5.4. This Table Shows All The Fitted Prompt Ratio Got From The Best MC Resolution Scale Factor And The Systematic Uncertainty Due To DCA Fit In PbPb Collisions In Centrality Class: 10–30%, 30–50% And 50–90%.

p_T intervals (GeV/c)	Prompt ratio	Systematic uncertainty (%)
centrality class: 10–30% in PbPb		
6–8		
8–10	0.79 ± 0.05	3.8
10–12.5	0.92 ± 0.05	7.6
12.5–15	0.78 ± 0.09	13.3
15–20	0.82 ± 0.04	2.4
20–30	0.90 ± 0.04	1.1
30–40	0.93 ± 0.06	7.5
centrality class: 30–50% in PbPb		
6–8	0.99 ± 0.05	6.1
8–10	0.81 ± 0.05	6.2
10–12.5	0.92 ± 0.03	3.3
12.5–15	0.83 ± 0.07	9.6
15–20	0.91 ± 0.04	4.4
20–30	0.97 ± 0.05	3.1
30–40	0.90 ± 0.08	10.0
centrality class: 50–90% in PbPb		
5–6		
6–8	0.89 ± 0.04	11.0
8–10	0.86 ± 0.04	2.3
10–12.5	0.88 ± 0.04	2.3
12.5–15	0.92 ± 0.04	4.3
15–20	0.85 ± 0.06	10.6
20–30	0.88 ± 0.05	4.5
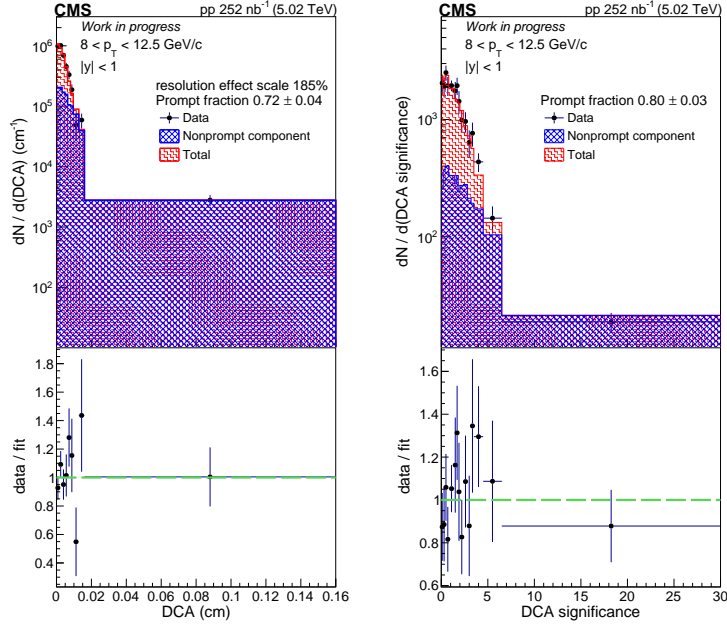
Figure 5.15. The Top Pannels Of Both Plots Show Prompt + Nonprompt Fit Of The Signal Λ_c^+ DCA Distribution Measured With The Invariant Mass Fit For p_T Range: 8–12.5 GeV/c In pp Collisions. The Left Plot Is With The Best MC Resolution Scale Factor In DCA Fit. The Right Plot Is From DCA Significance Fit Without Any Smearing, Which Is Used For Systematic Uncertainty Estimation. The Bottom Pannels Of Both Plots Show The Data/Fit Ratios.

5.4 Acceptance And Efficiency Correction

Acceptance and efficiency corrections are applied to the extracted Λ_c^+ yield in order to get the corrected spectra. In this section, the acceptance×efficiency as a function of transverse momentum p_T of Λ_c^+ is presented. The studies are performed with PYTHIA8 sample for pp and PYTHIA+HYDJET sample for PbPb.

The same strategy as that in 4.3 has been applied. Besides the p_T and centrality reweight, the PVz weight is also added to avoid the difference in PVz shape between MC and data. All weights are done for several times until the values of $\alpha\epsilon$ is converged. Figure 5.18 shows the
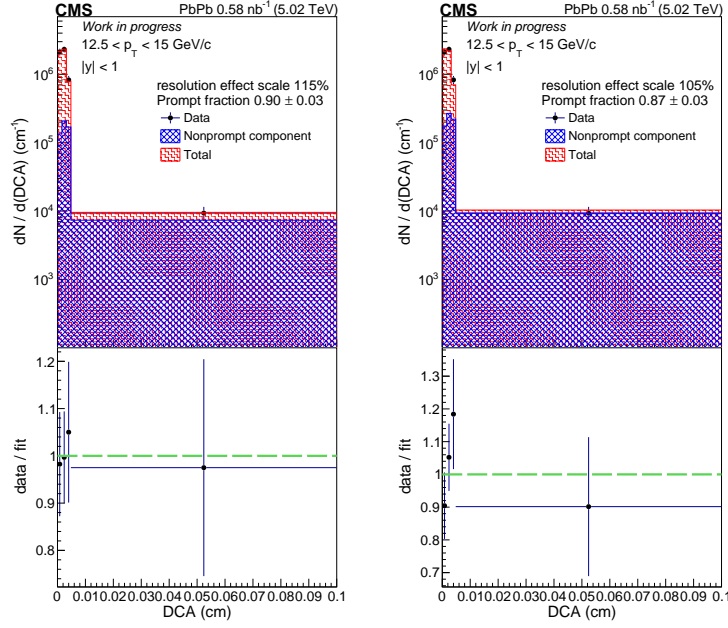
Figure 5.16. The Top Pannels Of Both Plots Show Prompt + Nonprompt Fit Of The Signal Λ_c^+ DCA Distribution Measured With The Invariant Mass Fit For p_T Range 12.5–15 GeV/c In PbPb Collisions In Centrality Class 0–90%. The Left Plot Is With Best MC Resolution Scale Factor. The Right Plot Is Used For Systematic Uncertainty Estimation. The Bottom Pannels Of Both Plots Show The Data/Fit Ratios.

acceptance times total efficiency as a function of p_T for both pp and PbPb collisions within five centrality classes.

5.5 Systematic Uncertainties

Systematic uncertainties arise from the extraction of the raw signal yield, the ability of the MC simulation to reproduce the combined acceptance and efficiency, the prompt ratio from DCA fit, the branching fraction of the decay mode, and the integrated luminosity. The detailed systematic uncertainties are described in detail as follows:

The systematic uncertainty in the signal yields is obtained by varying the modeling functions that are used for the signal and background contributions and also the fit range.
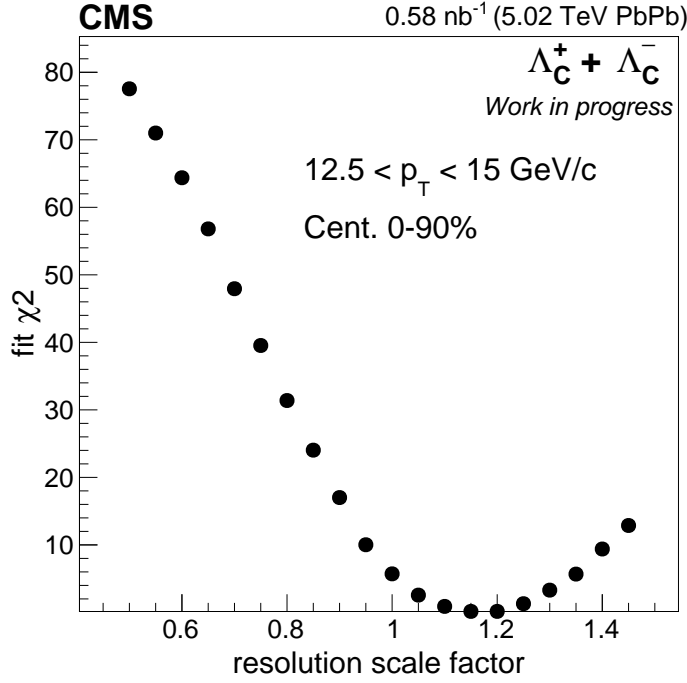
Figure 5.17. $\chi 2$ Of Λ_c^+ DCA Fit Vs. MC Resolution Scale Factor For 12.5–15 GeV/c In Centrality Class 0–90% In PbPb Collisions.

The background function is changed from the default order to default order +1 Chebyshev polynomials, with the difference in yields between alternative function and default fit function taken as the systematic uncertainty on background fit function. When the effect of changing the background fit function is considered, the signal shape is fixed according to the default fit function to avoid the signal shape changing effect. The systematic uncertainty for the signal PDF has been estimated by changing from the default signal fit function to an alternative signal fit function, for both pp and PbPb collisions. The alternative signal fit function is triple Gaussians, and double Gaussians for pp and PbPb collisions, respectively. The difference in signal yields between alternative signal fit function and the default one is taken as the systematic uncertainty on signal fit function. The systematic uncertainty for the fit range has been estimated by changing the fit range from the default range to alternative fit ranges, for both pp and PbPb collisions. The biggest difference in the signal yields between nominal and alternative fit range is taken as the systematic uncertainty on the fit range.

80
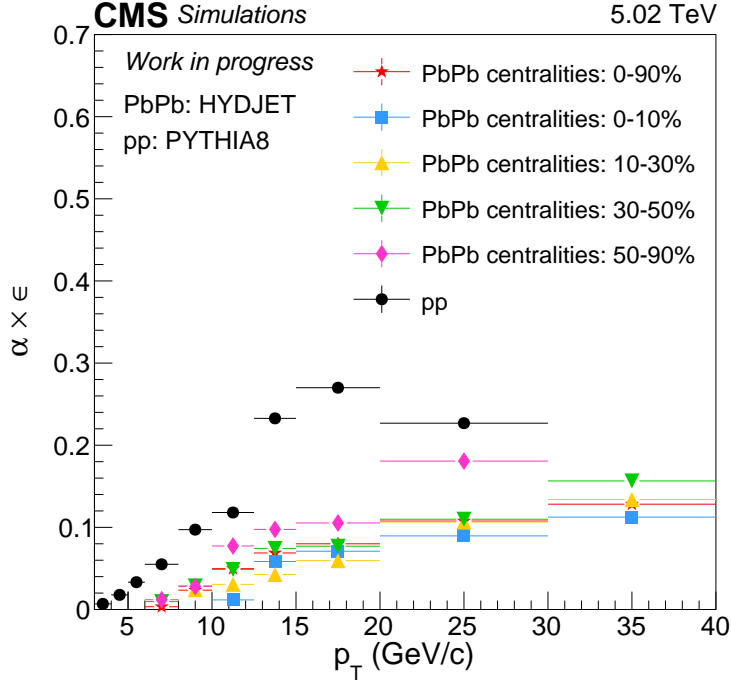
Figure 5.18. Acceptance Times Total Efficiency As A Function Of p_T For The pp And PbPb Analysis For Prompt Λ_c^+. The Black Spots Correspond To The Acceptance Times Total Efficiency For pp collisions. The Red Stars, Blue Boxes, Yellow Triangles, Green Triangles And Pink Markers Correspond To 0–90%, 0–10%, 10–30%, 30–50% and 50–90% In PbPb Collisions, Respectively.

Five sources of systematic uncertainties associated with the MC modeling of the data are evaluated. The first uncertainty measures the effect of the selection criteria variation, the same method is applied as in section 4.4. For each selection criteria (BDTG value or topological selection criteria), the double ratio is evaluated at many different values of the selection criterion. 6–10 GeV/c in PbPb collisions in 0–90% centrality class could not do the double ratio scan due to the small $s/\sqrt{b}$, the uncertainties for these two p_T bins are achieved by adding the systematic uncertainty for decay length significance and vertex probability in 10–12.5 GeV/c (0–90% centrality) and that of pointing angle α in 8–10 GeV/c in quadrature.

The second uncertainty arises from a potential mismodeling of the p_T distribution of Λ_c^+ baryons because $\alpha\epsilon$ is strongly dependent on the Λ_c^+ p_T. For both pp and PbPb collisions, the default p_T shape is derived from the data and the alternative p_T spectra is from PYTHIA8

with color reconnection (described in section 4.5). The deviation in $\alpha\epsilon$ is taken as the systematic uncertainty.

The third uncertainty arises from imprecise knowledge of the resonant substructure of the $pK^- \pi^+$ decay mode [2]. The procedure is described in section 4.4.

The fourth uncertainty associated with the MC modeling of the data is the track reconstruction efficiency, which is the same as that in section 4.4.

The fifth uncertainty arises form the prompt ratio that is got from DCA fit. This is explained in section 5.3.

The overall $\Lambda_c^+ \to pK^- \pi^+$ branching fraction uncertainty is 5.3% [2]. The uncertainties in the integrated luminosity in pp collisions and the MB selection efficiency in PbPb collisions are 1.9% [73] and 1.5% [68], respectively.

For the measurement of the p_T spectra, the uncertainties associated with the $\Lambda_c^+ \to pK^-$ π^+ branching fraction, tracking efficiency, the luminosity and MB selection efficiency are labeled as global uncertainties. Adding these contributions in quadrature yields global uncertainty of 6.8 and 7.4% for pp and PbPb collisions, respectively. In measuring the nuclear modification factor R_{AA}, the uncertainties associated with the branching fraction and sub-resonant contributions cancel and the prompt fraction uncertainty (for 6–8 GeV/c in 0–90% centrality class and 10–12.5 GeV/c in 0–10% centrality class) partially cancels. In calculating the Λ_c^+/D^0 production ratio, the uncertainties associated with D^0 from the yield extraction, selection criteria efficiency, and p_T shape are obtained from Ref. [41], while the uncertainties in the integrated luminosity in pp collisions and the MB selection efficiency in PbPb collisions cancel. Table 5.5-5.18 are the summary tables for relative systematic uncertainties for each measurements for prompt Λ_c^+.

5.6 Results

This section presents the p_T spectrum in both pp and PbPb (5 centrality ranges), R_{AA}, the Λ_c^+/D^0 production ratio in both pp and PbPb collisions.

Table 5.5. Summary Of Relative Systematic Uncertainties For Prompt Λ_c^+ Cross Section In pp Collisions At 5.02 TeV With CMS 2017 Data.

source	p_T interval (GeV/c)								
	3-4	4-5	5-6	6-8	8-10	10-12.5	12.5-15	15-20	20-30
Inv. mass fit (Background)	6.9%	5.8%	1.4%	0.0%	5.4%	5.7%	1.0%	4.8%	0.7%
Inv. mass fit(Signal)	0.2%	0.1%	0.3%	5.9%	1.1%	6.4%	1.2%	0.6%	2.9%
Inv. mass fit range	11.6%	21.7%	4.2%	5.8%	7.8%	6.9%	2.3%	3.3%	8.3%
Tracking efficiency	12%								
Selection efficiency	8.7%	8.7%	8.7%	13.6%	1.1%	3.5%	7.0%	8.2%	8.6%
MC p_T shape	4.5%	0.8%	0.3%	0.6%	0.3%	0.4%	0.1%	0.5%	3.1%
$\alpha\epsilon_{reco}$	8.6%	8.27%	8.25%	8.43%	8.23%	8.27%	8.18%	8.07%	8.20%
prompt fraction	21.2%	16.5%	6.3%	9.1%	11.1%	11.1%	11.1%	23.6%	21.3%
Luminosity	1.9%								
Branching ratio	5.3%								
Total systematic uncertainty	31.3%	33.1%	19.5%	24.2%	21.4%	22.4%	20.6%	30.0%	29.3%

Table 5.6. Summary Of Relative Systematic Uncertainties For Prompt Λ_c^+ Differential Yield In PbPb Collisions At 5.02 TeV For Centrality 0–90% With CMS 2018 Data.

source	p_T interval (GeV/c)						
	6–8	8–10	10–12.5	12.5–15	15–20	20–30	30–40
Inv. mass fit(Background)	0.9%	7.5%	5.4%	0.8%	6.9%	7.7%	3.8%
Inv. mass fit(Signal)	4.8%	6.8%	4.1%	1.3%	0.9%	2.3%	0.2%
Inv. mass fit range	42.8%	23.2%	2.9%	1.3%	16.2%	19.3%	7.8%
Tracking efficiency	15%						
Selection efficiency	36.2%	22.1%	6.5%	13.7%	4.6%	10.7%	20.2%
MC p_T shape	1.1%	0.4%	0.8%	0.3%	0.6%	1.4%	1.1%
$\alpha\epsilon_{reco}$	8.2%	8.2%	8.3%	8.2%	8.2%	8.0%	8.0%
prompt fraction	34.9%	6.7%	5%	3.3%	1.2%	2.2%	4.3%
Number of events	1.5%						
Branching ratio	5.3%						
Total uncertainty	68.6%	38.7%	21.1%	22.9%	25.6%	29.6%	28.7%

Table 5.7. Summary Of Relative Systematic Uncertainties For Prompt Λ_c^+ Differential Yield In PbPb Collisions At 5.02 TeV For Centrality 0–10% With CMS 2018 Data.

source	p_T interval (GeV/c)				
	10–12.5	12.5–15	15–20	20–30	30–40
Inv. mass fit(Background)	5.1%	10.3%	4.9%	5.9%	2.7%
Inv. mass fit(Signal)	2.9%	3.9%	4.8%	0.3%	1.4%
Inv. mass fit range	8.9%	24.5%	12.0%	11.8%	8.2%
Tracking efficiency	15%				
Selection efficiency	6.5%	13.7%	4.6%	10.7%	20.2%
MC p_T shape	0.02%	0.3%	1.2%	1.5%	0.3%
$\alpha\epsilon_{reco}$	8.6%	8.3%	8.2%	8.1%	8.3%
prompt fraction	24.5%	6.6%	6.3%	1.1%	4.4%
Number of events	1.5%				
Branching ratio	5.3%				
Total Uncertainty	32.9%	35.7%	24.0%	24.8%	28.8%

Table 5.8. Summary Of Relative Systematic Uncertainties For Prompt Λ_c^+ Differential Yield In PbPb Collisions At 5.02 TeV For Centrality 10–30% With CMS 2018 Data.

source	p_T interval (GeV/c)					
	8–10	10–12.5	12.5–15	15–20	20–30	30–40
Inv. mass fit(Background)	1.9%	1.9%	0.3%	7.2%	11.0%	0.3%
Inv. mass fit(Signal)	1.2%	1.4%	0.4%	0.6%	0.6%	0.3%
Inv. mass fit range	11.7%	20.8%	12.3%	11.2%	6.4%	16.1%
Tracking efficiency	15%					
Selection efficiency	22.1%	6.5%	13.7%	4.6%	10.7%	20.2%
MC p_T shape	0.3%	0.7%	0.2%	0.03%	2.0%	1.6%
$\alpha\epsilon_{reco}$	8.2%	8.7%	8.7%	8.5%	8.0%	8.2%
prompt fraction	3.8%	7.6%	13.3%	2.4%	1.1%	7.5%
Number of events	1.5%					
Branching ratio	5.3%					
Total uncertainty	31.1%	29.5%	29.1%	23.1%	24.5%	32.4%

Table 5.9. Summary Of Relative Systematic Uncertainties For Prompt Λ_c^+ Differential Yield In PbPb Collisions At 5.02 TeV For Centrality 30–50% With CMS 2018 Data.

source	p_T interval (GeV/c)						
	6–8	8–10	10–12.5	12.5–15	15–20	20–30	30–40
Inv. mass fit(Background)	2.2%	7.8%	7.4%	11.4%	8.3%	0.3%	5.4%
Inv. mass fit(Signal)	6.1%	0.7%	1.6%	2.2%	0.2%	0.6%	0.5%
Inv. mass fit range	9.1%	5.4%	4.8%	11.9%	4.2%	4.3%	10.3%
Tracking efficiency	15%						
Selection efficiency	36.2%	22.1%	6.5%	13.7%	4.6%	10.7%	20.2%
MC p_T shape	0.9%	0.4%	0.8%	0.4%	0.5%	0.5%	1.1%
$\alpha\epsilon_{reco}$	7.9%	8.6%	8.3%	8.3%	8.3%	8.4%	8.3%
prompt fraction	6.1%	6.2%	3.3%	9.6%	4.4%	3.1%	10.0%
Number of events	1.5%						
Branching ratio	5.3%						
Total uncertainty	42.3%	30.8%	21.4%	29.7%	21.2%	21.7%	31.1%

Table 5.10. Summary Of Relative Systematic Uncertainties For Prompt Λ_c^+ Differential Yield In PbPb Collisions At 5.02 TeV For Centrality 50–90% With CMS 2018 Data.

2*source	p_T interval (GeV/c)					
	6–8	8–10	10–12.5	12.5–15	15–20	20–30
Inv. mass fit(Background)	0.4%	0.8%	6.4%	6.8%	11.0%	0.5%
Inv. mass fit(Signal)	4.4%	0.7%	0.9%	2.1%	2.4%	3.7%
Inv. mass fit range	12.8%	18.1%	4.6%	11.5%	13.0%	5.7%
Tracking efficiency	15%					
Selection efficiency	36.2%	22.1%	6.5%	13.7%	4.6%	10.7%
MC p_T shape	0.9%	0.7%	0.7%	0.3%	0.3%	0.3%
$\alpha\epsilon_{reco}$	8.2%	8.1%	8.2%	8.2%	8.2%	8.0%
prompt fraction	11.0%	2.3%	2.3%	4.3%	10.6%	4.5%
Number of events	1.5%					
Branching ratio	5.3%					
Total uncertainty	44.0%	33.8%	20.8%	26.7%	27.4%	22.4%

Table 5.11. Summary Of Relative Systematic Uncertainties For Prompt Λ_c^+ R_{AA} In Centrality Class: 0–90% With CMS 2017/2018 Data.

source	p_T interval (GeV/c)					
	6–8	8–10	10–12.5	12.5–15	15–20	20–30
Inv. mass fit (pp)	8.3%	9.6%	11.0%	2.8%	5.9%	8.8%
Inv. mass fit(PbPb)	43.0%	25.3%	7.4%	2.0%	17.6%	20.9%
Tracking efficiency	19%					
Selection efficiency(pp)	13.6%	1.1%	13.5%	7.0%	8.2%	8.6%
Selection efficiency(PbPb)	10.9%	10.9%	6.5%	13.7%	4.6%	20.2%
MC p_T shape (pp)	0.6%	0.3%	0.4%	0.1%	0.5%	3.1%
MC p_T shape (PbPb)	1.1%	0.4%	0.8%	0.3%	0.6%	1.4%
prompt fraction	32.4%	12.9%	12.2%	11.6%	23.6%	21.4%
Luminosity (pp)	1.9%					
Number of events (PbPb)	1.5%					
Total uncertainty	60.3%	37.2%	30.3%	27.4%	36.8%	42.8%

Table 5.12. Summary Of Relative Systematic Uncertainties For Prompt Λ_c^+ R_{AA} In Centrality Class: 0–10% With CMS 2017/2018 Data.

source	p_T intervals (GeV/c)			
	10–12.5	12.5–15	15–20	20–30
Inv. mass fit (pp)	11.0%	2.8%	5.9%	8.8%
Inv. mass fit(PbPb)	10.7%	26.9%	13.8%	13.2%
Tracking efficiency	19%			
Selection efficiency(pp)	13.5%	7.0%	8.2%	8.6%
Selection efficiency(PbPb)	6.5%	13.7%	4.6%	20.2%
MC p_T shape (pp)	0.4%	0.1%	0.5%	3.1%
MC p_T shape (PbPb)	0.02%	0.3%	1.2%	1.5%
prompt fraction	10.0%	12.9%	24.4%	21.3%
Luminosity (pp)	1.9%			
Number of events (PbPb)	1.5%			
Total uncertainty	30.4%	38.7%	35.7%	39.6%

86

Table 5.13. Summary Of Relative Systematic Uncertainties For Prompt Λ_c^+ R_{AA} In Centrality Class: 10–30% With CMS 2017/2018 Data.

source	p_T interval (GeV/c)				
	8–10	10–12.5	12.5–15	15–20	20–30
Inv. mass fit (pp)	9.6%	11.0%	2.8%	5.9%	8.8%
Inv. mass fit (PbPb)	12.0%	20.9%	12.3%	13.4%	12.7%
Tracking efficiency	19%				
Selection efficiency (pp)	1.1%	13.5%	7.0%	8.2%	8.6%
Selection efficiency (PbPb)	10.9%	6.5%	13.7%	4.6%	20.2%
MC p_T shape (pp)	0.3%	0.4%	0.1%	0.5%	3.1%
MC p_T shape (PbPb)	0.3%	0.7%	0.2%	0.03%	2.0%
prompt fraction	11.7%	13.5%	17.3%	23.7%	21.3%
Luminosity (pp)	1.9%				
Number of events (PbPb)	1.5%				
Total uncertainty	29.3%	36.5%	32.6%	35.1%	39.4%

Table 5.14. Summary Of Relative Systematic Uncertainties For Prompt Λ_c^+ R_{AA} In Centrality Class: 30–50% With CMS 2017/2018 Data.

source	p_T interval (GeV/c)					
	6–8	8–10	10–12.5	12.5–15	15–20	20–30
Inv. mass fit (pp)	8.3%	9.6%	11.0%	2.8%	5.9%	8.8%
Inv. mass fit (PbPb)	11.2%	9.5%	9.0%	16.6%	9.3%	4.4%
Tracking efficiency	19%					
Selection efficiency (pp)	13.6%	1.1%	13.5%	7.0%	8.2%	8.6%
Selection efficiency (PbPb)	10.9%	10.9%	6.5%	13.7%	4.6%	20.2%
MC p_T shape (pp)	0.6%	0.3%	0.4%	0.1%	0.5%	3.1%
MC p_T shape (PbPb)	0.9%	0.4%	0.8%	0.4%	0.5%	1.1%
prompt fraction	11.0%	12.7%	11.6%	14.7%	24.0%	21.5%
Luminosity (pp)	1.9%					
Number of events (PbPb)	1.5%					
Total uncertainty	31.4%	28.8%	30.5%	33.2%	34.0%	37.7%

Table 5.15. Summary Of Relative Systematic Uncertainties For Prompt $\Lambda_{\rm c}^+$ $R_{\rm AA}$ In Centrality Class: 50–90% With CMS 2017/2018 Data.

source	p_T interval (GeV/c)					
	6–8	8–10	10–12.5	12.5–15	15–20	20–30
Inv. mass fit (pp)	8.3%	9.6%	11.0%	2.8%	5.9%	8.8%
Inv. mass fit (PbPb)	13.5%	18.2%	7.9%	13.5%	17.2%	6.8%
Tracking efficiency	19%					
Selection efficiency (pp)	13.6%	1.1%	13.5%	7.0%	8.2%	8.6%
Selection efficiency (PbPb)	10.9%	10.9%	6.5%	13.7%	4.6%	20.2%
MC p_T shape (pp)	0.6%	0.3%	0.4%	0.1%	0.5%	3.1%
MC p_T shape (PbPb)	0.9%	0.7%	0.7%	0.3%	0.3%	0.3%
prompt fraction	14.3%	11.3%	11.3%	11.9%	25.9%	21.8%
Luminosity (pp)	1.9%					
Number of events (PbPb)	1.5%					
Total uncertainty	33.6%	32.2%	30.1%	30.6%	38.1%	38.2%

Table 5.16. Summary Of Relative Systematic Uncertainties For Prompt $\Lambda_{\rm c}^+/D^0$ In pp Collisions At 5.02 TeV.

source	p_T interval (GeV/c)								
	3-4	4-5	5-6	6-8	8-10	10-12.5	12.5-15	15-20	20-30
Inv. mass fit ($\Lambda_{\rm c}^+$)	20.2%	14.5%	12.5%	8.1%	5.8%	9.3%	29.8%	13.9%	6.8%
Inv. mass fit(D^0)	7.6%	3.5%	3.0%	3.0%	1.7%	2.1%	2.1%	4.0%	2.0%
Tracking efficiency	4%								
Selection efficiency(D^0)	3.6%								0.5%
Selection efficiency($\Lambda_{\rm c}^+$)	23.8%	19.0%	27.0%	24.5%	0.3%	13.5%	28.7%	28.7%	8.6%
MC p_T shape ($\Lambda_{\rm c}^+$)	4.5%	0.8%	0.3%	0.6%	0.3%	0.4%	0.1%	0.5%	3.1%
MC p_T shape (D^0)	3.0%	2.0%	2.0%	1.0%	1.0%	1.0%	0.0%	0.0%	0.0%
prompt fraction ($\Lambda_{\rm c}^+$)	21.2%	16.5%	11.3%	6.8%	9.6%	20.5%	11.1%	23.6%	21.3%
prompt fraction (D^0)	10%								
Branching ratio ($\Lambda_{\rm c}^+$)	5.3%								
Branching ratio (D^0)	1.3%								
$\alpha\epsilon_{reco}$ ($\Lambda_{\rm c}^+$)	8.6%	8.27%	8.25%	8.43%	8.23%	8.27%	8.18%	8.07%	8.20%
Total uncertainty	41.8%	33.0%	35.4%	30.9%	18.9%	30.4%	45.4%	42.6%	28.3%

Table 5.17. Summary Of Relative Systematic Uncertainties For Prompt Λ_c^+/D^0 In PbPb Collisions In Centrality Class 0–90%.

source	p_T interval (GeV/c)						
	6–8	8–10	10–12.5	12.5–15	15–20	20–30	30–40
Inv. mass fit (Λ_c^+)	11.4%	18.5%	29.9%	5.4%	12.8%	18.9%	5.8%
Inv. mass fit(D^0)	1.7%	1.7%	1.3%	1.3%	6.5%	9.4%	7.5%
Tracking efficiency	5%						
Selection efficiency(D^0)	3.5%					2.7%	
Selection efficiency(Λ_c^+)	36.2%	22.1%	6.5%	13.7%	4.6%	20.2%	10.7%
MC p_T shape (Λ_c^+)	1.1%	0.4%	0.8%	0.3%	0.6%	1.4%	1.1%
MC p_T shape (D^0)	1.0%	1.0%	1.0%	0.0%	0.0%	0.0%	0.0%
prompt fraction (Λ_c^+)	34.9%	6.7%	5%	3.3%	1.2%	2.2%	4.3%
prompt fraction (D^0)	10%						
Branching ratio (Λ_c^+)	5.3%						
Branching ratio (D^0)	1.3%						
$\alpha\epsilon_{reco}$ (Λ_c^+)	8.2%	8.2%	8.3%	8.2%	8.2%	8.0%	8.0%
Total uncertainty	53.8%	33.4%	34.6%	21.5%	21.5%	33.0%	21.2%

Table 5.18. Summary Of Relative Systematic Uncertainties For Prompt Λ_c^+/D^0 In PbPb Collisions In Centrality Class 0–10%.

source	p_T interval (GeV/c)				
	10–12.5	12.5–15	15–20	20–30	30–40
Inv. mass fit (Λ_c^+)	7.2%	25.3%	6.9%	9.8%	15.8%
Inv. mass fit(D^0)	3.4%	3.4%	12.0%	12%	12.7%
Tracking efficiency	5%				
Selection efficiency(D^0)	8.1%			2.7%	
Selection efficiency(Λ_c^+)	6.5%	13.7%	4.6%	10.7%	20.2%
MC p_T shape (Λ_c^+)	0.02%	0.3%	1.2%	1.5%	0.3%
MC p_T shape (D^0)	1.0%	0.0%	0.0%	0.0%	0.0%
prompt fraction (Λ_c^+)	24.5%	6.6%	6.3%	1.1%	4.4%
prompt fraction (D^0)	10%				
Branching ratio (Λ_c^+)	5.3%				
Branching ratio (D^0)	1.3%				
$\alpha\epsilon_{reco}$ (Λ_c^+)	8.6%	8.3%	8.2%	8.1%	8.3%
Total uncertainty	31.6%	34.2%	23.3%	24.2%	32.7%

The p_T-differential cross section for prompt Λ_c^+ in pp collisions is defined as:

$$\left. \frac{d\sigma_{\rm pp}^{\Lambda_c^+}}{dp_T} \right|_{|y|<1} = \frac{f_{\rm prompt}}{2\mathcal{L}\Delta p_T \mathcal{B}} \frac{N_{\rm pp}^{\Lambda_c^+}|_{|y|<1}}{\alpha\epsilon} \, , \tag{5.2}$$

where $N_{\rm pp}^{\Lambda_c^+}|_{|y|<1}$ are the Λ_c^+ yields extracted in each p_T interval, $\mathcal{L}$ (252/nb for Zero Bias) is the luminosity, Δp_T is the width of the p_T interval, $f_{\rm prompt}$ is the prompt ratio of Λ_c^+, $\mathcal{B}$ is the branching ratio of the decay channel that is used in this analysis, $\alpha\epsilon$ represents the acceptance $\times$ efficiency correction. The factor $1/2$ accounts for the fact that the yield were measured for particles and antiparticles, but the cross section is given for particles only.

The cross section for prompt Λ_c^+ PbPb are presented as the followings:

$$\left. \frac{1}{\langle T_{\rm AA}\rangle} \frac{dN_{\rm PbPb}^{\Lambda_c^+}}{dp_T} \right|_{|y|<1} = \frac{f_{\rm prompt}}{\langle T_{\rm AA}\rangle} \frac{1}{2N_{\rm events}\Delta p_T \mathcal{B}} \frac{N_{\rm PbPb}^{\Lambda_c^+}|_{|y|<1}}{\alpha\epsilon} \, , \tag{5.3}$$

where $N_{\rm events}$ are the number of MB events (centrality class 0–90% has 3,395,373,402 events corrected by the event filter), $\langle T_{\rm AA}\rangle = \langle N_{\rm coll}\rangle/\sigma_{\rm pp\text{-}inelastic}$ is the nuclear overlap function, which is equal to the value of $N_{\rm coll}$ divided by the pp cross section. Other parameters are the same as those in pp collisions.
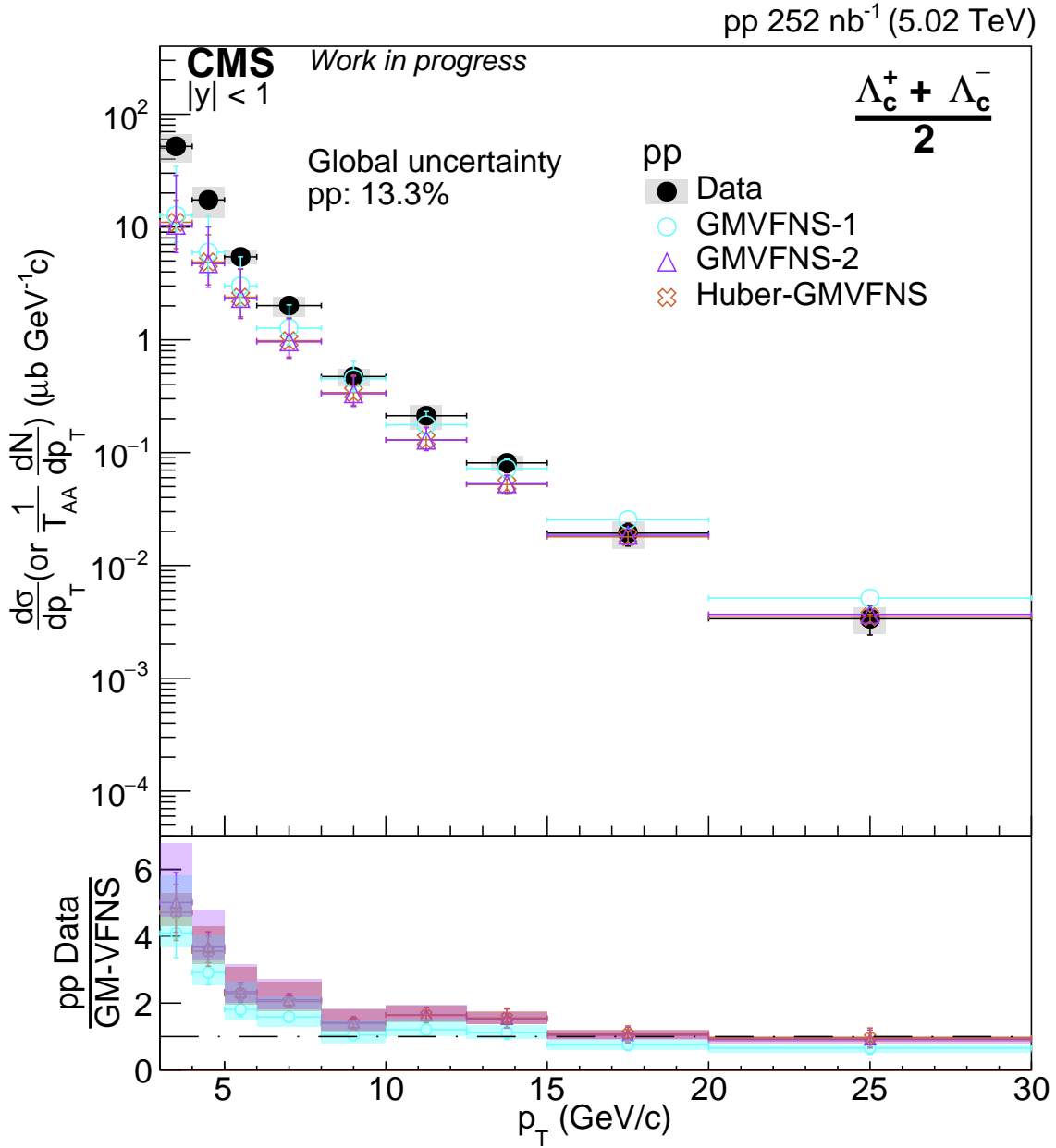
Figure 5.19 and 5.20 show the p_T-differential cross section of prompt Λ_c^+ baryon production in pp collisions for the range of $3 < p_T < 30$ GeV/c and the $T_{\rm AA}$-scaled yields in PbPb collisions in five centrality classes. The 13.3% (16.0%) normalization uncertainty for the pp (PbPb) results is not included in the boxes representing the systematic uncertainties for each data point.

$R_{\rm AA}$ of prompt Λ_c^+ is defined as the followings:

$$R_{\rm AA}(p_T) = \frac{1}{\langle T_{\rm AA}\rangle} \frac{dN_{\rm PbPb}^{\Lambda_c^+}}{dp_T} \left/ \frac{d\sigma_{\rm pp}^{\Lambda_c^+}}{dp_T} \right. . \tag{5.4}$$

The nuclear modification factor $R_{\rm AA}$ for prompt Λ_c^+ baryons in five centrality classes is shown in Fig. 5.21 as a function of p_T. The results show that Λ_c^+ is suppressed in PbPb collisions in 0–90% and 0–10% centrality classes compared to peripheral collisions.

Figure 5.22 shows the Λ_c^+/D^0 production ratio as a function of p_T for pp collisions and PbPb collisions in the centrality range 0–90 and 0–10%. Figure. 5.22 shows that calculations using a color reconnection model is consistent with our results for the Λ_c^+/D^0 production ratio in pp collisions within uncertainty. There is a hint of an enhancement in the Λ_c^+/D^0 production ratio in PbPb collisions in the p_T range of 6–10 GeV/c compared to pp data, but due to the large systematic uncertainty, no solid conclusion can be drawn. The PbPb measurement in the p_T range 12.5–30 GeV/c is consistent with the pp result. This lack of an enhancement may suggest that there is no significant contribution from the coalescence process for $p_T > 12.5$ GeV/c in PbPb collisions.
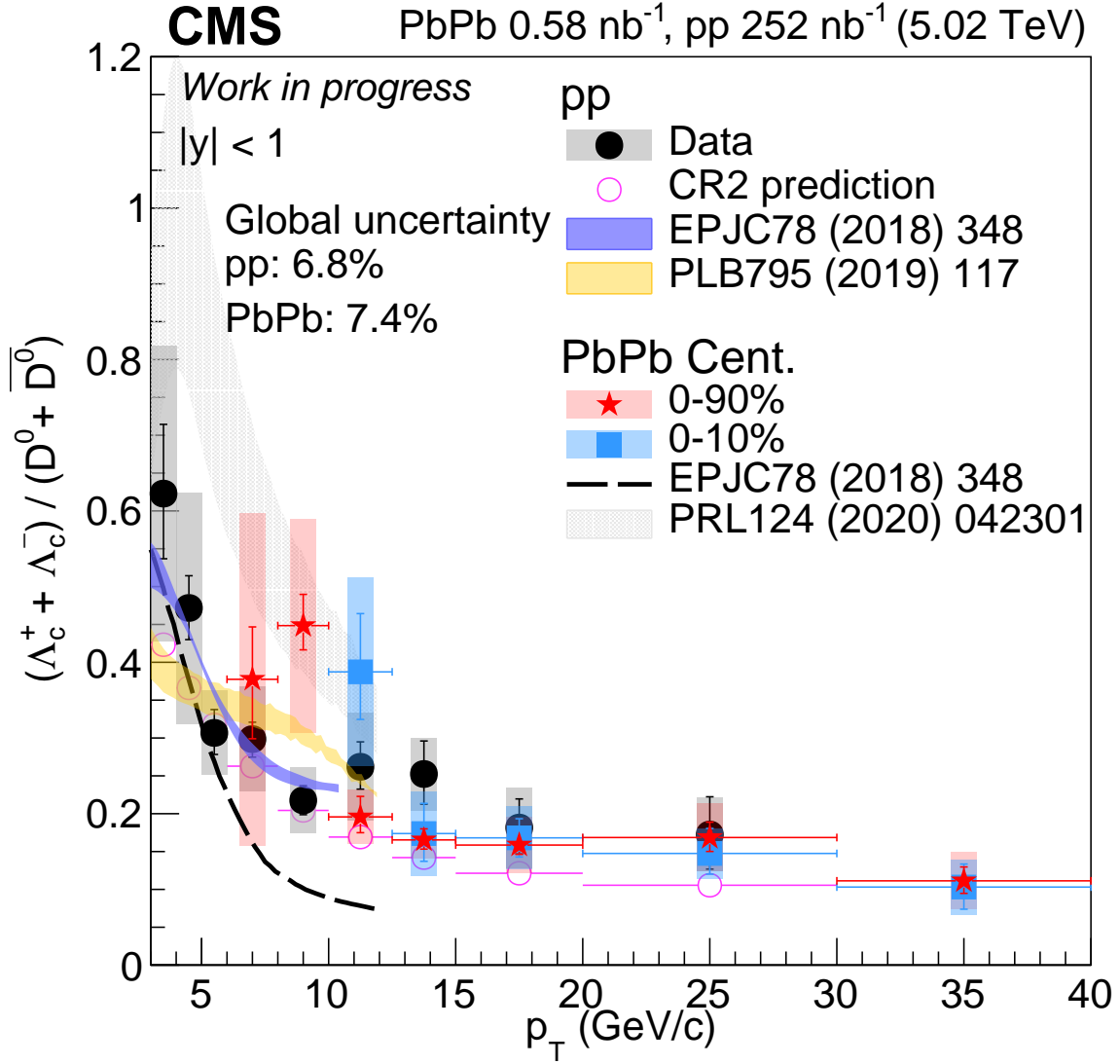
Figure 5.19. The p_T-differential Cross Sections For Prompt Λ_c^+ Production In pp Collisions. The Boxes And Error Bars Represent The Systematic And Statistical Uncertainties, Respectively. The Bottom Panel Shows Data/Predictions Ratios.
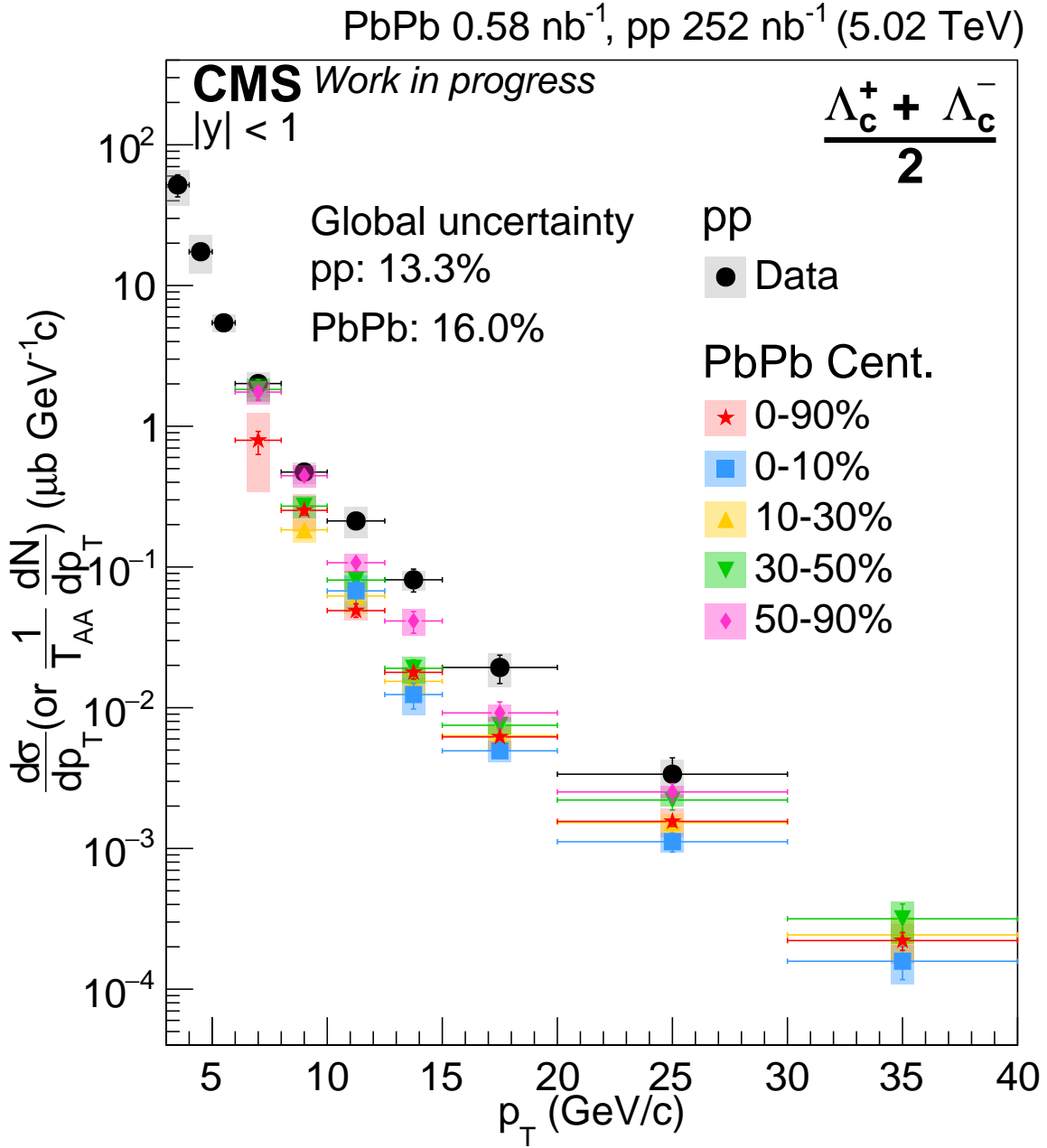
Figure 5.20. The p_T-differential Cross Sections For Prompt Λ_c^+ Production In pp Collisions And The T_{AA}-scaled Yields For Five Centrality Regions Of PbPb Collisions. The Boxes And Error Bars Represent The Systematic And Statistical Uncertainties, Respectively.
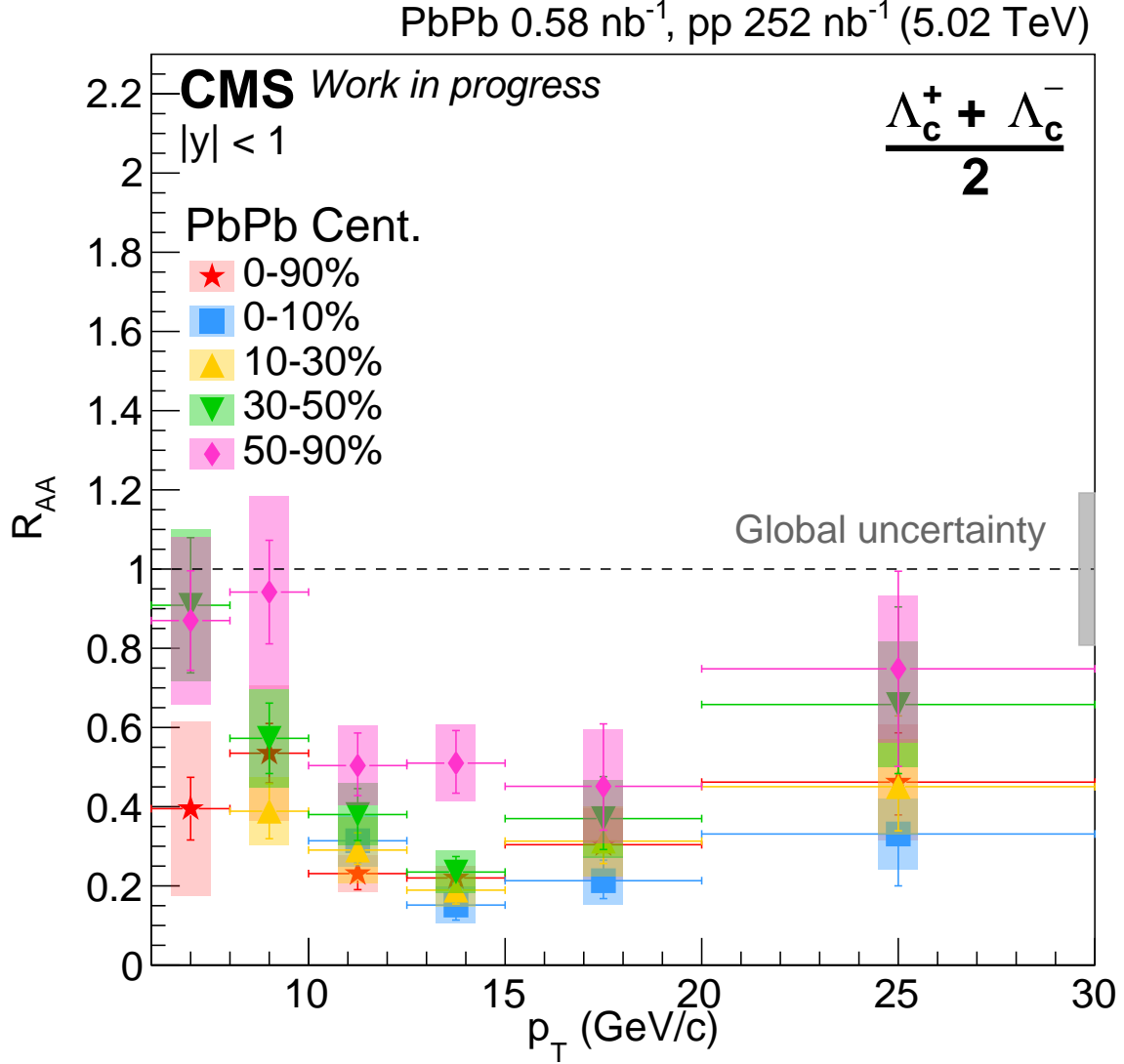
Figure 5.21. The Nuclear Modification Factor R_{AA} Versus p_T For Prompt Λ_c^+ Production. The Boxes And Error Bars Represent The Systematic And Statistical Uncertainties, Respectively. The band At Unity Labeled Global Uncertainty Includes The Uncertainties For The Luminosity Of pp Collisions, Number Of MinimumBias Events In PbPb Collisions, And Tracking Efficiency.

Figure 5.22. The Ratio Of The Production Cross Sections Of Prompt Λ_c^+ To Prompt D^0 Versus p_T From pp Collisions, As Well As 0–90% And 0–10% Centrality Classes In PbPb Collisions. The Boxes And Error Bars Represent The Systematic And Statistical Uncertainties, Respectively. The 6.8 And 7.4% Normalization Uncertainties In pp And PbPb Collisions, Respectively, Are Not Included In The Boxes Representing The Systematic Uncertainties For Each Data Point. The Open Stars Represent The Predictions Of PYTHIA 8 With Color Reconnection [69]. The Black And Purple Solid Lines Are The pp And PbPb Calculations(0–100% centrality) For Prompt Λ_c^+ Over Prompt D^0 Production Ratio From Ref. [47], And The Dashed Line Is The pp Calculation From Ref. [72].

6. SUMMARY

The p_T-differential cross sections of inclusive Λ_c^+ (including prompt and nonprompt contributions) and prompt Λ_c^+ have been measured with 2015 pp/PbPb and 2017/2018 pp/PbPb at 5.02 TeV with CMS detector. The shape of the inclusive Λ_c^+ p_T distribution in pp collisions is well described by the PYTHIA8 event generator. GMVFNS predictions with 3 different fragmentation functions are consistent with 2017 pp prompt data within uncertainties with $p_T > 8$ GeV/c, while pp data measurements are systematically above these three predictions when $p_T < 8$ GeV/c.

There is a suppression of prompt Λ_c^+ observed in centrality class: 0-90% and 0-10% in PbPb collisions. This is consistent with the suppression observed in D^0 meson measurements, which is understood to originate from the strong interaction between the charm quark and the quark-gluon plasma.

The Λ_c^+/D^0 production ratios in pp collisions are consistent with a model obtained by adding color reconnection in hadronization to PYTHIA8, and also with a model that includes enhanced contributions from the decay of excited charm baryons. There is a hint of an enhancement of Λ_c^+/D^0 production ratio in 6–12.5 GeV/c in PbPb collisions compared with pp production ratio. The Λ_c^+/D^0 production ratios in pp and PbPb collisions for $p_T = 12.5$–30 GeV/c are found to be consistent with each other. This may suggest that the coalescence process does not play a significant role in Λ_c^+ baryon production in this p_T range.

REFERENCES

[1] A. M. Sirunyan *et al.*, "Production of Λ_c^+ baryons in proton-proton and lead-lead collisions at $\sqrt{s_{\mathrm{NN}}}$ = 5.02 TeV," *Phys. Lett. B*, vol. 803, p. 135 328, 2020. DOI: 10.1016/j.physletb.2020.135328. arXiv: 1906.03322 [hep-ex].

[2] Particle Data Group, M. Tanabashi, *et al.*, "Review of particle physics," *Phys. Rev. D*, vol. 98, p. 030 001, 2018. DOI: 10.1103/PhysRevD.98.030001.

[3] S. Chatrchyan *et al.*, "Observation of a New Boson at a Mass of 125 GeV with the CMS Experiment at the LHC," *Phys. Lett. B*, vol. 716, pp. 30–61, 2012. DOI: 10.1016/j.physletb.2012.08.021. arXiv: 1207.7235 [hep-ex].

[4] G. Aad *et al.*, "Observation of a new particle in the search for the Standard Model Higgs boson with the ATLAS detector at the LHC," *Phys. Lett. B*, vol. 716, pp. 1–29, 2012. DOI: 10.1016/j.physletb.2012.08.020. arXiv: 1207.7214 [hep-ex].

[5] P. W. Higgs, "Broken symmetries and the masses of gauge bosons," *Phys. Rev. Lett.*, vol. 13, pp. 508–509, 16 Oct. 1964. DOI: 10.1103/PhysRevLett.13.508. [Online]. Available: https://link.aps.org/doi/10.1103/PhysRevLett.13.508.

[6] Wikipedia, 2020. [Online]. Available: https://en.wikipedia.org/wiki/Elementary_particle.

[7] M. Y. Han and Y. Nambu, "Three-triplet model with double SU(3) symmetry," *Phys. Rev.*, vol. 139, B1006–B1010, 4B Aug. 1965. DOI: 10.1103/PhysRev.139.B1006. [Online]. Available: https://link.aps.org/doi/10.1103/PhysRev.139.B1006.

[8] H. D. Politzer, "Reliable perturbative results for strong interactions?" *Phys. Rev. Lett.*, vol. 30, pp. 1346–1349, 26 Jun. 1973. DOI: 10.1103/PhysRevLett.30.1346. [Online]. Available: https://link.aps.org/doi/10.1103/PhysRevLett.30.1346.

[9] J. Greensite, *An introduction to the confinement problem.* 2011, vol. 821. DOI: 10.1007/978-3-642-14382-3.

[10] D. J. Gross and F. Wilczek, "Ultraviolet Behavior of Nonabelian Gauge Theories," *Phys. Rev. Lett.*, vol. 30, J. C. Taylor, Ed., pp. 1343–1346, 1973. DOI: 10.1103/PhysRevLett.30.1343.

[11] S. Bethke, "Experimental tests of asymptotic freedom," *Prog. Part. Nucl. Phys.*, vol. 58, pp. 351–386, 2007. DOI: 10.1016/j.ppnp.2006.06.001. arXiv: hep-ex/0606035.

[12] E. V. Shuryak, "Theory of hadronic plasma," *Sov. Phys. JETP*, vol. 47, p. 212, 1978, [Zh. Eksp. Teor. Fiz. 74 (1978) 408]. [Online]. Available: http://jetp.ac.ru/cgi-bin/e/index/e/47/2/p212?a=list.

[13] A. Bazavov, T. Bhattacharya, M. Cheng, N. H. Christ, C. DeTar, S. Ejiri, S. Gottlieb, R. Gupta, U. M. Heller, K. Huebner, C. Jung, F. Karsch, E. Laermann, L. Levkova, C. Miao, R. D. Mawhinney, P. Petreczky, C. Schmidt, R. A. Soltz, W. Soeldner, R. Sugar, D. Toussaint, and P. Vranas, "Equation of state and QCD transition at finite temperature," *Phys. Rev. D*, vol. 80, p. 014 504, 1 Jul. 2009. DOI: 10.1103/PhysRevD.80.014504. [Online]. Available: https://link.aps.org/doi/10.1103/PhysRevD.80.014504.

[14] J. C. Collins and M. J. Perry, "Superdense Matter: Neutrons or Asymptotically Free Quarks?" *Phys. Rev. Lett.*, vol. 34, pp. 1353–1356, 21 May 1975. DOI: 10.1103/PhysRevLett.34.1353. [Online]. Available: https://link.aps.org/doi/10.1103/PhysRevLett.34.1353.

[15] Y. Akiba *et al.*, "The Hot QCD White Paper: Exploring the Phases of QCD at RHIC and the LHC," Feb. 2015. arXiv: 1502.02730 [nucl-ex].

[16] M. Gyulassy and M. Plumer, "Jet Quenching in Dense Matter," *Phys. Lett. B*, vol. 243, pp. 432–438, 1990. DOI: 10.1016/0370-2693(90)91409-5.

[17] R. Baier, Y. L. Dokshitzer, A. H. Mueller, S. Peigne, and D. Schiff, "Radiative energy loss and p(T) broadening of high-energy partons in nuclei," *Nucl. Phys. B*, vol. 484, pp. 265–282, 1997. DOI: 10.1016/S0550-3213(96)00581-0. arXiv: hep-ph/9608322.

[18] J. Casalderrey-Solana and C. A. Salgado, "Introductory lectures on jet quenching in heavy ion collisions," *Acta Phys. Polon. B*, vol. 38, M. Praszalowicz, M. Kutschera, and E. Malec, Eds., pp. 3731–3794, 2007. arXiv: 0712.3443 [hep-ph].

[19] J. D. Bjorken, "Energy Loss of Energetic Partons in Quark - Gluon Plasma: Possible Extinction of High p(t) Jets in Hadron - Hadron Collisions," Aug. 1982.

[20] M. H. Thoma and M. Gyulassy, "Quark Damping and Energy Loss in the High Temperature QCD," *Nucl. Phys. B*, vol. 351, pp. 491–506, 1991. DOI: 10.1016/S0550-3213(05)80031-8.

[21] J. Adams *et al.*, "Experimental and theoretical challenges in the search for the quark gluon plasma: The STAR Collaboration's critical assessment of the evidence from RHIC collisions," *Nucl. Phys. A*, vol. 757, pp. 102–183, 2005. DOI: 10.1016/j.nuclphysa.2005.03.085. arXiv: nucl-ex/0501009.

[22] K. Adcox *et al.*, "Formation of dense partonic matter in relativistic nucleus-nucleus collisions at RHIC: Experimental evaluation by the PHENIX collaboration," *Nucl. Phys. A*, vol. 757, pp. 184–283, 2005. DOI: 10.1016/j.nuclphysa.2005.03.086. arXiv: nucl-ex/0410003.

[23] I. Arsene *et al.*, "Quark gluon plasma and color glass condensate at RHIC? The Perspective from the BRAHMS experiment," *Nucl. Phys. A*, vol. 757, pp. 1–27, 2005. DOI: 10.1016/j.nuclphysa.2005.02.130. arXiv: nucl-ex/0410020.

[24] B. B. Back *et al.*, "The PHOBOS perspective on discoveries at RHIC," *Nucl. Phys. A*, vol. 757, pp. 28–101, 2005. DOI: 10.1016/j.nuclphysa.2005.03.084. arXiv: nucl-ex/0410022.

[25] B. Muller, J. Schukraft, and B. Wyslouch, "First Results from Pb+Pb collisions at the LHC," *Ann. Rev. Nucl. Part. Sci.*, vol. 62, pp. 361–386, 2012. DOI: 10.1146/annurev-nucl-102711-094910. arXiv: 1202.3233 [hep-ex].

[26] N. Armesto and E. Scomparin, "Heavy-ion collisions at the Large Hadron Collider: a review of the results from Run 1," *Eur. Phys. J. Plus*, vol. 131, no. 3, p. 52, 2016. DOI: 10.1140/epjp/i2016-16052-4. arXiv: 1511.02151 [nucl-ex].

[27] Chatrchyan *et al.*, "Dependence on pseudorapidity and on centrality of charged hadron production in PbPb collisions at $\sqrt{s_{NN}}$ = 2.76 TeV," *JHEP*, vol. 08, 141. 35 p, Jul. 2011. DOI: 10.1007/JHEP08(2011)141. arXiv: 1107.4800. [Online]. Available: https://cds.cern.ch/record/1370087.

[28] M. L. Miller, K. Reygers, S. J. Sanders, and P. Steinberg, "Glauber modeling in high energy nuclear collisions," *Ann. Rev. Nucl. Part. Sci.*, vol. 57, p. 205, 2007. DOI: 10.1146/annurev.nucl.57.090506.123020. arXiv: nucl-ex/0701025 [nucl-ex].

[29] A. Beraudo *et al.*, "Extraction of heavy-flavor transport coefficients in QCD matter," *Nucl. Phys. A*, vol. 979, R. Rapp, P. B. Gossiaux, A. Andronic, R. Averbeck, and S. Masciocchi, Eds., p. 21, 2018. DOI: 10.1016/j.nuclphysa.2018.09.002. arXiv: 1803.03824 [nucl-th].

[30] V. Greco, C. M. Ko, and P. Lévai, "Parton coalescence and the antiproton/pion anomaly at RHIC," *Phys. Rev. Lett.*, vol. 90, p. 202 302, 2003. DOI: 10.1103/PhysRevLett.90.202302. arXiv: nucl-th/0301093 [nucl-th].

[31] R. J. Fries, V. Greco, and P. Sorensen, "Coalescence models for hadron formation from quark gluon plasma," *Ann. Rev. Nucl. Part. Sci.*, vol. 58, p. 177, 2008. DOI: 10.1146/annurev.nucl.58.110707.171134. arXiv: 0807.4939 [nucl-th].

[32] B. I. Abelev *et al.*, "Identified baryon and meson distributions at large transverse momenta from Au+Au collisions at $\sqrt{s_{\mathrm{NN}}}$ = 200 GeV," *Phys. Rev. Lett.*, vol. 97, p. 152 301, 2006. DOI: 10.1103/PhysRevLett.97.152301. arXiv: nucl-ex/0606003.

[33] B. I. Abelev *et al.*, "Systematic measurements of identified particle spectra in pp, d+Au and Au+Au collisions from STAR," *Phys. Rev. C*, vol. 79, p. 034 909, 2009. DOI: 10.1103/PhysRevC.79.034909. arXiv: 0808.2041 [nucl-ex].

[34] B. I. Abelev *et al.*, "Centrality dependence of charged hadron and strange hadron elliptic flow from $\sqrt{s_{\mathrm{NN}}}$ = 200 Au+Au collisions," *Phys. Rev. C*, vol. 77, p. 054 901, 2008. DOI: 10.1103/PhysRevC.77.054901. arXiv: 0801.3466 [nucl-ex].

[35] A. Adare *et al.*, " suppression at forward rapidity in Au+Au collisions at $\sqrt{s_{\mathrm{NN}}}$ =200," *Phys. Rev. C*, vol. 84, p. 054 912, 2011. DOI: 10.1103/PhysRevC.84.054912. arXiv: 1103.6269 [nucl-ex].

[36] J. Adam *et al.*, " suppression at forward rapidity in Pb-Pb collisions at $\sqrt{s_{\mathrm{NN}}}$ = 5.02 tev," *Phys. Lett. B*, vol. 766, p. 212, 2017. DOI: 10.1016/j.physletb.2016.12.064. arXiv: 1606.08197 [nucl-ex].

[37] B. B. Abelev *et al.*, "Centrality, rapidity and transverse momentum dependence of suppression in Pb-Pb collisions at $\sqrt{s_{\mathrm{NN}}}$ = 2.76 TeV," *Phys. Lett. B*, vol. 734, p. 314, 2014. DOI: 10.1016/j.physletb.2014.05.064. arXiv: 1311.0214 [nucl-ex].

[38] L. Adamczyk *et al.*, "Observation of D^0 meson nuclear modifications in Au+Au collisions at $\sqrt{s_{\mathrm{NN}}}$ = 200 GeV," *Phys. Rev. Lett.*, vol. 113, p. 142 301, 2014, [Erratum: 10.1103/PhysRevLett.121.229901]. DOI: 10.1103/PhysRevLett.113.142301. arXiv: 1404.6185 [nucl-ex].

[39] J. Adam *et al.*, "Centrality and transverse momentum dependence of D^0-meson production at mid-rapidity in Au+Au collisions at $\sqrt{s_{\mathrm{NN}}}$ = 200 GeV," *Phys. Rev. C*, vol. 99, p. 034 908, 2019. DOI: 10.1103/PhysRevC.99.034908. arXiv: 1812.10224 [nucl-ex].

[40] A. M. Sirunyan *et al.*, "Measurement of prompt D^0 meson azimuthal anisotropy in Pb-Pb collisions at $\sqrt{s_{\mathrm{NN}}}$ = 5.02 TeV," *Phys. Rev. Lett.*, vol. 120, p. 202 301, 2018. DOI: 10.1103/PhysRevLett.120.202301. arXiv: 1708.03497 [nucl-ex].

[41] A. M. Sirunyan *et al.*, "Nuclear modification factor of D^0 mesons in PbPb collisions at $\sqrt{s_{\mathrm{NN}}}$ = 5.02 tev," *Phys. Lett. B*, vol. 782, p. 474, 2018. DOI: 10.1016/j.physletb.2018.05.074. arXiv: 1708.04962 [nucl-ex].

[42] S. Acharya *et al.*, "*D*-meson azimuthal anisotropy in midcentral Pb-Pb collisions at $\sqrt{s_{NN}}$ = 5.02 tev," *Phys. Rev. Lett.*, vol. 120, p. 102 301, 2018. DOI: 10.1103/PhysRevLett.120.102301. arXiv: 1707.01005 [nucl-ex].

[43] S. Acharya *et al.*, "Measurement of D^0, D^+, D^{*+} and production in Pb-Pb collisions at $\sqrt{s_{NN}}$ =5.02 tev," *JHEP*, vol. 10, p. 174, 2018. DOI: 10.1007/JHEP10(2018)174. arXiv: 1804.09083 [nucl-ex].

[44] Y. Oh, C. M. Ko, S. H. Lee, and S. Yasui, "Heavy baryon/meson ratios in relativistic heavy ion collisions," *Phys. Rev. C*, vol. 79, p. 044 905, 2009. DOI: 10.1103/PhysRevC.79.044905. arXiv: 0901.1382 [nucl-th].

[45] S. H. Lee, K. Ohnishi, S. Yasui, I.-K. Yoo, and C.-M. Ko, "Λ_c enhancement from strongly coupled quark-gluon plasma," *Phys. Rev. Lett.*, vol. 100, p. 222 301, 2008. DOI: 10.1103/PhysRevLett.100.222301. arXiv: 0709.3637 [nucl-th].

[46] S. Ghosh, S. K. Das, V. Greco, S. Sarkar, and J.-e. Alam, "Diffusion of Λ_c in hot hadronic medium and its impact on Λ_c/D ratio," *Phys. Rev. D*, vol. 90, p. 054 018, 2014. DOI: 10.1103/PhysRevD.90.054018. arXiv: 1407.5069 [nucl-th].

[47] S. Plumari, V. Minissale, S. K. Das, G. Coci, and V. Greco, "Charmed hadrons from coalescence plus fragmentation in relativistic nucleus-nucleus collisions at RHIC and LHC," *Eur. Phys. J. C*, vol. 78, p. 348, 2018. DOI: 10.1140/epjc/s10052-018-5828-7. arXiv: 1712.00730 [hep-ph].

[48] S. Acharya *et al.*, "Λ_c^+ production in pp collisions at $\sqrt{s}$= 7 TeV and in p-Pb collisions at $\sqrt{s_{NN}}$ = 5.02 tev," *JHEP*, vol. 04, p. 108, 2018. DOI: 10.1007/JHEP04(2018)108. arXiv: 1712.09581 [nucl-ex].

[49] S. Acharya *et al.*, "Λ_c^+ production in Pb-Pb collisions at $\sqrt{s_{NN}}$ = 5.02 tev," *Phys. Lett. B*, vol. 793, p. 212, 2019. DOI: 10.1016/j.physletb.2019.04.046. arXiv: 1809.10922 [nucl-ex].

[50] R. Aaij *et al.*, "Prompt charm production in pp collisions at $\sqrt{s}$ = 7 TeV," *Nucl. Phys. B*, vol. 871, p. 1, 2013. DOI: 10.1016/j.nuclphysb.2013.02.010. arXiv: 1302.2864 [hep-ex].

[51] R. Aaij *et al.*, "Prompt Λ_c^+ production in pPb collisions at $\sqrt{s_{NN}}$ = 5.02 tev," *JHEP*, vol. 02, p. 102, 2019. DOI: 10.1007/JHEP02(2019)102. arXiv: 1809.01404 [hep-ex].

[52] M. A. G. Aivazis, J. C. Collins, F. I. Olness, and W.-K. Tung, "Leptoproduction of heavy quarks. II. A unified QCD formulation of charged and neutral current processes from fixed-target to collider energies," *Phys. Rev. D*, vol. 50, p. 3102, 1994. DOI: 10.1103/PhysRevD.50.3102.

[53] T. Sjöstrand, S. Ask, J. R. Christiansen, R. Corke, N. Desai, P. Ilten, S. Mrenna, S. Prestel, C. O. Rasmussen, and P. Z. Skands, "An introduction to PYTHIA 8.2," *Comput. Phys. Commun.*, vol. 191, p. 159, 2015. DOI: 10.1016/j.cpc.2015.01.024. arXiv: 1410.3012 [hep-ph].

[54] T. Sjostrand, S. Mrenna, and P. Z. Skands, "PYTHIA 6.4 Physics and Manual," *JHEP*, vol. 05, p. 026, 2006. DOI: 10.1088/1126-6708/2006/05/026. arXiv: hep-ph/0603175.

[55] S. Chatrchyan *et al.*, "The CMS experiment at the CERN LHC," *JINST*, vol. 3, S08004, 2008. DOI: 10.1088/1748-0221/3/08/S08004.

[56] S. Chatrchyan *et al.*, "Description and performance of track and primary-vertex reconstruction with the CMS tracker," *JINST*, vol. 9, P10009, 2014. DOI: 10.1088/1748-0221/9/10/P10009. arXiv: 1405.6569 [physics.ins-det].

[57] CMS Collaboration, "CMS Technical Design Report for the Pixel Detector Upgrade," Tech. Rep., Sep. 2012, Additional contacts: Jeffrey Spalding, Fermilab, Jeffrey.Spalding@cern.ch Didier Contardo, Universite Claude Bernard-Lyon I, didier.claude.contardo@cern.ch. [Online]. Available: https://cds.cern.ch/record/1481838.

[58] CMS Collaboration, *CMS TriDAS project: Technical Design Report, Volume 1: The Trigger Systems*, ser. Technical design report. CMS. [Online]. Available: https://cds.cern.ch/record/706847.

[59] P. Sphicas *et al.*, "CMS: The TriDAS project. Technical design report, Vol. 2: Data acquisition and high-level trigger," Dec. 2002.

[60] C. Grandi, D. Stickland, L. Taylor, A. Petrilli, and A. Hervé, "CMS Computing Model: The "CMS Computing Model RTAG"," CERN, Geneva, Tech. Rep., Dec. 2004. [Online]. Available: https://cds.cern.ch/record/814248.

[61] H. Voss, A. Hocker, J. Stelzer, and F. Tegenfeldt, "TMVA, the Toolkit for Multivariate Data Analysis with ROOT," *PoS*, vol. ACAT, p. 040, 2007. DOI: 10.22323/1.050.0040.

[62] V. Khachatryan *et al.*, "Event generator tunes obtained from underlying event and multiparton scattering measurements," *Eur. Phys. J. C*, vol. 76, p. 155, 2016. DOI: 10.1140/epjc/s10052-016-3988-x. arXiv: 1512.00815 [hep-ex].

[63] I. P. Lokhtin and A. M. Snigirev, "A model of jet quenching in ultrarelativistic heavy ion collisions and high-p_t $hadron spectra at RHIC$," *Eur. Phys. J. C*, vol. 45, p. 211, 2006. DOI: 10.1140/epjc/s2005-02426-3. arXiv: hep-ph/0506189 [hep-ph].

[64] A. M. Sirunyan *et al.*, "Studies of beauty suppression via nonprompt D^0 mesons in Pb-Pb collisions at $\sqrt{s_{\mathrm{NN}}}$ = 5.02 tev," *Phys. Rev. Lett.*, vol. 123, p. 022 001, 2019. DOI: 10.1103/PhysRevLett.123.022001. arXiv: 1810.11102 `[hep-ex]`.

[65] A. M. Sirunyan *et al.*, "Measurement of the $B^{\pm}$ meson nuclear modification factor in Pb-Pb collisions at $\sqrt{s_{\mathrm{NN}}}$ = 5.02 tev," *Phys. Rev. Lett.*, vol. 119, p. 152 301, 2017. DOI: 10.1103/PhysRevLett.119.152301. arXiv: 1705.04727 `[hep-ex]`.

[66] M. Cacciari, M. Greco, and P. Nason, "The p_T spectrum in heavy flavor hadroproduction," *JHEP*, vol. 05, p. 007, 1998. DOI: 10.1088/1126-6708/1998/05/007. arXiv: hep-ph/9803400 `[hep-ph]`.

[67] CMS Collaboration, "CMS luminosity calibration for the pp reference run at $\sqrt{s}$= 5.02 TeV," CMS Physics Analysis Summary CMS-PAS-LUM-16-001, 2016. [Online]. Available: http://cdsweb.cern.ch/record/2235781.

[68] V. Khachatryan *et al.*, "Charged-particle nuclear modification factors in PbPb and pPb collisions at $\sqrt{s_{\mathrm{NN}}}$ = 5.02 tev," *JHEP*, vol. 04, p. 039, 2017. DOI: 10.1007/JHEP04(2017)039. arXiv: 1611.01664 `[nucl-ex]`.

[69] J. R. Christiansen and P. Z. Skands, "String formation beyond leading colour," *JHEP*, vol. 08, p. 003, 2015. DOI: 10.1007/JHEP08(2015)003. arXiv: 1505.01681 `[hep-ph]`.

[70] M. Benzke, M. V. Garzelli, B. Kniehl, G. Kramer, S. Moch, and G. Sigl, "Prompt neutrinos from atmospheric charm in the general-mass variable-flavor-number scheme," *JHEP*, vol. 12, p. 021, 2017. DOI: 10.1007/JHEP12(2017)021. arXiv: 1705.10386 `[hep-ph]`.

[71] P. Skands, S. Carrazza, and J. Rojo, "Tuning PYTHIA 8.1: the Monash 2013 tune," *Eur. Phys. J. C*, vol. 74, p. 3024, 2014. DOI: 10.1140/epjc/s10052-014-3024-y. arXiv: 1404.5630 `[hep-ph]`.

[72] M. He and R. Rapp, "Charm-baryon production in proton-proton collisions," *Phys. Lett. B*, vol. 795, p. 117, 2019. DOI: 10.1016/j.physletb.2019.06.004. arXiv: 1902.08889 `[nucl-th]`.

[73] CMS Collaboration, "Luminosity measurement in proton-proton collisions at 5.02 TeV in 2017 at CMS," CMS Physics Analysis Summary CMS-PAS-LUM-19-001, 2019. [Online]. Available: http://cdsweb.cern.ch/record/2235781.

VITA

Rui Xiao graduated from Shandong University in June 2015 with a Bachelor of Science Degree in Physics. She pursed her graduate study at Purdue University from 2015 to 2021. Rui joined the high energy nuclear physics group under Prof. Wei Xie, as a member of the CMS Collaboration. Rui will graduate from Purdue University with a Ph.D in physics in 2021.